Three-Dimensional Electromagnetic Scattering from Layered Media with Rough Interfaces for Subsurface Radar Remote Sensing

by

Xueyang Duan

A dissertation submitted in partial fulfillment
of the requirements for the degree of
Doctor of Philosophy
(Electrical Engineering)
in The University of Michigan
2012

Doctoral Committee:

Professor Mahta Moghaddam, Chair
Professor Eric Michielssen
Professor Christopher Ruf
Professor Fawwaz Ulaby

To my parents and friends.

ACKNOWLEDGEMENTS

First of all, I would like to express my sincere gratitude to my advisor and committee chair, Professor Mahta Moghaddam, for her continuous support to my Ph. D study. Her patience and encouragement are always there from the beginning of my experience as a graduate student in the University of Michigan through my writing this dissertation. Her inspiration, advices, as well as the freedom she gave to me to explore on my own make my Ph. D experience productive and stimulating. I also would like to thank my other committee members: Professor Eric Michielssen, Professor Christopher Ruf, and Professor Fawwaz Ulaby, for agreeing to be on my dissertation committee and accepting to evaluate this dissertation work. I am grateful to Professor Michielssen especially for providing method of moments simulation results for the validation of the modeling methodology of long cylinder scattering in this work.

I would like to acknowledge my colleagues and friends in Radiation Laboratory for their unconditional help and invaluable friendship. I especially want to thank Mark Haynes and Steven Clarkson for their building and offering measurement setup for my validation of the random media scattering model, thank Yuriy Goykhman for his contribution in designing and building the tower-based radar, as well as Guanbo Chen and Ruzbeh Akbar for their help on takeing the radar measurements. I would also like to acknowledge my colleague Alireza Tabatabaeenejad for his help on editing part of my dissertation. I am grateful for all the support I got from Dr. Leland Pierce, Dr. Adib Nashashibi, Dr. Roger De Roo, Mehrnoosh Vahidpour, Line van Nieuwstadt, Mariko Buergin, and Scott Rudolph.

I would like to thank Dr. Joel T. Johnson and his group from Ohio State University for

providing the multilayer SPM3 and MoM data for our model validation.

I would also like to acknowledge Dr. Jasmeet Judge and her group from the University of Florida, for their facilities, collaboration, and providing ground sensor data for our radar measurements in Gainesville, FL.

Finally, I would like to express my deepest gratitude to my parents and all friends. Without their love and care, the completion of this dissertation would not have been possible.

TABLE OF CONTENTS

LIST OF FIGURES

LIST OF TABLES

LIST OF APPENDICES

APPENDIX

CHAPTER 1

Introduction

1.1   Background and Motivation

This dissertation is motivated by numerous applications of microwave remote sensing of layered random media with rough interfaces. Such a structure exists widely in natural settings and manmade objects, for example, soil fields with or without vegetation, multi-year ice, human skin-tissue interface, civil infrastructure, and solid state components with deposited metal or dielectrics. Electromagnetic scattering at various bands from these objects usually contains information about their geometry and dielectric properties, which can be exploited by microwave remote sensing. As a noninvasive technique, microwave remote sensing is extremely attractive for this purpose since it can be used for soil moisture and biomass estimation, facility construction monitoring, warning of landslide, permafrost characterization, glacier monitoring, medical imaging, infrastructure defect detection, component quality control, etc. In this dissertation, we focus on remote sensing application to soil moisture evaluation.

Soil moisture is one of the entities closely related to both our daily lives and long-term environmental dynamics of the Earth. Importance of soil moisture is evident in many areas: directly affecting vegetation growth, soil moisture is one of the first-order determinants of agricultural production. Monitoring changes in soil moisture can assist in risk reduction
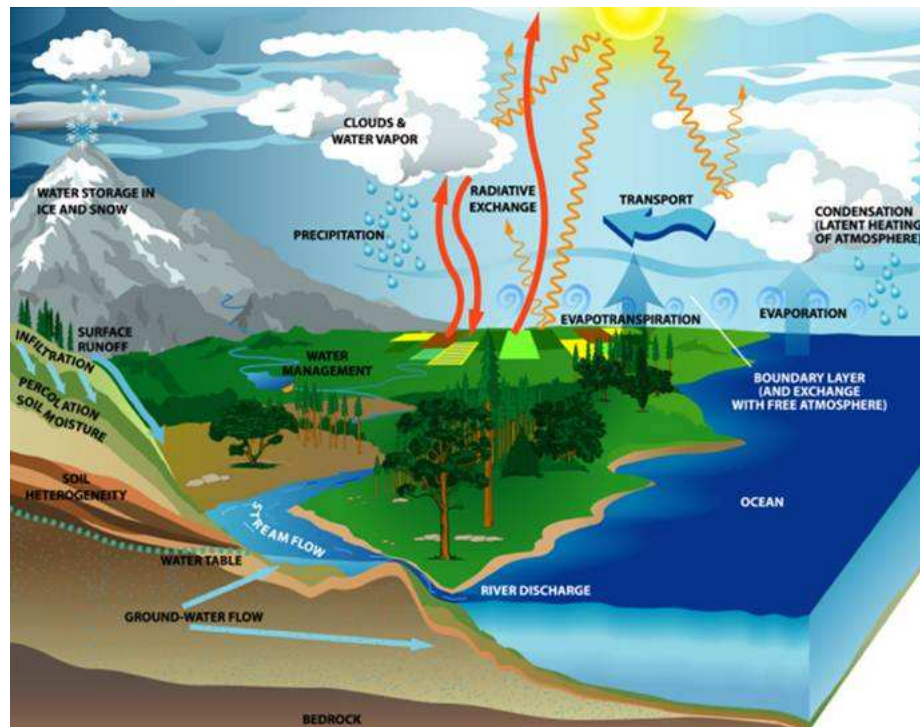
Figure 1.1: Conceptualization of global water cycle [2]

strategies. Water stored in soil plays an important role in water cycling and top soil degra-dation. Due to its control on soil evaporation and transpiration, surface soil moisture is a key parameter in modeling the heat and mass transfer in the global water and energy cycle (Figure 1.1). Knowledge of temporal and spatial distribution of soil moisture on a global scale is critical for weather forecast and climate prediction [1]. This list can go on.

Despite its importance, global distribution of soil moisture, especially the root-zone soil moisture, is currently one of the least observed quantities. The ground in-situ measure-ment of soil moisture requires dense or local optimized sampling to meet the resolution requirements by the global circulation models (<50 to 100 km) and hydrologic models (<10 to 20 km) [3]; this can be hardly achieved with sufficient spatial and temporal fre-quency, especially at a global scale. Microwave remote sensing may be the only feasible approach for providing these observations since the soil dielectric properties are directly related to its moisture content. In particular, active microwave remote sensing technology has the advantages of high resolution, large area coverage, and all-weather operating capa-
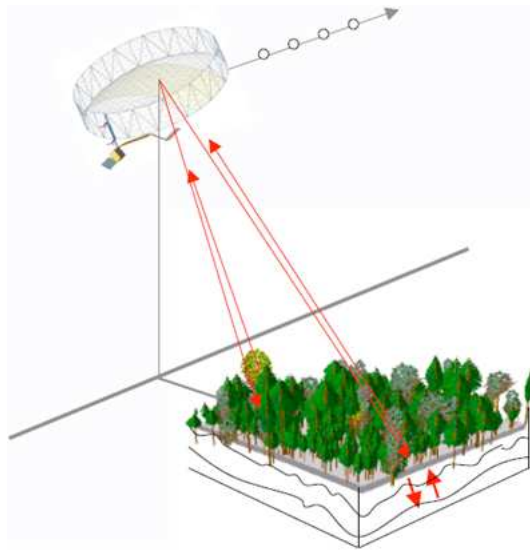
Figure 1.2: Radar remote sensing of soil moisture

bility without disturbing the ground. Moreover, low-frequency (P-band: 216 to 450 MHz and VHF: 30 to 300 MHz) radar systems are preferred for subsurface and root-zone moisture detection for their large depth of ground penetration (Figure 1.2).

Missions and experimental systems for global or regional soil moisture determination have been proposed and implemented since the 1980s. Various platforms have been considered, such as spaceborne, airborne, and near-ground systems. The most recent spaceborne system is the Soil Moisture and Ocean Salinity (SMOS) mission launched by European Space Agency (ESA) in 2009 which provides global soil moisture radiometric observation at L-band, but with low resolution of 50 km [3] [4]. The RADARSAT-2 launched by Canadian Space Agency (CSA) in 2007 operates at C-band [5] and have been used to produce estimations of soil moisture with high resolution but for sparsely vegetated area and short crops. Besides spaceborne systems, which have the advantage of large-area coverage with regular repeat observations, airborne systems are also used but localized for regional measurements. For example, the National Aeronautics and Space Administration / Jet Propulsion Laboratory (NASA/JPL) AIRSAR operating at C-, L-, and P-bands flew from 1988 to 2004 and was used in a limited capacity to develop methods for retrival of soil moisture, and in particular for estimating subcanopy soil moisture [6]. The NASA Uninhabited

3
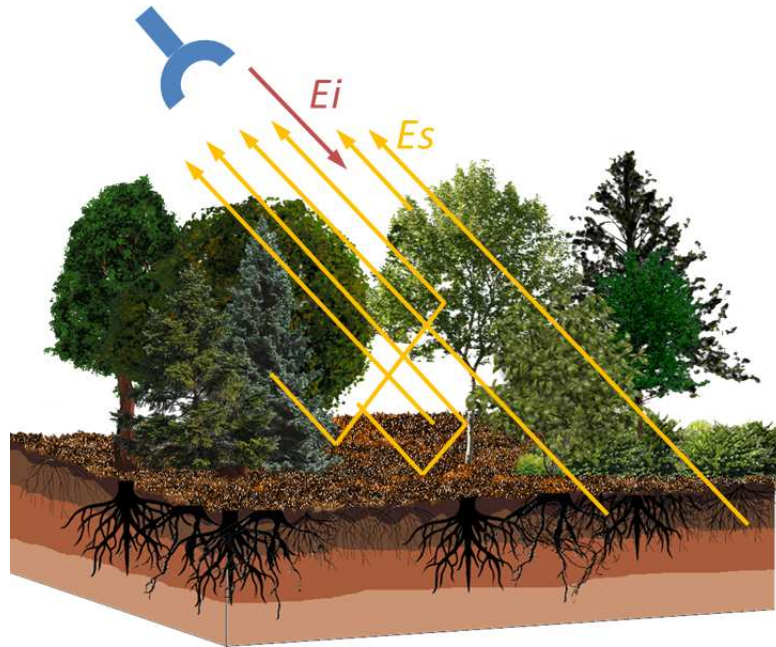
Figure 1.3: Backscattering in low frequency measurement of vegetated ground

Aerial Vehicle Synthetic Aperture Radar (UAVSAR) is a state-of-the-art reconfigurable, polarimetric L-band SAR that has been used recently in support of soil moisture retrieval validations [7]. Operating at lower altitude, tower-based systems have been used for small area measurements and proof-of-concept experiments. One example is the Microwave Observatory of Subcanopy and Subsurface (MOSS) tower radar [8], which has been used for subsurface soil moisture measurements.

Recently, NASA has initiated the spaceborne Soil Moisture Active and Passive (SMAP) mission and the Airborne Microwave Observatory of Subcanopy and Subsurface (Air-MOSS) mission. SMAP will be launched in 2014 equipped with a SAR operating at L-band measuring the global soil moisture at resolutions of 1-3 km [9] and an L-band radiometer with a resolution of 40 km. And the AirMOSS will start to fly an airborne SAR at P-band over several locations in North America in 2012 for subsurface and root-zone soil moisture characterization.

For the purpose of feasibility analysis, radar system design optimization and development of retrieval algorithms for geophysical quantities using the radar measurements, for-

Figure 1.4: Layered structure in ground with vegetation roots and other inhomogeneities [10]

ward modeling of electromagnetic scattering from the ground provides us an indispensable tool. It computes the expected radar scattering cross section from given ground characteristics including soil profile, moisture content, and soil surface statistics. Such a model is required to be computationally efficient, capable of simulating realistic scenarios, and applicable to large variety of soil conditions, including surface roughnesses, soil moisture profiles, existence of subsurfaces and inhomogeneous sublayer media (Figure 1.3 and 1.4).

1.2   Overview of Related Studies and Previous Work

In the past several decades, much work has been dedicated to modeling and prediction of electromagnetic scattering from the ground. The existing modeling methods can be generally categorized into empirical regression techniques and theoretical scattering models. The empirical or semi-empirical solutions [11] [12] are based on large sets of measurement data at specific locations and with specific sensors, and therefore have a generally small domain of validity. The theoretical approaches are based on physical models and can be applied to more general ground conditions and sensor characteristics. The theoretical

scattering models can be further classified into analytical, numerical, and semi-numerical solutions. The analytical solutions may involve limiting assumptions in, for example, surface roughness, to allow the derivation of a closed form expression. Therefore, they usually have the highest computational efficiency among theoretical scattering models, yet their validity is limited to smoother surfaces. On the other hand, numerical methods can solve for surfaces with large roughnesses with very high computational cost. Semi-numerical approaches are a good trade-off between the validity domain and the computational cost, by transforming to discrete spectral domain representation and by making use of the physical properties of the problem. The methods we developed in this dissertation are in this category.

For scattering from rough surfaces, studies can be traced back to 1950s starting with single rough surface scattering [13] [14] [15], which evolved into analytical solutions such as the small perturbation method (SPM) [16] [17], small-slope approximation (SSA) [18] [19], and Kirchhoff approximation (KA) [16]. With the advent of digital computers, numerical approaches were later developed, which can be grouped into time-domain methods [20] [21] and frequency-domain methods [20] [22] [23] [24], for example, method of moments (MoM), integral equation method (IEM), and advanced integral equation method (AIEM). As a semi-numerical method, the extended boundary condition method (EBCM), which was first proposed in [25], was applied to the problem of electromagnetic scattering from rough surfaces [16] [26]. However, its solution was found to be unstable for larger roughnesses, resulting in a validity regime only a bit larger than the analytical methods. Among these approaches, SPM and MoM have been extended to multilayer structures [17] [27].

Numerous works have focused on solving the problem of wave propagation through and scattering from random media. One approximate technique is the radiative transfer equation (RTE), which was first proposed in [28], and became a classical method when describing the wave propagation through a sparse medium. However, this method is an incoherent approach based on power conservation without considering the interaction among

particles. Another approximate technique is to treat the random medium as a mixture of disconnected particles and find its effective permittivity [29] [16]. The models based on this technique usually take account of only dipole-dipole interactions among particles, and can be viewed as a low frequency approximation. For dense media, many multiple scattering solutions are developed since the work in [30], such as the quasi-crystalline approximation (QCA) [31], the coherent-potential approximation (CPA) [32], and the strong fluctuation theory [33] [34]. Though these methods take into account higher-order interactions in the media, they neglect the multipole coupling among particles in the process of statistical averaging. On the contrary, the recursive T-matrix method [35] [26] gives the exact solution of the multiple scattering by particles considering all orders of interaction, and is one of the most computationally efficient numerical methods. This approach is ideal for disconnected particles, for example, buried rocks and ice particles in the ground. Nevertheless, it is less accurate when describing the scattering from root-like clusters in the soil volume, which we would like to handle in conjunction with the study of soil moisture.

The solution for combinations of the rough surface scattering and discrete random media scattering exist only for two-dimensional (2D) case [36]. Even there, the solution in [36] still manifests the instability due to surface roughness, and only handles simple circular particles. No solution for scattering from rough surfaces with buried root-like clusters exists.

1.3   Thesis Objectives and Contribution

The objective of this dissertation is to construct a computationally efficient model of the electromagnetic scattering from layered ground with vertical dielectric profiles and buried vegetation roots and other inhomogeneities. Such complexity in modeling soil structure scattering has never been fully solved to-date. The contribution details of this dissertation are summarized below:

• **Stabilized extended boundary condition method (SEBCM):** The extended boundary

7

condition method is developed for 3D vector scattering and is stabilized to become a powerful approach for solving the scattering from arbitrarily random rough surfaces. It provides accurate solutions over large surface roughnesses at much higher computational efficiency than fully numerical techniques.

- **3D scattering model of multilayer random rough surfaces:** This is the only known practically applicable multilayer rough surface scattering model valid for large surface roughnesses to-date. It can serve as the forward model in subsurface soil moisture retrievals in the future.

- **3D scattering model from the buried root structures:** This is the first time that scattering contribution of vegetation roots have been investigated in the remote sensing of subsurface soil moisture.

- **Experimental Validation:** Experimental validation of random medium scattering has never been reported elsewhere as far as we known. And the compact remotely controlled radar system does not exist to-date. As well, measurements and analysis of data from a stand-alone remotely-controlled low-altitude radar are novel and open up a new area of future investigation.

1.4   Dissertation Overview

This dissertation consists of four main chapters in addition to the introduction and conclusion chapters. **Chapter 2** presents a solution to 3D electromagnetic scattering from a single arbitrary random rough surface using the stabilized extended boundary condition method (SEBCM). It solves the vector scattered fields in regions both above and below the surface, and thereby calculates the bistatic scattering coefficients of the rough surface. This method addresses the long-existing problem of instability of the classical EBCM and largely improves the validity domain over roughness. Meanwhile, it keeps the high computational efficiency compared to the fully numerical methods, such as the method of mo-

ments (MoM). Theory, formulation and validation with other model results and experimental measurement will be shown in this chapter. The SEBCM also forms one of the basics in the solution of the layered problem, which will be presented in Chapter 3.

Chapter 3 focuses on the solution of 3D scattering from layered rough surfaces with homogeneous media or dielectric profiles. This soluation is based on the scattering matrix approach. By knowing the single rough surface scattering matrix using the SEBCM and the propagation matrix inside the layer medium, the bistatic scattering coefficients of the layered structure are calculated. After extensive validation, a sensitivity study has been performed to understand the model behavior as a function of geophysical parameters, such as layer separation, subsurface roughness, and sublayer dielectric property.

Chapter 4 completes the definition of the ground by considering buried inhomogeneities among layered rough surfaces, such as rocks and vegetation roots. These inhomogeneities are considered as either discrete random media or clusters of scatterers with given patterns. Depending on the scatterers in the clusters, the recursive transition matrix (T-matrix) method or the generalized iterative extended boundary condition method (GIEBCM) is used. The scattering matrix is then found from the transition matrix and included in the layered-medium scattering computation.

With all the theories discussed in the above chapters, **Chapter 5** is dedicated to describe our work on a tower-based radar system and the experiments done with it. This system is a prototype for future low-altitude mobile soil moisture retrieval system. We have tested the system and carried out measurements in actual fields with and without vegetation. Primary results will be shown in this chapter. **Chapter 6** concludes this dissertation and presents recommendations on future work.

CHAPTER 2

Three-dimensional Bistatic Electromagnetic Scattering from Single Surface with Arbitrary Roughness

In this chapter, we develop the Stabilized Extended Boundary Condition method (SE-BCM) based on the classical EBCM to solve the three-dimensional vector electromagnetic scattering problem from arbitrary random rough surfaces. Similar to the classical EBCM, we expand the fields in terms of Floquet modes and match the extended boundary conditions at test surfaces away from the actual rough surface to retrieve the surface currents and therefore the scattered fields. However, to solve long-standing stability problems of the classical EBCM, we introduce a z-coordinate transformation to restrict and control the test surface locations explicitly. We also introduce the concepts of moderated test surface locations and balanced k-charts for further stabilization and optimization of the solutions. The computational efficiency is optimized by judicious sub-matrix decomposition. The resulting bistatic scattering cross-sections are validated by comparing with analytical and numerical solutions. Specifically, the solutions are compared with those from the small perturbation method and small-slope approximation within their validity region, and with those from the method of moments outside the validity domains of analytical solutions. It is shown that SEBCM gives accurate, numerically efficient, full-wave solutions over a large range of surface roughnesses and medium losses, which are far beyond the validity range of analytical methods. These properties are expected to make SEBCM a competitive

forward solver for soil moisture retrieval from radar measurements.

2.1 Introduction

The problem of electromagnetic scattering from arbitrarily random rough surfaces has been a subject of numerous studies over the past several decades for its important applications in microwave remote sensing. Being representative of many naturally occurring surface and subsurface structures such as soil, snow, and ice, the model of electromagnetic scattering from single or multiple-layered random rough surfaces characterizes of the interaction between electromagnetic waves and these remote sensing targets. Currently, one of the major applications of the radar technology is microwave remote sensing of soil moisture where the objective is to map the distributions of soil moisture whose temporal and spatial variations are influential parameters in both climatic and hydrologic models. To provide global measurements of soil moisture, NASA is developing the Soil Moisture Active/Passive (SMAP) [9] mission, which will map the global soil moisture with unprecedented resolution, sensitivity, and area coverage. As one of the main SMAP instruments, a synthetic aperture radar (SAR) operating at L-band will provide measurements with ground resolutions of 1-3 km, sensing the soil conditions for bare to moderately vegetated surfaces. To retrieve the soil properties from radar measurements, accurate and highly efficient inverse algorithms are necessary, which in turn require accurate and efficient radar forward scattering models.

To date, many approaches have been investigated to solve the rough surface scattering problem, including analytical, numerical, and empirical methods. The analytical methods are based on approximation techniques [16], among which the small perturbation method (SPM) and the Kirchhoff approximation (KA) are two of the most widely used. However, although these methods have the highest computational efficiency, their combination cannot cover the entire range of practical problems. The small perturbation method, which is often referred as a low frequency approach, is limited to surfaces with rather small height

variations ($k_0 h_{rms} < 0.3$) and relatively small slopes ($k_0 l_c \sim 1$), where k_0 is the free space wavenumber, h_{rms} is the surface root-mean-squared (rms) height, and l_c is the surface correlation length. Also, the first-order SPM solutions only predict for the co-polarized backscattering cross section. On the other hand, the Kirchhoff approximation, which is referred to as a high frequency method, requires that every point on the rough surface have a large radius of curvature relative to the wavelength ($k_1 h_{rms} < 0.3$ and $\sqrt{2} h_{rms}/l_c < 0.3$ [29], where k_1 is the wavenumber in the medium). Another approach that extends SPM and KA is the small-slope approximation (SSA) [18]. Still, it is limited to surfaces with roughness $h_{rms}/l_c < \min(1/\tan\theta_i, 1/\tan\theta_s)$ (θ_i and θ_s are incidence angle and scattering angle respectively) and tends to underestimate the scattering cross sections at large angles [19].

The numerical solutions typically use differential equation formulations for time-domain approaches ([20, 21]) and surface integral equation formulations for frequency-domain approaches, including method of moments (MoM) ([22–24]), Integral Equation Method (IEM) [37], and Advanced Integral Equation Method (AIEM) [38]. These numerical methods are capable of simulating surfaces with arbitrary roughness; however, their computational cost is typically high, especially for the three-dimensional problem. Besides the methods mentioned above, the empirical formulas are used as well [39] which are based on curve-fitting of experimental data. They are accurate for the particular location used but usually not elsewhere, and lack physical insight.

Having features of both analytical and numerical methods, the extended boundary condition method (EBCM) is an attractive approach due to its expected accuracy and computational efficiency. The 2D EBCM has been developed in [16]. It gives accurate full wave solutions including co-pol and cross-pol components in a fraction of the time needed by numerical methods such as MoM. A preliminary version of the 3D EBCM has been reported in [40] but only used to compute the periodic surface problem. The classical EBCM [16],[40] has not been practically used as a main approach to solve the rough surface scattering problem due to its much smaller validity domain than that being theoretically pre-

dicted. The EBCM matrix system tends to be unstable and ill conditioned when applied to surfaces with large height variations or highly lossy media. This limits the classical EBCM to a practical domain only slightly larger than that of approximate techniques, which give faster analytical solutions.

In this work, based on the classical EBCM, the three-dimensional scattering model named as stabilized EBCM (SEBCM) is developed and stabilized. Using similar principles to the classical EBCM, SEBCM expands the fields in terms of a superposition of Floquet modes and matches the extended boundary conditions (EBC) at test surfaces away from the actual rough surface to retrieve the surface currents, from which the scattered fields are computed. In the classical EBCM formulations, locations of the test surfaces are not explicitly defined. This causes the EBCM matrix system to become unstable, since more and more points of the actual surface may cross the test surfaces as the standard deviation of the surface height increases. To stabilize the classical EBCM, SEBCM introduces a z-coordinate transformation to restrict and control the test surface locations explicitly. Moreover, a significantly enhanced numerical solution for the resulting system is developed to further stabilize and optimize the computations. As a result, the SEBCM can be applied to surfaces with a large range of roughnesses.

Results of SEBCM are compared with the SPM solutions for slightly rough surfaces and the KA solutions for surfaces with large curvature, as well as the SSA solutions for surfaces with larger roughnesses and moderate loss. Additionally, SEBCM solutions are validated by comparing to results given by the method of moments (MoM) for 2D surface with both 2D and 1D roughnesses. All of the comparisons show the agreement of this 3D SEBCM model with other approaches within their limits of validity. The model results are also verified with field observations with very good agreement.

The SEBCM developed here will form the basis of the solution to scattering from layered arbitrary rough surfaces. Also, its large validity range for roughnesses and high computational efficiency make SEBCM a competitive forward solver for soil moisture and roughness retrieval from radar measurements.

2.2 Problem Geometry and Analysis

2.2.1 Problem Geometry
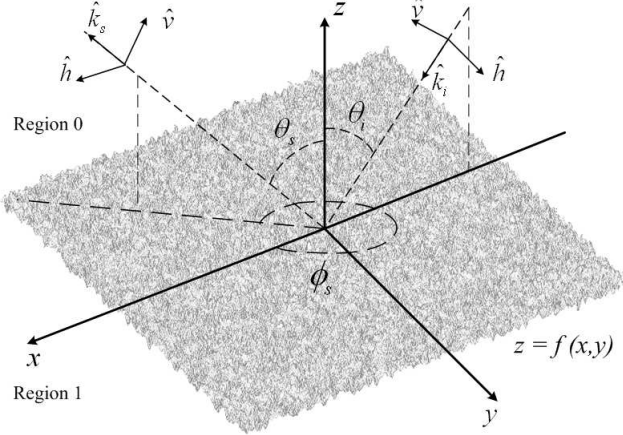
Figure 2.1: Geometry of the problem: scattering from single 2D rough surface

The problem considered here is the 3D bistatic scattering from an arbitrary random rough surface as shown in Figure 2.1. The 2D rough surface f with rms height h_{rms} and correlation length l_c separates free space (region 0, ε_0, μ_0) from a homogenous medium (region 1, ε_1, $\mu_1 = \mu_0$). The z-axis is perpendicular to the mean-plane of the surface. The incidence plane is coincident with the x-z plane and the projection of the incident wave vector points to the positive x-direction. The polarization is defined to be horizontal (H) or TE polarized when the electric field is directed along the y-axis and vertical (V) or TM polarized when the magnetic field is directed along the y-axis. To apply EBCM, the rough surface is assumed to be periodic with a period that is much larger than the correlation length of the surface roughness. The surface profile satisfies

$$f(x,y) = f(x+nL_x, y+mL_y), \quad \forall\, m,n \in \mathbb{Z}$$

where L_x and L_y are periods along the x- and y-directions, respectively. Its maximum and minimum heights are denoted as $f_{max} = \max\{f\}$ and $f_{min} = \min\{f\}$. The differential

surface area and the normal vector to the surface at each point are,

$$dS' = dxdy\sqrt{1 + f_x^2 + f_y^2}$$

$$\hat{n} = \frac{-\hat{x}f_x - \hat{y}f_y + \hat{z}}{\sqrt{1 + f_x^2 + f_y^2}} = \hat{x}n_x + \hat{y}n_y + \hat{z}n_z$$

where f_x and f_y are partial derivatives of the surface profile with respect to the x and y directions, respectively.

2.2.2 Analysis and Formulation

Generation of two-dimensional random rough surface

To implement EBCM, a numerical model for the 2D random rough surface is required. The numerical model of a one-dimensional random rough surface is developed in [41]. It generates the surface by constructing its spectrum. This model is extended to a 2D rough surface and summarized here, the numerical details can be found in Appendix A.

A 2D random rough surface $z = f(x,y)$ is obtained by

- generating an $M \times N$ random number array with standard normal distribution and rearranging it to be a complex array $\{c_{mn}\}$ with real values at cross points of rows $M/2$, M and columns $N/2$, N;

- calculating spectral density $W(K_m, K_n)$ and the matrix of $F_{mn} = 2\pi\sqrt{L_x L_y W(K_m, K_n)} \cdot c_{mn}$;

- computing the rough surface by 2D IFFT from the F_{mn} matrix.

where $K_m = 2\pi m/L_x$ and $K_n = 2\pi n/L_y$.

For the soil rough surfaces, the exponential correlation function with its spectral density,

$$C(\bar{r}_\perp) = \exp\left(-\frac{|\bar{r}_\perp|}{l}\right) \tag{2.1}$$
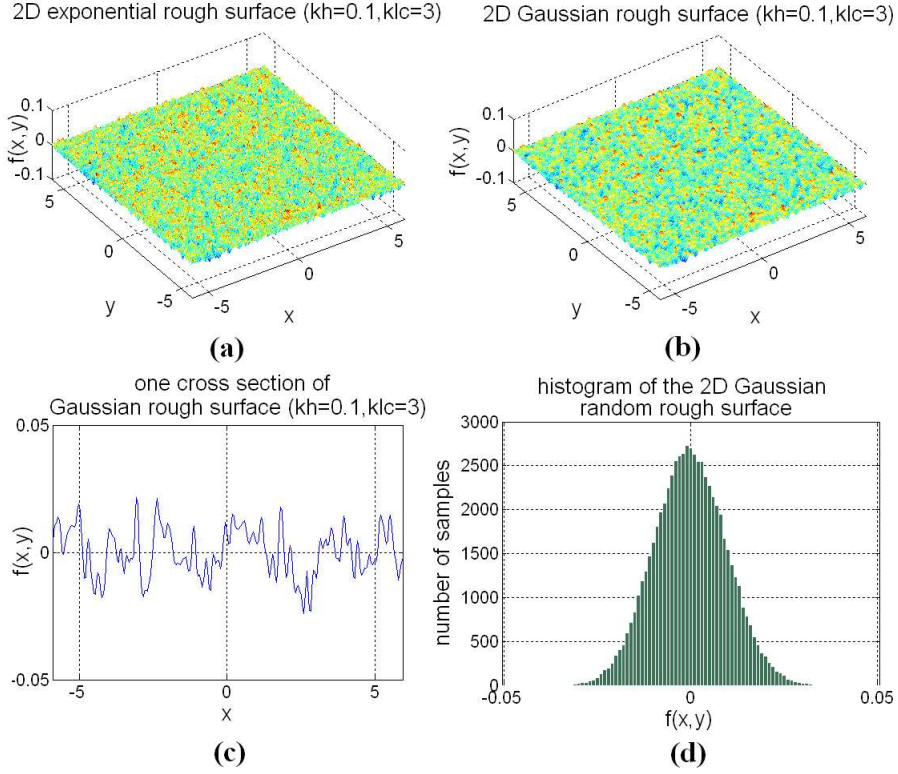
Figure 2.2: Examples of Gaussian random rough surface (dimension of 50λ): (a) with exponential correlation function ($k_0 l_c = 3$ and $k_0 h_{rms} = 0.1$); (b) with Gaussian correlation function ($k_0 l_c = 3$ and $k_0 h_{rms} = 0.1$; (c) cross-cut of the surface in (b); (d) the histogram of the surface in (b).

$$W(\bar{k}_\perp) = \frac{h^2 l^2}{2\pi \left(1 + \bar{k}_\perp^2 l^2\right)^{\frac{3}{2}}} \tag{2.2}$$

appear to better match experimental data than the Gaussian correlation function [42]. Examples of 2D rough surfaces with Gaussian correlation function are shown in Figure 2.2.

Scattering matrix formulation

Scalar solutions to the electromagnetic scattering from 1D periodic single rough surface based on EBCM have been discussed in [16]. In this work, the 3D vector solution to the scattering from a 2D periodic rough surface $f(x,y)$ is developed. The formulation for TE (H-pol) waves is presented here, and the TM (V-pol) wave solution can be obtained

16

through duality. The incident wave with horizontal polarization is $\mathbf{E}_i(\bar{r}) = \hat{y}E_0 e^{i\mathbf{k}_i \cdot \mathbf{r}}$, where the propagation vector $\mathbf{k}_i = k_{ix}\hat{x} + k_{iy}\hat{y} - k_{iz}\hat{z}$. The subscript i denotes the incidence direction.

i. 3D periodic Green's function

The plane wave illuminating one period of the 2D rough surface is

$$E_y(\mathbf{r}' + \hat{x}nL_x + \hat{y}mL_y) = E_y(\mathbf{r}')e^{ik_{ix}nL_x}e^{ik_{iy}mL_y} \tag{2.3}$$

where L_x and L_y are periods along x- and y-directions, respectively. The periodic scalar Green's function in region 0 or 1 is obtained as [16]

$$g_{jp}(\mathbf{r},\mathbf{r}') = \sum_{m,n} g_j(\mathbf{r},\mathbf{r}' + \hat{x}nL_x + \hat{y}mL_y)e^{ik_{ix}nL_x}e^{ik_{iy}mL_y}$$
$$= \frac{i}{2L_xL_y}\sum_{m,n}\frac{1}{k_{jzmn}}e^{ik_{xn}(x-x')+ik_{ym}(y-y')+ik_{jzmn}|z-z'|} \tag{2.4}$$

where $k_{jzmn} = \sqrt{k_j^2 - k_{xn}^2 - k_{ym}^2}$, $k_{xn} = k_{ix} + nK_x$ and $k_{ym} = k_{iy} + mK_y$. From the periodic Green's function, it can be seen that the scattered waves are propagating in discrete Floquet modes with directions determined by k_{xn}, k_{ym} and k_{jzmn}.

ii. Scattering matrix derivation from the extended boundary conditions

Using Green's theorem, the electric field in a source-free region can be obtained by,

$$\mathbf{E}(\mathbf{r}) = \oiint_{s'} dS'\{i\omega\mu g(\mathbf{r},\mathbf{r}')\left[\hat{n} \times \mathbf{H}(\mathbf{r}')\right] + \nabla g(\mathbf{r},\mathbf{r}') \times \left[\hat{n} \times \mathbf{E}(\mathbf{r}')\right]\} \tag{2.5}$$

Utilizing the 3D periodic scalar Green's function and based on the extinction theorem, the total electric fields in region 0 and 1 are as follows:

17

In region 0,

$$
\mathbf{E}^i(\mathbf{r}) + \mathbf{E}_0^s(\mathbf{r}) = \mathbf{E}^i + \int_P dS' \{ i\omega\mu g_{0p}(\mathbf{r},\mathbf{r}') \left[\hat{n} \times \mathbf{H}_0(\mathbf{r}') \right]
$$

$$
+\nabla' g_{0p}(\mathbf{r},\mathbf{r}') \times \left[\hat{n} \times \mathbf{E}_0(\mathbf{r}') \right] \} =
\begin{cases}
\mathbf{E}_0(\mathbf{r}), \ z > f(x,y) \\
0, \qquad z < f(x,y)
\end{cases}
\tag{2.6}
$$

In region 1,

$$
\mathbf{E}_1^s(\mathbf{r}) = - \int_P dS' \{ i\omega\mu g_{1p}(\mathbf{r},\mathbf{r}') \left[\hat{n} \times \mathbf{H}_1(\mathbf{r}') \right]
$$

$$
+\nabla' g_{1p}(\mathbf{r},\mathbf{r}') \times \left[\hat{n} \times \mathbf{E}_1(\mathbf{r}') \right] \} =
\begin{cases}
0, \qquad z > f(x,y) \\
\mathbf{E}_1(\mathbf{r}), \ z < f(x,y)
\end{cases}
\tag{2.7}
$$

Considering the fields at test surfaces where z is larger than the maximum surface height f_{max} or smaller than the minimum surface height f_{min}, $|z - z'|$ becomes $z - z'$ for $z > f_{max}$ and $-(z - z')$ for $z < f_{min}$. We express the scattered fields as the summation of Floquet modes using the periodic Green's function in Eq.2.4.

In region 0, this gives

$$
\mathbf{E}_0(\mathbf{r}) = \mathbf{E}^i(\mathbf{r}) + \sum_{m,n} \mathbf{b}_{mn}^{(0)} \frac{e^{i\mathbf{k}_{0mn}^+ \cdot \mathbf{r}}}{k_{0mnz}^2} \quad z > f_{max}
\tag{2.8}
$$

$$
0 = \mathbf{E}^i(\mathbf{r}) - \sum_{m,n} \mathbf{a}_{mn}^{(0)} \frac{e^{i\mathbf{k}_{0mn}^- \cdot \mathbf{r}}}{k_{0mnz}^2} \quad z < f_{min}
\tag{2.9}
$$

In region 1, we have

$$
0 = - \sum_{m,n} \mathbf{b}_{mn}^{(1)} \frac{e^{i\mathbf{k}_{1mn}^+ \cdot \mathbf{r}}}{k_{1mnz}^2} \quad z > f_{max}
\tag{2.10}
$$

$$
\mathbf{E}_1(\mathbf{r}) = \sum_{m,n} \mathbf{a}_{mn}^{(1)} \frac{e^{i\mathbf{k}_{1mn}^- \cdot \mathbf{r}}}{k_{1mnz}^2} \quad z < f_{min}
\tag{2.11}
$$

where $\mathbf{a}_{mn}^{(j)}$ and $\mathbf{b}_{mn}^{(j)}$ are the Floquet mode coefficients in region $j = 0, 1$, and the propagation

18

vector $\mathbf{k}_{jmn}^{\pm} = \hat{x}k_{xn} + \hat{y}k_{ym} \pm \hat{z}k_{jzmn}$. Eq.(2.9) and Eq.(2.10) are referred to as the extended boundary conditions. With $dS'\nabla'e^{-i\mathbf{k}_{jmn}^{\pm}\cdot\mathbf{r}'} \times \hat{n} \times \mathbf{E}(\mathbf{r}') = -idS'\left(\mathbf{k}_{jmn}^{\pm} \times \hat{n} \times \mathbf{E}\right)e^{-i\mathbf{k}_{jmn}^{\pm}\cdot\mathbf{r}'}$, we find

$$b_{mnx}^{(j)} = \frac{ik_{jzmn}}{2L_xL_y} \cdot \int_p dS' \left\{ -i[k_{ym}\hat{z}\cdot(\hat{n}\times\mathbf{E}_j) - k_{jzmn}\hat{y}\cdot(\hat{n}\times\mathbf{E}_j)]e^{-i\mathbf{k}_{jmn}^{+}\cdot\mathbf{r}'} \right.$$
$$\left. +e^{-i\mathbf{k}_{jmn}^{+}\cdot\mathbf{r}'}\hat{x}\cdot[\hat{n}\times\nabla'\times\mathbf{E}_j] \right\} \tag{2.12}$$

$$b_{mny}^{(j)} = \frac{ik_{jzmn}}{2L_xL_y} \cdot \int_p dS' \left\{ -i[k_{jzmn}\hat{x}\cdot(\hat{n}\times\mathbf{E}_j) - k_{xn}\hat{z}\cdot(\hat{n}\times\mathbf{E}_j)]e^{-i\mathbf{k}_{jmn}^{+}\cdot\mathbf{r}'} \right.$$
$$\left. +e^{-i\mathbf{k}_{jmn}^{+}\cdot\mathbf{r}'}\hat{y}\cdot[\hat{n}\times\nabla'\times\mathbf{E}_j] \right\} \tag{2.13}$$

$$b_{mnz}^{(j)} = \frac{ik_{jzmn}}{2L_xL_y} \cdot \int_p dS' \left\{ -i[k_{xn}\hat{y}\cdot(\hat{n}\times\mathbf{E}_j) - k_{ym}\hat{x}\cdot(\hat{n}\times\mathbf{E}_j)]e^{-i\mathbf{k}_{jmn}^{+}\cdot\mathbf{r}'} \right.$$
$$\left. +e^{-i\mathbf{k}_{jmn}^{+}\cdot\mathbf{r}'}\hat{z}\cdot[\hat{n}\times\nabla'\times\mathbf{E}_j] \right\} \tag{2.14}$$

and

$$a_{mnx}^{(j)} = -\frac{ik_{jzmn}}{2L_xL_y} \cdot \int_p dS' \left\{ -i[k_{ym}\hat{z}\cdot(\hat{n}\times\mathbf{E}_j) + k_{jzmn}\hat{y}\cdot(\hat{n}\times\mathbf{E}_j)]e^{-i\mathbf{k}_{jmn}^{-}\cdot\mathbf{r}'} \right.$$
$$\left. +e^{-i\mathbf{k}_{jmn}^{-}\cdot\mathbf{r}'}\hat{x}\cdot[\hat{n}\times\nabla'\times\mathbf{E}_j] \right\} \tag{2.15}$$

$$a_{mny}^{(j)} = -\frac{ik_{jzmn}}{2L_xL_y} \cdot \int_p dS' \left\{ i[k_{jzmn}\hat{x}\cdot(\hat{n}\times\mathbf{E}_j) + k_{xn}\hat{z}\cdot(\hat{n}\times\mathbf{E}_j)]e^{-i\mathbf{k}_{jmn}^{-}\cdot\mathbf{r}'} \right.$$
$$\left. +e^{-i\mathbf{k}_{jmn}^{-}\cdot\mathbf{r}'}\hat{y}\cdot[\hat{n}\times\nabla'\times\mathbf{E}_j] \right\} \tag{2.16}$$

$$a_{mnz}^{(j)} = -\frac{ik_{jzmn}}{2L_xL_y} \cdot \int_p dS' \left\{ -i[k_{xn}\hat{y}\cdot(\hat{n}\times\mathbf{E}_j) - k_{ym}\hat{x}\cdot(\hat{n}\times\mathbf{E}_j)]e^{-i\mathbf{k}_{jmn}^{-}\cdot\mathbf{r}'} \right.$$
$$\left. +e^{-i\mathbf{k}_{jmn}^{-}\cdot\mathbf{r}'}\hat{z}\cdot[\hat{n}\times\nabla'\times\mathbf{E}_j] \right\} \tag{2.17}$$

We now perform a z-transformation to ensure the solutions obtained from the extended boundary conditions are physical. To impose the restriction of test surface locations, we let $u = z - f_{min}$ and $v = z - f_{max}$, therefore, $u < 0$ when $z < f_{min}$ and $v > 0$ when $z > f_{max}$. The transformed expressions of the fields are:

In region 0,

$$\mathbf{E}_0(\mathbf{r}) = \mathbf{E}^i(\mathbf{r}) + \sum_{m,n} \mathbf{B}_{mn}^{(0)} \frac{e^{i\mathbf{k}_{0mn}^+ \cdot \mathbf{r}}}{k_{0mnz}^2} \quad v > 0 \tag{2.18}$$

$$0 = \mathbf{E}^i(\mathbf{r}) - \sum_{m,n} \mathbf{A}_{mn}^{(0)} \frac{e^{i\mathbf{k}_{0mn}^- \cdot \mathbf{r}}}{k_{0mnz}^2} \quad u < 0 \tag{2.19}$$

In region 1,

$$0 = -\sum_{m,n} \mathbf{B}_{mn}^{(1)} \frac{e^{i\mathbf{k}_{1mn}^+ \cdot \mathbf{r}}}{k_{1mnz}^2} \quad v > 0 \tag{2.20}$$

$$\mathbf{E}_1(\mathbf{r}) = \sum_{m,n} \mathbf{A}_{mn}^{(1)} \frac{e^{i\mathbf{k}_{1mn}^- \cdot \mathbf{r}}}{k_{1mnz}^2} \quad u < 0 \tag{2.21}$$

where the propagation vector $\mathbf{k}_{jmn}^{\pm} = \hat{x}k_{xn} + \hat{y}k_{ym} \pm \hat{z}k_{jzmn}$, and

$$\mathbf{B}_{mn}^{(0)} = \mathbf{b}_{mn}^{(0)} e^{ik_{0nz}f_{max}}$$

$$\mathbf{A}_{mn}^{(0)} = \mathbf{a}_{mn}^{(0)} e^{-ik_{0nz}f_{min}}$$

$$\mathbf{B}_{mn}^{(1)} = \mathbf{b}_{mn}^{(1)} e^{ik_{1nz}f_{max}}$$

$$\mathbf{A}_{mn}^{(1)} = \mathbf{a}_{mn}^{(1)} e^{-ik_{1nz}f_{min}}$$

The surface fields can be written in terms of Fourier series as follows, with the Fourier coefficients are unknowns to be solved:

$$dS' \left(\hat{n} \times \mathbf{E}_j(\mathbf{r}') \right) = dxdy \sum_{p,q} 2\boldsymbol{\alpha}_{pq}^{(j)} e^{i\left(k_{xq}x + k_{yp}y\right)} \tag{2.22}$$

$$dS' \left[\hat{n} \times \left(\nabla' \times \mathbf{E}_j(\mathbf{r}') \right) \right] = dxdy \sum_{p,q} 2\boldsymbol{\beta}_{pq}^{(j)} e^{i\left(k_{xq}x + k_{yp}y\right)} \tag{2.23}$$

where $\boldsymbol{\alpha}_{pq}^{(j)} = \hat{x}\alpha_{pqx}^{(j)} + \hat{y}\alpha_{pqy}^{(j)} + \hat{z}\alpha_{pqz}^{(j)}$ and $\boldsymbol{\beta}_{pq}^{(j)} = \hat{x}\beta_{pqx}^{(j)} + \hat{y}\beta_{pqy}^{(j)} + \hat{z}\beta_{pqz}^{(j)}$. The continuity of the tangential electric and magnetic fields implies that $\boldsymbol{\alpha}_{pq}^{(0)} = \boldsymbol{\alpha}_{pq}^{(1)} = \boldsymbol{\alpha}_{pq}$ and $\boldsymbol{\beta}_{pq}^{(0)} = \boldsymbol{\beta}_{pq}^{(1)} = \boldsymbol{\beta}_{pq}$. Moreover, components of the unknown $\bar{\boldsymbol{\alpha}}$ and $\bar{\boldsymbol{\beta}}$ are not totally independent; their z-components can be expressed as:

$$\bar{\alpha}_z = f_x\bar{\alpha}_x + f_y\bar{\alpha}_y$$
$$\bar{\beta}_z = f_x\bar{\beta}_x + f_y\bar{\beta}_y$$

The extended boundary conditions and the known incident wave $\mathbf{E}^i = \hat{y}E_0 e^{i\mathbf{k}_i \cdot \mathbf{r}}$ restrict the Floquet mode coefficients to be

$$\begin{cases} A_{mnx}^{(0)} = 0 \\ A_{mny}^{(0)} = \delta_{m0}\delta_{ni}k_{0iz}^2 E_0 e^{-ik_{0iz}f_{min}} \\ A_{mnz}^{(0)} = 0 \end{cases} \qquad \begin{cases} B_{mnx}^{(1)} = 0 \\ B_{mny}^{(1)} = 0 \\ B_{mnz}^{(1)} = 0 \end{cases}$$

With the diagonal matrices

$$\begin{aligned} D_a^{(0)} &= \left[e^{-ik_{0nz}f_{min}} \right] \\ D_b^{(0)} &= \left[e^{ik_{0nz}f_{max}} \right] \\ D_a^{(1)} &= \left[e^{-ik_{1nz}f_{min}} \right] \\ D_b^{(1)} &= \left[e^{ik_{1nz}f_{max}} \right] \end{aligned}$$

the surface fields can be obtained by solving for α and β from:

$$\begin{bmatrix} D_a^{(0)} & 0 & 0 & 0 \\ 0 & D_a^{(0)} & 0 & 0 \\ 0 & 0 & D_b^{(1)} & 0 \\ 0 & 0 & 0 & D_b^{(1)} \end{bmatrix} \cdot \bar{\bar{T}} \cdot \begin{pmatrix} \bar{\alpha}_x \\ \bar{\alpha}_y \\ \bar{\beta}_x \\ \bar{\beta}_y \end{pmatrix} = \begin{pmatrix} \bar{A}_x^{(0)} \\ \bar{A}_y^{(0)} \\ \bar{B}_x^{(1)} \\ \bar{B}_y^{(1)} \end{pmatrix} \tag{2.24}$$

where

$$\bar{\bar{T}} = \frac{1}{L_x L_y} \begin{pmatrix} \bar{\bar{Q}}^-_{0Nxx} & \bar{\bar{Q}}^-_{0Nxy} & \bar{\bar{Q}}^-_{0Dxx} & 0 \\ \bar{\bar{Q}}^-_{0Nyx} & \bar{\bar{Q}}^-_{0Nyy} & 0 & \bar{\bar{Q}}^-_{0Dyy} \\ \bar{\bar{Q}}^+_{1Nxx} & \bar{\bar{Q}}^+_{1Nxy} & \bar{\bar{Q}}^+_{1Dxx} & 0 \\ \bar{\bar{Q}}^+_{1Nyx} & \bar{\bar{Q}}^+_{1Nyy} & 0 & \bar{\bar{Q}}^+_{1Dyy} \end{pmatrix} \tag{2.25}$$

The scattered and transmitted fields can be obtained by evaluating,

$$\begin{pmatrix} \bar{B}^{(0)}_x \\ \bar{B}^{(0)}_y \\ \bar{B}^{(0)}_z \\ \bar{A}^{(1)}_x \\ \bar{A}^{(1)}_y \\ \bar{A}^{(1)}_z \end{pmatrix} = \begin{bmatrix} D^{(0)}_b & 0 & 0 & 0 & 0 & 0 \\ 0 & D^{(0)}_b & 0 & 0 & 0 & 0 \\ 0 & 0 & D^{(0)}_b & 0 & 0 & 0 \\ 0 & 0 & 0 & D^{(1)}_a & 0 & 0 \\ 0 & 0 & 0 & 0 & D^{(1)}_a & 0 \\ 0 & 0 & 0 & 0 & 0 & D^{(1)}_a \end{bmatrix} \cdot \bar{\bar{P}} \cdot \begin{pmatrix} \bar{\alpha}_x \\ \bar{\alpha}_y \\ \bar{\beta}_x \\ \bar{\beta}_y \end{pmatrix} \tag{2.26}$$

where

$$\bar{\bar{P}} = \frac{1}{L_x L_y} \begin{pmatrix} \bar{\bar{Q}}^+_{0Nxx} & \bar{\bar{Q}}^+_{0Nxy} & \bar{\bar{Q}}^+_{0Dxx} & 0 \\ \bar{\bar{Q}}^+_{0Nyx} & \bar{\bar{Q}}^+_{0Nyy} & 0 & \bar{\bar{Q}}^+_{0Dyy} \\ \bar{\bar{Q}}^+_{0Nzx} & \bar{\bar{Q}}^+_{0Nzy} & \bar{\bar{Q}}^+_{0Dzx} & \bar{\bar{Q}}^+_{0Dzy} \\ \bar{\bar{Q}}^-_{1Nxx} & \bar{\bar{Q}}^-_{1Nxy} & \bar{\bar{Q}}^-_{1Dxx} & 0 \\ \bar{\bar{Q}}^-_{1Nyx} & \bar{\bar{Q}}^-_{1Nyy} & 0 & \bar{\bar{Q}}^-_{1Dyy} \\ \bar{\bar{Q}}^-_{1Nzx} & \bar{\bar{Q}}^-_{1Nzy} & \bar{\bar{Q}}^-_{1Dzx} & \bar{\bar{Q}}^-_{1Dzy} \end{pmatrix} \tag{2.27}$$

The matrix entries in each sub-matrix block are shown in Eq.(2.28) and Eq.(2.29), where

$$I^\pm_j = \int_p dx dy e^{-i\left[(k_{xn}-k_{xq})x'+(k_{ym}-k_{yp})y'\pm k_{jzmn}f(x',y')\right]} \tag{2.30}$$

Details of this derivation are shown in Appendix B. The scattering matrix is the matrix product shown in Eq.(2.31). Direct derivation of the matrix $\bar{\bar{T}}$ suggests that it has dimensions of 6×4 $\bar{\bar{Q}}$ sub-matrix blocks. However, the rows of sub-matrix blocks are related by the divergence-free condition in the source-free region. Therefore, the matrix $\bar{\bar{T}}$ is repre-

sented uniquely of four blocks by four independent blocks of sub-matrices as in expression (2.25).

iii. Computation of bistatic scattering cross section

In [41], the relationship between bistatic scattering cross section and the Floquet mode coefficients of the upward-propagating fields is derived for the two-dimensional scattering problem. The bistatic scattering cross section for the three-dimensional scenario is derived here.

Considering the incident wave to be h-polarized (TE wave), the incident power density is

$$S_{inc} = \frac{|E_{y0}^i|^2}{2\eta}\cos\theta_i = \frac{\cos\theta_i}{2\eta} \quad \text{for } E_{y0}^i = 1 \tag{2.32}$$

$$Q_{0Nxx,\atop mnpq}^{\pm} = -k_{ym}(k_{xn}-k_{xq})I_0^{\pm}, \; Q_{0Nxy,\atop mnpq}^{\pm} = -\left(k_{ym}(k_{ym}-k_{yp})+k_{0zmn}^2\right)I_0^{\pm}, \; Q_{0Dxx,\atop mnpq}^{\pm} = \pm ik_{0zmn}\left(\frac{k_0 Z_0}{k_1 Z_1}\right)I_0^{\pm}$$

$$Q_{0Nyx,\atop mnpq}^{\pm} = \left(k_{xn}(k_{xn}-k_{xq})+k_{0zmn}^2\right)I_0^{\pm}, \; Q_{0Nyy,\atop mnpq}^{\pm} = k_{xn}(k_{ym}-k_{yp})I_0^{\pm}, \; Q_{0Dyy,\atop mnpq}^{\pm} = \pm ik_{0zmn}\left(\frac{k_0 Z_0}{k_1 Z_1}\right)I_0^{\pm} \tag{2.28}$$

$$Q_{0Nzx,\atop mnpq}^{\pm} = \mp k_{ym}k_{0zmn}I_0^{\pm}, \; Q_{0Nzy,\atop mnpq}^{\pm} = \pm k_{xn}k_{0zmn}I_0^{\pm}, \; Q_{0Dzx,\atop mnpq}^{\pm} = -i(k_{xn}-k_{xq})I_0^{\pm}, \; Q_{0Dzy,\atop mnpq}^{\pm} = -i(k_{ym}-k_{yp})I_0^{\pm}$$

$$Q_{1Nxx,\atop mnpq}^{\pm} = -k_{ym}(k_{xn}-k_{xq})I_1^{\pm}, \; Q_{1Nxy,\atop mnpq}^{\pm} = -\left(k_{ym}(k_{ym}-k_{yp})+k_{1zmn}^2\right)I_1^{\pm}, \; Q_{1Dxx,\atop mnpq}^{\pm} = \pm ik_{1zmn}I_1^{\pm}$$

$$Q_{1Nyx,\atop mnpq}^{\pm} = \left(k_{xn}(k_{xn}-k_{xq})+k_{1zmn}^2\right)I_1^{\pm}, \; Q_{1Nyy,\atop mnpq}^{\pm} = k_{xn}(k_{ym}-k_{yp})I_1^{\pm}, \; Q_{1Dyy,\atop mnpq}^{\pm} = \pm ik_{1zmn}I_1^{\pm} \tag{2.29}$$

$$Q_{1Nzx,\atop mnpq}^{\pm} = \mp k_{ym}k_{1zmn}I_1^{\pm}, \; Q_{1Nzy,\atop mnpq}^{\pm} = \pm k_{xn}k_{1zmn}I_1^{\pm}, \; Q_{1Dzx,\atop mnpq}^{\pm} = -i(k_{xn}-k_{xq})I_1^{\pm}, \; Q_{1Dzy,\atop mnpq}^{\pm} = -i(k_{ym}-k_{yp})I_1^{\pm}$$

$$\bar{\bar{S}} = \begin{bmatrix} D_b^{(0)} & 0 & 0 & 0 & 0 & 0 \\ 0 & D_b^{(0)} & 0 & 0 & 0 & 0 \\ 0 & 0 & D_b^{(0)} & 0 & 0 & 0 \\ 0 & 0 & 0 & D_a^{(1)} & 0 & 0 \\ 0 & 0 & 0 & 0 & D_a^{(1)} & 0 \\ 0 & 0 & 0 & 0 & 0 & D_a^{(1)} \end{bmatrix} \cdot \bar{\bar{P}} \cdot \bar{\bar{T}}^{-1} \cdot \begin{bmatrix} D_a^{(0)} & 0 & 0 & 0 \\ 0 & D_a^{(0)} & 0 & 0 \\ 0 & 0 & D_b^{(1)} & 0 \\ 0 & 0 & 0 & D_b^{(1)} \end{bmatrix}^{-1} \tag{2.31}$$

23

At the observation direction (ϕ_s, θ_s), the h-polarized scattered field is

$$E_{hh}^s = E_\phi^s = \hat{\phi} \cdot (\hat{x} E_x^s + \hat{y} E_y^s + \hat{z} E_z^s) = -E_x^s \sin\phi_s + E_y^s \cos\phi_s \qquad (2.33)$$

and the v-polarized scattered wave is

$$E_{vh}^s = E_\theta^s = \hat{\theta} \cdot (\hat{x} E_x^s + \hat{y} E_y^s + \hat{z} E_z^s) = E_x^s \cos\theta_s \cos\phi_s + E_y^s \cos\theta_s \sin\phi_s - E_z^s \sin\theta_s \qquad (2.34)$$

From Eq.2.9, we let $E_{hh}^s = \sum\limits_{m,n} b_{mn\phi}^{(h)} e^{i\mathbf{k}_{0mn}^+ \cdot \mathbf{r}}$ and $E_{vh}^s = \sum\limits_{m,n} b_{mn\theta}^{(h)} e^{i\mathbf{k}_{0mn}^+ \cdot \mathbf{r}}$, where

$$b_{mn\phi}^{(h)} = -\frac{b_{mnx}}{k_{0mnz}^2} \sin\phi_s + \frac{b_{mny}}{k_{0mnz}^2} \cos\phi_s \qquad (2.35)$$

$$b_{mn\theta}^{(h)} = \frac{b_{mnx}}{k_{0mnz}^2} \cos\theta_s \cos\phi_s + \frac{b_{mny}}{k_{0mnz}^2} \cos\theta_s \sin\phi_s - \frac{b_{mnz}}{k_{0mnz}^2} \sin\theta_s \qquad (2.36)$$

Then the time-averaged fractional powers contained in the scattered wave are

$$P_{mn}^{hh} = |b_{mn\phi}^{(h)}|^2 \frac{k_{0zmn}}{k_0} \text{ and } P_{mn}^{vh} = |b_{mn\theta}^{(h)}|^2 \frac{k_{0zmn}}{k_0}$$

Using the transformation between discrete and continuous domains[41], we have

$$\frac{L_x L_y}{4\pi^2} \iint dk_{xn} dk_{ym} (\cdot) = \frac{L_x L_y}{4\pi^2} \iint d\theta_s d\phi_s \begin{vmatrix} \frac{\partial k_{xn}}{\partial \phi_s} & \frac{\partial k_{xn}}{\partial \theta_s} \\ \frac{\partial k_{ym}}{\partial \phi_s} & \frac{\partial k_{ym}}{\partial \theta_s} \end{vmatrix} (\cdot) \qquad (2.37)$$

The total scattered power of HH is

$$\sum_{m,n} P_{mn}^{hh} = \frac{L_x L_y}{4\pi^2 \cos\theta_i} \iint d\theta_s d\phi_s k_0^2 \sin\theta_s \cos^2\theta_s |b_{mn\phi}|^2$$

$$= \iint d\theta_s d\phi_s \sin\theta_s \sigma_{hh}(\theta_s, \phi_s) \qquad (2.38)$$

Therefore,

$$\sigma_{hh}(\theta_s, \phi_s) = \frac{L_x L_y k_0^2}{4\pi^2 \cos\theta_i} \cos^2\theta_s |b_{mn\phi}^{(h)}|^2 \qquad (2.39)$$

24

Similarly,

$$\sigma_{vh}(\theta_s, \phi_s) = \frac{L_x L_y k_0^2}{4\pi^2 \cos\theta_i} \cos^2\theta_s |b_{mn\theta}^{(h)}|^2 \tag{2.40}$$

Same derivation can be applied for the incident TM wave (v-pol). The 3D bistatic scattering cross sections are

$$\sigma_{hv}(\theta_s, \phi_s) = \frac{L_x L_y k_0^2}{4\pi^2 \cos\theta_i} \cos^2\theta_s |b_{mn\phi}^{(v)}|^2 \tag{2.41}$$

$$\sigma_{vv}(\theta_s, \phi_s) = \frac{L_x L_y k_0^2}{4\pi^2 \cos\theta_i} \cos^2\theta_s |b_{mn\theta}^{(v)}|^2 \tag{2.42}$$

with

$$b_{mn\phi}^{(v)} = \frac{b_{mnx}}{k_{0mnz}^2} \cos\theta_s \cos\phi_s + \frac{b_{mny}}{k_{0mnz}^2} \cos\theta_s \sin\phi_s - \frac{b_{mnz}}{k_{0mnz}^2} \sin\theta_s \tag{2.43}$$

$$b_{mn\theta}^{(v)} = -\frac{b_{mnx}}{k_{0mnz}^2} \sin\phi_s + \frac{b_{mny}}{k_{0mnz}^2} \cos\phi_s \tag{2.44}$$

2.2.3 Numerical Stabilization

In addition to modifying the classical EBCM formulation to explicitly impose conditions at the test surfaces, we have developed techniques for stabilizing the numerical solution of EBCM. This further extends the validity regime of SEBCM.

Moderated test surface locations

In the classical EBCM formulation, the ill-conditioning is caused by the behavior of the matrix $\bar{\bar{T}}$, which is directly computed from the actual rough surface. As shown in above SEBCM formulation (Eq.(2.31)), we impose the test surface conditions on the matrix $\bar{\bar{T}}$ by operating on it with $\bar{\bar{D}}$, resulting in the product $\bar{\bar{D}} \cdot \bar{\bar{T}}$, where $\bar{\bar{D}}$ is the diagonal matrix containing the test surface conditions. Instead of inverting the ill-conditioned matrix $\bar{\bar{T}}$, the matrix $\bar{\bar{D}} \cdot \bar{\bar{T}}$ is inverted. This can be thought of as a regularization scheme: when the classical EBCM system becomes ill-conditioned, there is mathematically more

than one solution to the system. By explicitly defining the test surfaces, the solution space is constrained to make the solution unique, thereby, the matrix system $(\bar{\bar{D}} \cdot \bar{\bar{T}})$ is stabilized. Moreover, though the condition is imposed that the test surfaces should be outside (f_{min}, f_{max}), large distances between test surfaces and the actual surface will also cause ill-conditioning of the matrix $\bar{\bar{T}}$, especially in a lossy medium, since more and more modes fail to reach the test surfaces. Thus, a coordinate transformation margin Δ is defined as $\Delta < min\{|f_{max} - h_{rms}|, |f_{min} - h_{rms}|\}$. The test surfaces will be outside $(f_{min} + \Delta, f_{max} - \Delta)$, which postpones the occurrence of ill-conditioning.

Balanced k-chart with controllable k-boundary

In standard EBCM algorithms, the Floquet modes used to expand the fields are defined symmetrically with respect to the incident field, i.e, mode 0 of the incoming wave is in the direction of the incident field. In terms of a k-chart, this means an unbalanced arrangement of the Floquet modes in k-space. Many evanescent modes are (unnecessarily) included in the matrix computation, which causes the matrix to become rapidly ill-conditioned as the roughness increases. To avoid this, the k-chart is balanced as illustrated in Figure 2.3 (in 2D) and Figure 2.4 (in 3D) where the 0-mode is along the k_z axis. As a trade-off for this balancing, the back-scattering direction will not exactly coincide with one of the Floquet modes. Therefore, an 'angle tolerance' is defined as one of the criteria in computing the surface periods and the number of Floquet modes, which is the largest allowable angle difference between back-scattering direction and its nearest mode.

In addition, as shown in Figure 2.3(b) which is in 2D for illustration, a k-boundary is set to determine the Floquet modes involved in the computation. The k-boundary can be used to exclude the modes at large transmitting angles that are not able to reach the test surfaces due to the loss in region 1. This effectively stabilizes the system for lossy cases. In the lossy cases, the contraction of the k-boundary is related to the medium loss and surface roughness as shown in Figure 2.5. The more lossy the medium is, the less information can arrive at test surfaces. The k-boundary is set to exclude those attenuated

(a) unbalanced k-chart

(b) balanced k-chart
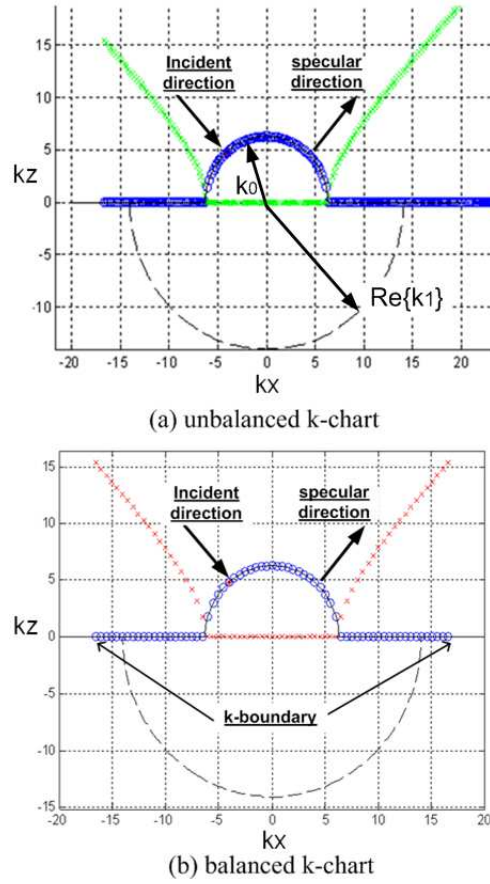
Figure 2.3: k-chart in 2D problem, where circle- and cross-markers indicate the real and imaginary parts of the mode propagation coefficients. The scattered modes on the upper half circle with the radius k_0 are propagation modes in region 0; and the lower half circle with the radius $\text{Re}\{k_I\}$ indicates the propagating transmitted modes in region 1. Evanescent modes in region 0 fall on the k_x-axis outside the upper half circle. (a) shows the unbalanced k-chart with 0-mode being at the specular direction; (b) shows the balanced k-chart; the 0-mode is at k_z-axis, i.e. the mode distribution is symmetric, based on which the k-boundary determines the modes included in the computation.

modes vanishing at the test surfaces, which happen to the higher order modes first. Hence, the new k-boundary is defined as a function of the media loss and the distance between test surfaces and the actual surface, for which, we introduce the linear product of these two factors as $D_t = 2\text{Im}\{k_I\} \cdot \text{Re}\{k_I\} \cdot f_{min}$, where $\text{Im}\{k_I\}$ represents the media loss and $\text{Re}\{k_I\}f_{min}$ describes the distance to the test surface appearing in medium 1. The new k-
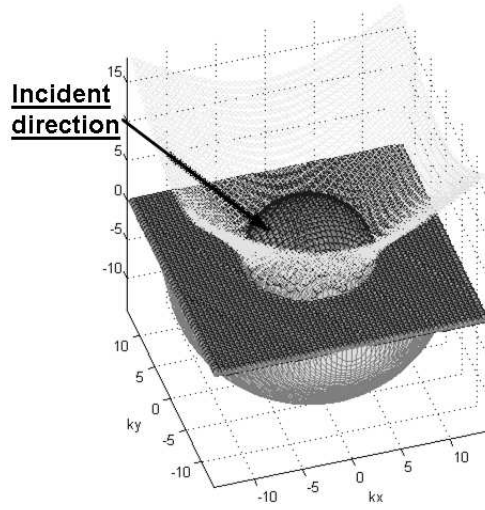
Figure 2.4: Balanced k-chart in 3D: similar as in the 2D case (Figure 2.3), in the 3D k-chart, the propagation modes in both regions are indicated by the upper half sphere (radius is k_0) and the lower half sphere (radius is $\mathrm{Re}\{k_I\}$). The k-boundary becomes a circle in k_x-k_y plane.
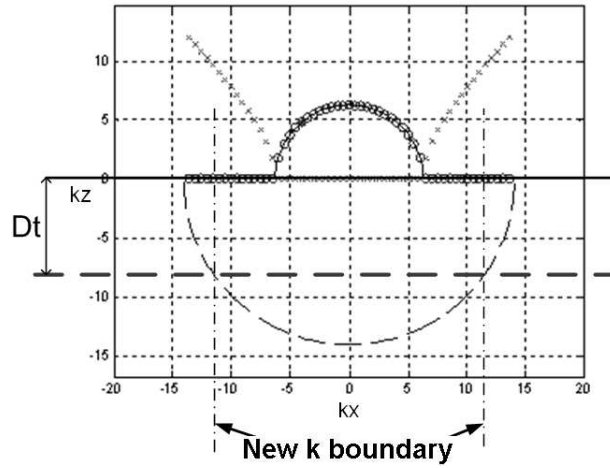
Figure 2.5: The relation between k-boundary and D_t is illustrated in 2D. In the case of lossy medium, the k-boundary is determined considering the medium loss (in D_t).

boundary used in the computation is $k_{bdry} = \sqrt{\mathrm{Re}\{k_I\}^2 - D_t^2}$. However, since the k_{bdry} is required to determine the surface, i.e, f_{min}, instead of $\mathrm{Re}\{k_I\}f_{min}$, a modified quantity $\mathrm{Re}\{k_I\}h_{rms} \cdot \alpha$ is used, where α is the estimated ratio between f_{min} and the rms height.

28

Other numerical improvements

Besides the above considerations, when setting an angle tolerance for the back-scattering calculation a variable total number of Floquet modes can be used in computation, so that depending on the available computing power, solutions with a pre-specified (larger) error can still be obtained with relatively small computational resources.

Moreover, a 'corner margin' is introduced as one of the criteria in the determination of the surface periods. The 'corner margin' is used to remove the singularity caused by the Floquet modes at the transition edge from propagating modes to evanescent modes. In the 3D case, the singularity occurs at the propagating modes having the largest $k_{0mnx}^2 + k_{0mny}^2$ and $k_{1mnx}^2 + k_{1mny}^2$.

Additionally, when determining the surface periods and the number of Floquet modes used in computation, there are many pairs of values satisfying a given angle tolerance and corner margin. Therefore, a limit on the number of Floquet modes N_{limit} is introduced depending on the computational resources available. The more Floquet modes are allowed, the larger the resulting surface periods will be, and therefore the better accuracy the solutions will have. For a given N_{limit}, solutions with less accuracy can still be calculated if desired, with moderate computing power.

Optimization for computational efficiency

One of the challenges in implementing the EBCM algorithm for 3D scattering problems is the large computational load for both memory and computing time. In this work, the computation efficiency is improved by decomposition of loop operations into matrix operations and the matrix operation is further broken down into operations based on sub-matrix blocks of small size.

Firstly, the integral (2.30) is usually calculated through Fourier transformation of the power series expansion of the exponential term $e^{\pm ik_{jzmn}f(x,y)}$. This approach can be further decomposed into a matrix operation by observing that the integral term of the entry $Q_{mnpq}^{\pm}$

is

$$I^{\pm}_{j,mnpq} = \sum_{h=0}^{N_{tr}} FFT \left(\frac{(\pm ik_{jzmn}f(x,y))^h}{h!} \right)$$

$$= \sum_{h=0}^{N_{tr}} \frac{(\pm ik_{jzmn})^h}{h!} FFT(f^h(x,y)) \tag{2.45}$$

where N_{tr} is the number of terms in the truncated power series. Let N denote the number of Floquet modes. The first expression in Eq.(2.45) requires $(2N+1)^2$ FFT operations. However, as implied by the second expression in Eq.(2.45), we can construct a $N_{tr} \times (4N+1)^2$ matrix $\bar{\bar{F}}$ as

$$\bar{\bar{F}} = \begin{pmatrix} FFT(f^0(x,y)) \\ FFT(f^1(x,y)) \\ FFT(f^2(x,y)) \\ \vdots \\ FFT(f^{N_{tr}}(x,y)) \end{pmatrix} \tag{2.46}$$

where each row is the Fourier transform expressed in a row vector. We can also construct a $(2N+1)^2 \times N_{tr}$ matrix $\bar{\bar{K}}^{\pm}_j$ as

$$\bar{\bar{K}}^{\pm}_j = \begin{pmatrix} \frac{(\pm ik_{jz(-N)(-N)})^0}{0!} & \frac{(\pm ik_{jz(-N)(-N)})^1}{1!} & \cdots & \frac{(\pm ik_{jz(-N)(-N)})^{N_{tr}}}{N_{tr}!} \\ \vdots & \vdots & \vdots & \vdots \\ \frac{(\pm ik_{jzmn})^0}{0!} & \frac{(\pm ik_{jzmn})^1}{1!} & \cdots & \frac{(\pm ik_{jzmn})^{N_{tr}}}{N_{tr}!} \\ \vdots & \vdots & \vdots & \vdots \\ \frac{(\pm ik_{jzNN})^0}{0!} & \frac{(\pm ik_{jzNN})^1}{1!} & \cdots & \frac{(\pm ik_{jzNN})^{N_{tr}}}{N_{tr}!} \end{pmatrix} \tag{2.47}$$

Then the integral term of the entry $Q^{\pm}_{mnpq}$ can be obtained as the $(n-q, m-p)$-entry of the matrix product $\bar{\bar{K}}^{\pm}_j \cdot \bar{\bar{F}}$. The computation of this product involves only N_{tr} Fourier transforms and the number of Fourier transform operations will not increase with the number of Floquet modes included.

As the size of the matrix $\bar{\bar{T}}$ increases by a factor of four from the 2D problem to the 3D

30
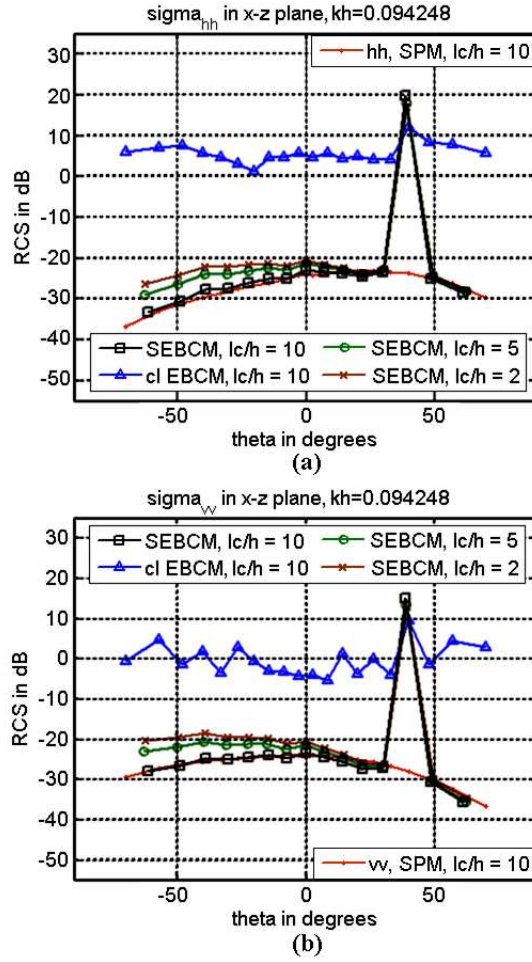
Figure 2.6: Comparison of 3D SEBCM and classical EBCM results for $\varepsilon_1 = 5.46 + 0.37i$, exponential rough surface with $k_0 h_{rms} = 0.094$, $l_c / h_{rms} = 10$ (SPM results are shown as a reference). SEBCM results of $l_c / h_{rms} = 5$ and $l_c / h_{rms} = 2$ are presented as well: (a) σ_{hh}; (b) σ_{vv}.

problem, the filling procedure of the matrix $\bar{\bar{T}}$ and $\bar{\bar{P}}$ also slows down the computation. By observing the matrix expressions (2.25) and (2.27), this procedure can be reduced to filling only six sub-matrix blocks, $[I^{\pm}_{j,mnpq}]$, $[(k_{xn} - k_{xq})I^{\pm}_{j,mnpq}]$ and $[(k_{ym} - k_{yp})I^{\pm}_{j,mnpq}]$. The remaining sub-matrix blocks can be obtained by left or right multiplication of the diagonal matrices $[k_{xn}]$, $[k_{ym}]$ and $[k_{jzmn}]$ with these six sub-matrices. This results in a similar efficiency for matrix filling as in the 2D EBCM.

The matrix $\bar{\bar{T}}$, which requires the matrix inverse operation, is of dimension $2(2N +$

$1)^2 \times 2(2N+1)^2$. Its size increases as the 4th power of the number of Floquet modes. Hence, it is usually difficult to include a large number of Floquet modes. However, when considering scattering from a single surface, the knowledge of only one column in the inverse matrix corresponding to the propagation vector of the incident wave is sufficient. Therefore, finding the matrix inverse reduces to solving a linear system. Additionally, rows in the matrix $\bar{\bar{T}}$ can be grouped and an algorithm based on row operations can be used to solve the linear system with modest memory resources. Moreover, the structure of the matrix $\bar{\bar{T}}$ involving zero sub-matrices is also utilized for speed enhancement. When full inverse of the matrix $\bar{\bar{T}}$ is required for further work involving multiple surfaces, matrix inversion based on sub-matrices can be utilized.

Using a single 2.4 GHz processor and 2 GB memory, simulating the 3D problem of scattering from a $L_x = L_y \approx 15\lambda$ rough surface including 30 Floquet modes takes 3 hours in Matlab for one realization. Having similar accuracy in the results shown in Figure 2.11 and Figure 2.12 in the next section, the number of unknowns to be solved in 3D SEBCM for an given incident field is on the order of $16N^2$, which is much less than the number of unknowns required in MoM [43].

2.3 Model Validation

2.3.1 Stabilization Results

As shown in Figure 2.6, in the case of lossy medium ($\varepsilon_1 = 5.46 + 0.37i$, usually in the case of very low soil moisture content), the classical EBCM solutions are not valid any more for surface roughness of only $k_0 h_{rms} \approx 0.1$ with $l_c/h_{rms} = 10$, indicating a validity domain no larger than the analytical solutions. Presented in the same figure, the SEBCM gives very stable results (SPM results of this case are plotted as a reference). Moreover, stable SEBCM results for even larger h_{rms}/l_c ratios are shown as well.
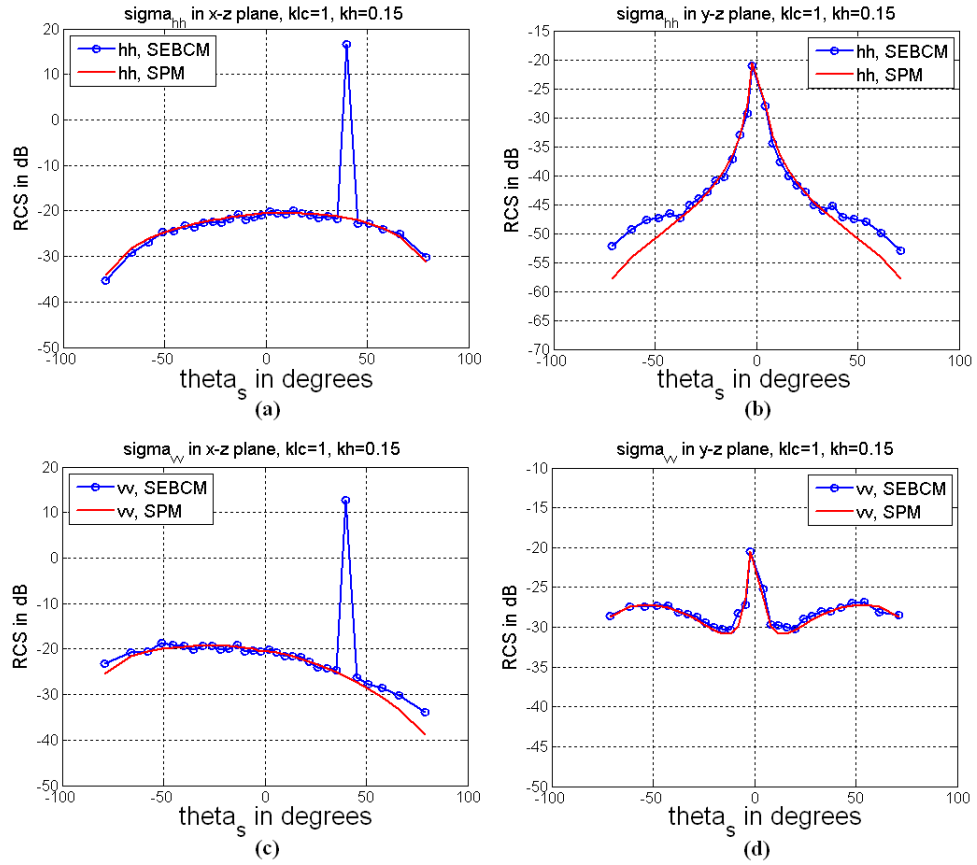
Figure 2.7: Comparison of co-pol SCSs of SEBCM and SPM ($\varepsilon_0 = 1$, $\varepsilon_1 = 5$, Gaussian rough surface with $k_0 l_c = 1$, $k_0 h = 0.15$, $\theta_i = 40°$, over 50 realizations): (a) σ_{hh} in x-z plane; (b) σ_{hh} in y-z plane; (c) σ_{vv} in x-z plane; (d) σ_{vv} in y-z plane.

2.3.2   Validation with Analytical Solutions for Surfaces with 2D Roughness

The validity of the 3D SEBCM solutions for scattering from random rough surfaces is verified first by comparison with the small perturbation method results for surfaces with slight roughnesses that are within the SPM validity domain, as shown in Figure 2.7 - Figure 2.9. The Gaussian rough surface has statistics of $k_0 l_c = 1$ and $k_0 h_{rms} = 0.15$ with periods of $L_x = L_y = 14.78\lambda_0$, $\varepsilon_0 = 1$ and $\varepsilon_1 = 5$. Results shown are computed over 50 realizations with $k_{bdry} = k_1$ and $\Delta = 0$. The co-pol scattering cross section (SCS) comparisons in the x-z and y-z planes are shown in Figure 2.7, and the cross-pol SCS comparisons in y-z plane
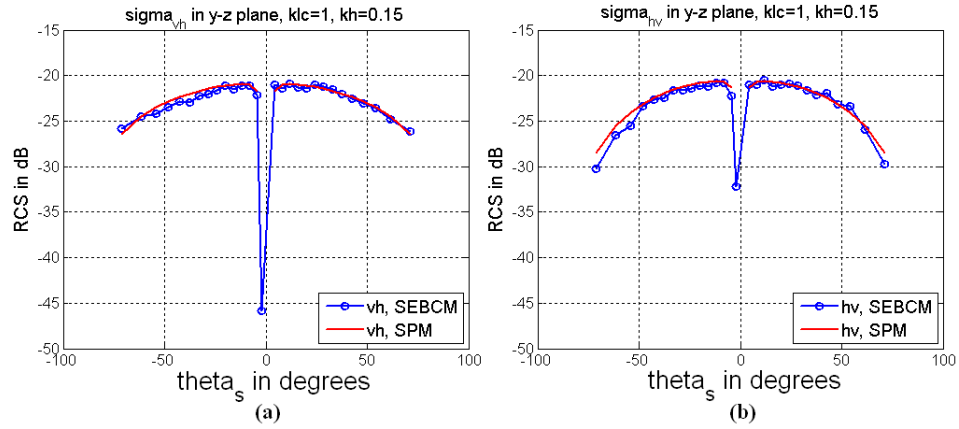
Figure 2.8: Comparison of cross-pol SCSs of SEBCM and SPM in y-z plane ($\varepsilon_0 = 1$, $\varepsilon_1 = 5$, Gaussian rough surface with $k_0 l_c = 1$, $k_0 h = 0.15$, $\theta_i = 40°$, over 50 realizations): (a) σ_{vh}; (b) σ_{hv}.
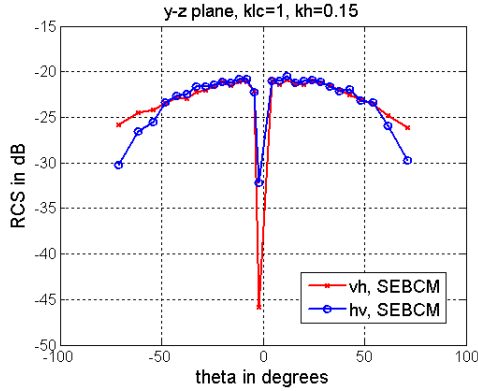
Figure 2.9: Comparison of two cross-pol SCSs of 3D SEBCM ($\varepsilon_0 = 1$, $\varepsilon_1 = 5$, Gaussian rough surface with $k_0 l_c = 1$, $k_0 h = 0.15$, $\theta_i = 40°$, over 50 realizations) in x-z plane of section.

is shown in Figure 2.8. As can be seen, the SEBCM and SPM solutions agree with each other very well. Disagreement appears at large scattering angles where SPM is not valid. Figure 2.9 verifies the reciprocity in the cross-pol components of the 3D SEBCM results. A good agreement can be seen in y-z plane. Their values in x-z plane are expected to be zero.

For larger roughnesses, the SEBCM solutions are verified with small slope approximation results for surfaces with $\varepsilon_1 = 5$, $k_0 h_{rms} = 0.5$, $k_0 l_c = 2.5$ as shown in Figure 2.10 (a) and

34
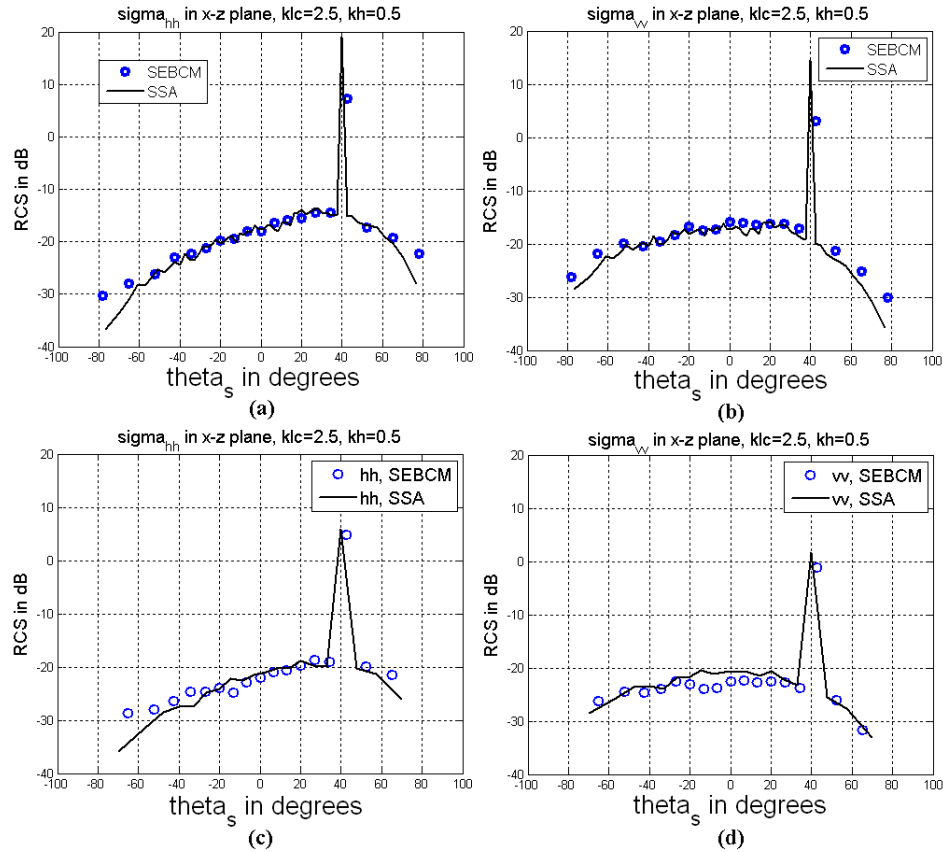
Figure 2.10: Comparison of SEBCM and SSA solutions: (a) and (b) are SCSs in x-z plane for lossless medium ($\varepsilon_1 = 5$, exponential rough surface with $k_0 h_{rms} = 0.5$, $k_0 l_c = 2.5$); (c) and (d) are SCSs in x-z plane for lossy medium ($\varepsilon_1 = 5.46 + 0.37i$, exponential rough surface with $k_0 h_{rms} = 0.5$, $k_0 l_c = 2.5$).

(b). The results are computed over 50 realizations with incidence angle of $40°$, $k_{bdry} = k_1$, $\Delta = 0$, and the limit of the number of Floquet modes N_{limit} of 20. Very good agreement can be seen. For this roughness ($h_{rms}/l_c = 1/5$), the SSA solutions tend to underestimate the scattering at angles larger than $\sim 78°$ [19]. Figure 2.10 (c) and (d) compares SEBCM and SSA solutions for a lossy medium ($\varepsilon_1 = 5.46 + 0.37i$) and same surface statistics.

2.3.3 Validation with MoM and AIEM

As shown in Figure 2.11 and Figure 2.12, SEBCM results of scattering from surfaces with both small and large roughnesses are compared to the solutions from MoM [43]. The simulations use Gaussian random rough surfaces with exponential correlation functions.

35
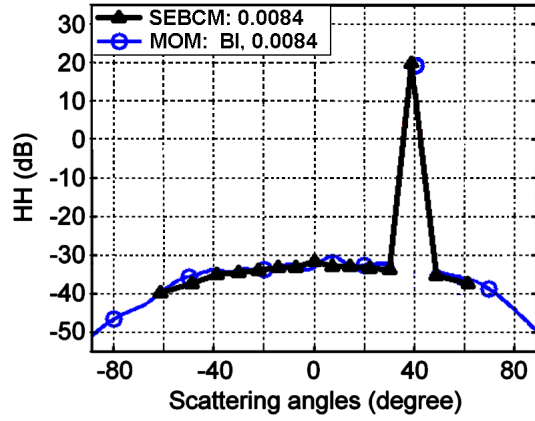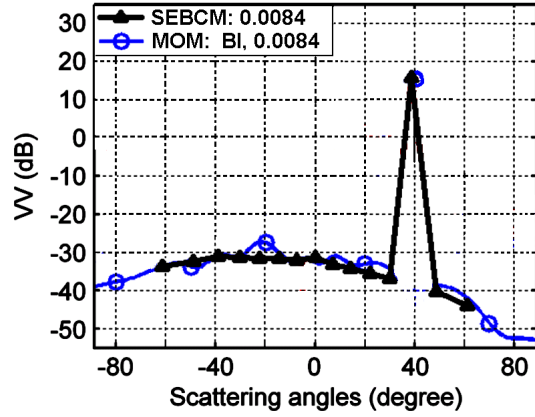
Figure 2.11: Comparison between SEBCM and MoM solutions for (a) HH with rms height of $0.0084\lambda_0$; (b) VV with rms height of $0.0084\lambda_0$. ($\varepsilon_1 = 5.46 + i0.37$, exponential rough surface with $l_c/h = 10$). Reference: [43].

Figure 2.11 compares HH and VV results for the surface with $h_{rms} = 0.0084\lambda_0$, and Figure 2.12 shows comparisons of HH and VV for the surface with $h_{rms} = 0.105\lambda_0$. Both cases are using $l_c/h_{rms} = 10$ and $\varepsilon_1 = 5.46 + i0.37$. Good agreements can be observed. Results of MoM were not available for HV.

Moreover, simulations are carried out for various other heights and the same l_c/h_{rms} ratio, as shown in Figure 2.13 for HH and Figure 2.14 for VV, where comparisons between SEBCM and several other method including MoM, AIEM, and an empirical model [43] can be seen. SEBCM gives larger backscattering coefficients for large rms heights compared to MoM. Simulations show that the SEBCM extends the range of validity of solutions as
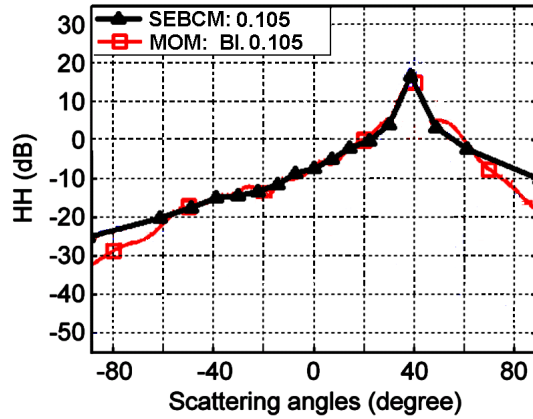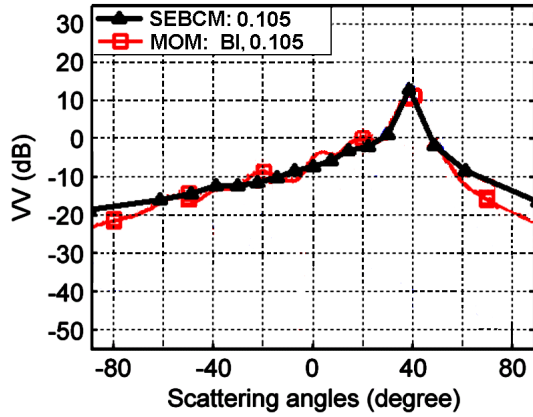
Figure 2.12: Comparison between SEBCM and MoM solutions for (a) HH with rms height of $0.105\lambda_0$; (b) VV with rms height of $0.105\lambda_0$. ($\varepsilon_1 = 5.46 + i0.37$, exponential rough surface with $l_c/h = 10$). Reference: [43].

a function of surface roughness to at least $kh_{rms} = 1$ as opposed to $k_0 h_{rms} < 0.2$ (lossless cases) for classical EBCM.

Simulation results as a function of the real part of permittivity are shown in Figure 2.15 for HH-pol and Figure 2.16 for VV-pol, where solutions from the other models [43] are also shown for comparison. These results were generated for $l_c/h_{rms} = 6$. As seen from the resutls, no two methods completely agree but the solution is stable and consistent.
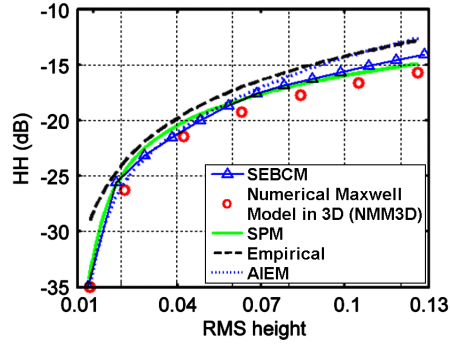
Figure 2.13: Comparison of backscattering coefficients in decibel as a function of rms height between SEBCM and other model solutions for HH ($\varepsilon_1 = 5.46 + i0.37$, exponential rough surface with $l_c/h_{rms} = 10$). Reference: [43]
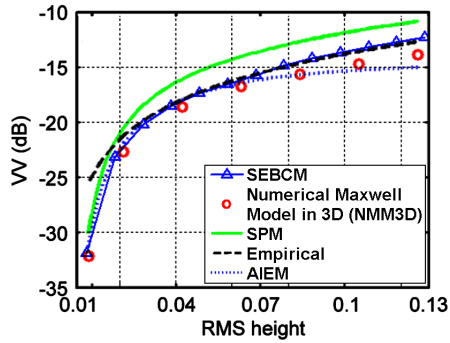
Figure 2.14: Comparison of backscattering coefficients in decibel as a function of rms height between SEBCM and other model solutions for VV ($\varepsilon_1 = 5.46 + i0.37$, exponential rough surface with $l_c/h_{rms} = 10$). Reference: [43]
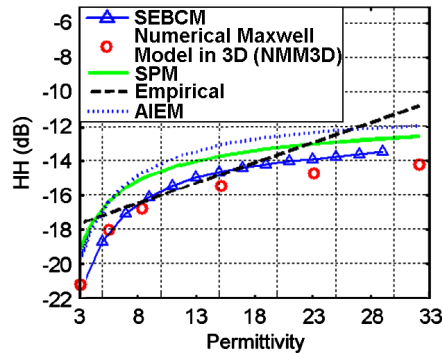
Figure 2.15: Comparison of backscattering coefficients in decibel as a function of real part of permittivity between SEBCM and other model solutions for HH ($h_{rms} = 0.063\lambda_0$, exponential rough surface with $l_c/h_{rms} = 6$). Reference: [43]

38
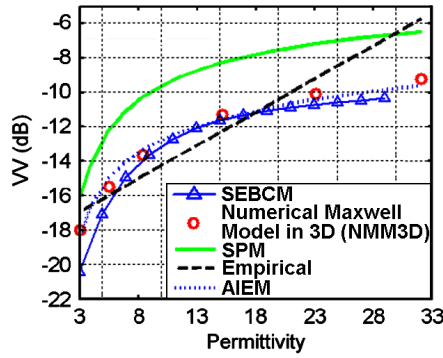
Figure 2.16: Comparison of backscattering coefficients in decibel as a function of real part of permittivity between SEBCM and other model solutions for VV ($h_{rms} = 0.063\lambda_0$, exponential rough surface with $l_c/h_{rms} = 6$). Reference: [43]
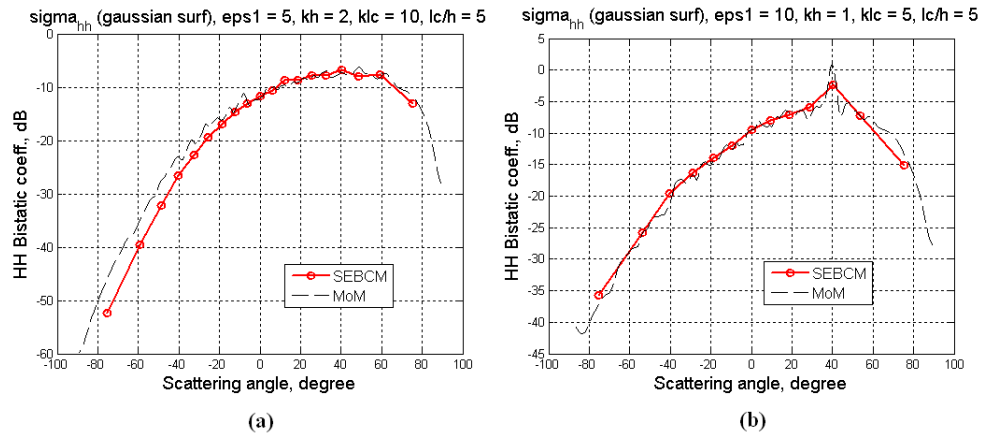
Figure 2.17: Comparison of 2D SCSs computed (over 50 realizations) using 3D SEBCM and MoM (only for hh) ($\varepsilon_0 = 1$, $\theta_i = 40°$, Gaussian rough surface): (a) σ_{hh} for surface with $\varepsilon_1 = 5$, $k_0 h_{rms} = 2$ and $k_0 l_c = 10$; (b) σ_{hh} for surface with $\varepsilon_1 = 10$, $k_0 h_{rms} = 1$ and $k_0 l_c = 5$.

2.3.4 Validation with MoM solutions for 2D surfaces with 1D roughnesses

The 3D SEBCM solutions are also compared with MoM for 2D surfaces with 1D roughness as shown in Figure 2.17, where $k_0 h_{rms} = 2$, $k_0 l_c = 10$ in (a) for $\varepsilon_1 = 5$ and $k_0 h_{rms} = 1$, $k_0 l_c = 5$ in (b) for $\varepsilon_1 = 10$. Good agreements can be seen in these comparisons. In these cases, the 3D SEBCM degenerates into 2D SEBCM and shows significant improvement in its validity range as a function of surface roughnesses compared to classical EBCM.
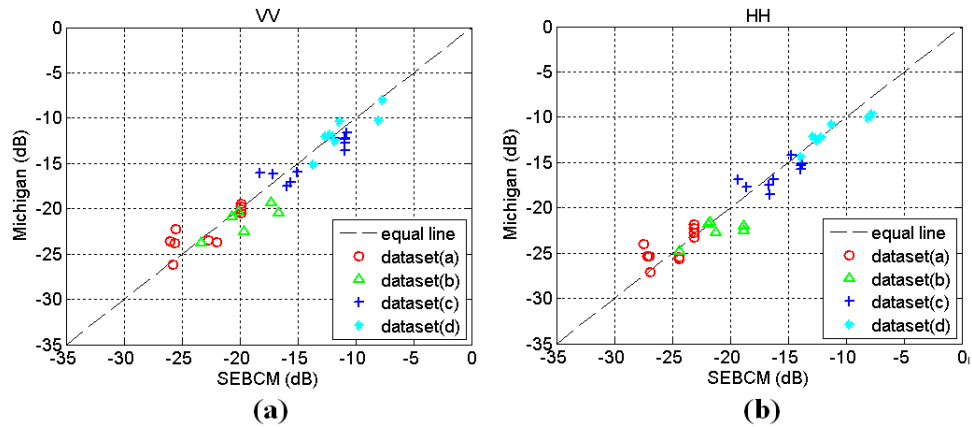
Figure 2.18: Comparison of VV- and HH-pol. backscattering coefficients between SEBCM and Michigan measurement data (as in Table 2.1).

Detailed analysis of the 2D cases is included in [44].

2.3.5 Comparison with Measurement Data

Michigan's L-band POLARSCAT data [11] and its comparison with other model results [43] are further used to verify the SEBCM solutions. The incidence angle is $40°$ and the surface and medium properties are listed in Table 2.1. Figure 2.18 shows the comparisons of SEBCM with the observation data. Good agreement can be seen between SEBCM results and the measurement data. The mean absolute error in VV-pol. is 1.30 dB, and the mean absolute error in HH-pol is 1.20 dB.

2.4 Summary and Conclusion

The stabilized extended boundary condition method (SEBCM) for solving the three-dimensional bistatic scattering from arbitrary random rough surfaces is developed based on the classical EBCM. This method retrieves the surface sources by matching the extended boundary conditions of the Floquet-mode expanded fields at the test surfaces away from the actual rough surface, then stabilizes the solutions by explicitly restricting and controlling the test surface locations. The numerical computation is further stabilized by

40

Table 2.1: Comparison between Theoretical Results and Michigan Observation Data. (in dB) [43]

Table 2.1: (a) RMS height = 0.55 cm, correlation length = 9.40 cm.

Real	Imag	Michigan Data	SEBCM	NMM3D
3.61	0.24	VV -23.56, HH -25.39	VV -26.01, HH -27.10	VV -25.47, HH -28.50
3.73	0.26	VV -26.14, HH -27.08	VV -25.78, HH -26.91	VV -25.31, HH -28.34
3.76	0.26	VV -23.76, HH -25.39	VV -25.61, HH -26.94	VV -25.27, HH -28.30
4.31	0.32	VV -22.30, HH -24.00	VV -25.49, HH -27.45	VV -24.60, HH -27.66
5.40	0.44	VV -23.51, HH -25.49	VV -22.67, HH -24.41	VV -23.46, HH -26.66
6.42	0.55	VV -23.74, HH -25.63	VV -21.95, HH -24.43	VV -22.60, HH -26.01
12.39	1.10	VV -19.80, HH -22.21	VV -19.90, HH -23.14	VV -19.91, HH -24.14
12.39	1.10	VV -19.46, HH -21.85	VV -19.90, HH -23.14	VV -19.91, HH -24.14
12.39	1.10	VV -20.45, HH -23.25	VV -19.90, HH -23.14	VV -19.91, HH -24.14
12.39	1.10	VV -20.07, HH -22.81	VV -19.90, HH -23.14	VV -19.91, HH -24.14

Table 2.1: (b) RMS height = 0.94 cm, correlation length = 6.90 cm.

Real	Imag	Michigan Data	SEBCM	NMM3D
2.89	0.15	VV -23.84, HH -24.87	VV -23.32, HH -24.37	VV -21.01, HH -24.32
3.61	0.24	VV -20.94, HH -21.68	VV -20.70, HH -21.74	VV -20.12, HH -23.08
4.18	0.31	VV -22.54, HH -22.81	VV -19.60, HH -21.22	VV -19.47, HH -22.29
4.31	0.32	VV -20.35, HH -21.80	VV -20.08, HH -21.86	VV -19.34, HH -22.14
5.40	0.44	VV -19.34, HH -22.06	VV -17.34, HH -18.84	VV -18.30, HH -21.10
6.42	0.55	VV -20.49, HH -22.58	VV -16.62, HH -18.80	VV -17.49, HH -20.50

Table 2.1: (c) RMS height = 1.78 cm, correlation length = 8.30 cm.

Real	Imag	Michigan Data	SEBCM	NMM3D
2.94	0.16	VV -16.07, HH -16.92	VV -18.29, HH -19.33	VV -16.97, HH -20.22
3.32	0.20	VV -16.18, HH -17.73	VV -17.14, HH -18.58	VV -16.50, HH -19.50
3.64	0.24	VV -17.55, HH -17.52	VV -15.96, HH -16.67	VV -16.13, HH -18.95
3.82	0.27	VV -17.08, HH -18.57	VV -15.60, HH -16.58	VV -15.93, HH -18.67
4.15	0.30	VV -15.94, HH -16.93	VV -15.08, HH -16.22	VV -15.59, HH -18.20
11.27	1.00	VV -12.22, HH -14.20	VV -11.83, HH -14.73	VV -11.59, HH -14.82
13.68	1.21	VV -12.38, HH -15.29	VV -10.90, HH -13.95	VV -10.94, HH -14.35
13.68	1.21	VV -12.26, HH -15.12	VV -10.90, HH -13.95	VV -10.94, HH -14.35
13.68	1.21	VV -12.72, HH -15.09	VV -10.90, HH -13.95	VV -10.94, HH -14.35
13.68	1.21	VV -13.57, HH -15.77	VV -10.90, HH -13.95	VV -10.94, HH -14.35
14.19	1.26	VV -11.65, HH -15.13	VV -10.80, HH -13.77	VV -10.82, HH -14.27

Table 2.1: (d) RMS height = 3.47 cm, correlation length = 11.00 cm.

Real	Imag	Michigan Data	SEBCM	NMM3D
2.94	0.16	VV -15.14, HH -14.44	VV -13.68, HH -13.95	VV -15.93, HH -15.05
3.34	0.21	VV -12.51, HH -12.10	VV -11.85, HH -12.85	VV -14.59, HH -14.39
3.64	0.24	VV -11.98, HH -12.51	VV -12.66, HH -12.51	VV -13.70, HH -13.94
4.15	0.30	VV -11.85, HH -12.25	VV -12.25, HH -12.10	VV -12.43, HH -13.28
4.63	0.36	VV -10.35, HH -10.80	VV -11.42, HH -11.28	VV -11.46, HH -12.75
11.27	1.00	VV -10.29, HH -10.02	VV -8.01, HH -8.13	VV -8.30, HH -9.47
14.19	1.26	VV -7.98, HH -9.65	VV -7.71, HH -7.80	VV -7.85, HH -8.40

balancing the Floquet mode distribution in k-space and introducing a k-boundary to eliminate the evanescent modes and attenuated modes that are unnecessarily involved in the calculation. Meanwhile, by introducing a tolerance in the computation, this method can be applied with moderate computing power as well. Additional to the development of 3D SEBCM, for numerical implementation, a model for two-dimensional rough surfaces with arbitrary statistical properties is developed, and the relationship between bistatic scattering cross section and upward-propagating Floquet modes is extended into three-dimensions.

The simulation results of SEBCM are compared with the SPM solutions for slightly rough surfaces. Results are also verified with the SSA solutions for lossy surfaces and surfaces with larger roughnesses outside the validity regimes of SPM. These comparisons validate the 3D SEBCM solutions within the validity domains of above analytical approaches respectively. Moreover, further validation of the 3D SEBCM is done using the 3D MoM results for 2D surfaces with 2D and 1D roughness, as well as with field observations.

Compared to the classical EBCM, the 3D SEBCM improves the surface roughness validity region for $k_0 h_{rms}$ from less than 0.2 (with lossless medium) to at least 1. This range of roughnesses makes SEBCM an appropriate method for realistic soil moisture applications. Much more significant improvement can be seen when the method is applied to 2D surfaces with 1D roughness, where its validity range up to $k_0 h_{rms} = 2$.

CHAPTER 3

Three-dimensional Bistatic Electromagnetic Scattering from Multi-Layer Surfaces with Arbitrary Roughness

A model of three-dimensional electromagnetic scattering from multiple rough surfaces within homogeneous-layered or vertically inhomogeneous media is developed in this chapter. This model, aimed at radar remote sensing of surface-to-depth profiles of soil moisture, computes total bistatic radar cross sections from the multilayer structure based on the scattering matrix approach, cascading the scattering matrices of individual rough interfaces and the layer propagation matrices. We have developed the single-surface scattering matrix obtained using the stabilized extended boundary condition method (SEBCM) providing both large validity range over the surface roughness and higher computational efficiency compared to fully numerical solutions in the previous chapter. In the presence of a vertical dielectric profile, the aggregate scattering matrix of the profile is obtained from the model of stratified homogeneous layers. Results of this multilayer SEBCM model are validated with small perturbation method (SPM) of up to third order and the method of moments (MoM). Additionally, the model is used to perform a sensitivity analysis of the scattering cross section with respect to perturbations in ground parameters such as subsurface layer separation, roughness of surface and subsurface layers, and moisture content of subsurface layers. The multilayer SEBCM model developed here presents a realistic and computationally feasible method for solving scattering from multilayer rough surfaces of realistic

43

roughness, providing an accurate and efficient tool for future retrievals of soil moisture profiles.

3.1   Introduction

Multilayer media with random rough interfaces represent many natural structures such as soil profiles, snow-covered ground, and multilayer ice. Remote sensing of these structures is of increasing importance in scientific and operational applications. Soil moisture profiles, in particular, are of special interest for their prominent role in both climatic and hydrologic modeling. Monitoring subsurface and root-zone soil moisture on a global scale will provide better understanding of the global hydrologic cycle, and could result in better short-term weather and long-term climate predictions. Despite its importance, subsurface and root-zone soil moisture is still one of the least observed geophysical quantities. Active and passive microwave remote sensing at L-band ($\sim$1.26 GHz - 1.4 GHz) and higher frequencies has long been recognized as the most suitable way for large-scale observations of surface soil moisture [9], evidenced by the development of missions such as the NASA Soil Moisture Active and passive (SMAP) mission and the European Space Agency (ESA) Soil Moisture and Ocean Salinity (SMOS) mission. The SMAP mission [9], in particular, will map the global soil moisture with a synthetic aperture radar (SAR) and a radiometer operating at L-band with ground resolutions of 1-3 km and 36 km, respectively. It will allow retrieval of soil moisture for bare to moderately vegetated surfaces.

To remotely sense the subsurface and root-zone soil moisture, lower-frequency measurement systems are needed for their capability of deeper penetration. The NASA Earth Ventures 1 (EV-1) Airborne Microwave Observatory of Subcanopy and Subsurface (Ari-MOSS) mission, currently under development, is such a system and will be equipped with an airborne P-band synthetic aperture radar (SAR) for observations of subsurface and root-zone soil moisture with multi-looked resolution of a few tens of meters over several representative biomes in north America. To retrieve subsurface soil properties, radar scattering

44

models of layered media representing soil profiles are needed, which must also include random rough boundaries. Typically, these forward scattering models are the most time- and resource-consuming component of retrieval algorithms, highlighting the need for an accurate and efficient forward model of electromagnetic (EM) scattering from multilayer rough surfaces.

In the past, several works have been dedicated to solving the multilayer rough surface scattering problem. In [45], the problem has been solved for the two-dimensional (2D) case - or the 1D rough surface - using the classical extended boundary condition method (EBCM). For the same problem in 3D, [17] gives the solution using small perturbation method (SPM) for interfaces having small roughnesses ($k_0 l_c \sim 1$, $k_0 h < 0.3$, where k_0 is the free space wave number, h and l_c are the rms height and correlation length of the surface [46]). SPM solutions up to 4th order are discussed in [47]. For a fully numerical solution for the two-rough-surface problem, the steepest descent fast multipole method (SDFMM) has been presented in [48], though the surface is assumed to be deterministic in that a single specific surface realization has been considered. Other numerical approaches based on the method of moments (MoM) have also been developed and are currently under evaluation [27]. The fully numerical methods require extremely large computational resources and cannot easily be extended to cases involving more than two surfaces. An alternative is offered in this work for the electromagnetic scattering from multilayer random rough surfaces, using the scattering matrix approach and the stabilized extended boundary condition method (SEBCM). This model, which we call the multilayer SEBCM, provides both validity over large surface roughnesses and high computational efficiency. It is also not limited to two surfaces, and can be readily extended to multiple (>2) layers.

The multilayer SEBCM computes the scattering cross section from the multiple-layered media with rough interfaces by cascading the scattering matrices of all interfaces and the propagation matrices of all intervening layers, which together can represent arbitrary profiles and any number of rough interfaces. Single-surface scattering matrix of each random rough interface is found using the stabilized extended boundary condition method (SE-

BCM) we developed and discussed in the last chapter. With much higher computational efficiency than the numerical methods, it gives accurate full wave solutions to the vector scattered fields over all directions from a single surface with large roughness range ($k_0 h < 1.0$). Besides the EM scattering occurring at each medium interface, wave propagation within every profile layer is described by the propagation matrix. In this work, two types of profile layers are considered: (1) homogeneous and (2) inhomogeneous consisting of a vertical dielectric profile. The latter is modeled as stacked homogeneous differential layers with small layer thickness compared to the wavelength. The reflection and transmission matrices of this arrangement are calculated by recursively cascading those of the differential layers.

Validation of the multilayer SEBCM model is performed by comparisons with other available solutions. First, results are compared with small perturbation method solutions for multilayer surfaces of small roughnesses using the 1st order (SPM1) and large roughnesses using the 3rd order (SPM3) solutions. Moreover, the incoherent components of the solutions are compared with the method of moments (MoM) results for the two-rough-surface case with good agreements.

Once validated, we use the multilayer SEBCM to carry out a sensitivity study of the bistatic radar scattering cross section to variations in the ground parameters of interest in soil moisture detection, such as the depth of the subsurface layer, subsurface layer roughness, and subsurface layer moisture content, for both L-band and P-band frequencies. As shown from the results, while P-band scattering cross section shows up to $\sim$10 dB variation in the backscattering direction as a function of the subsurface and sublayer properties investigated, L-band scattering cross section is much less sensitive to these parameters.

(a)

(b)
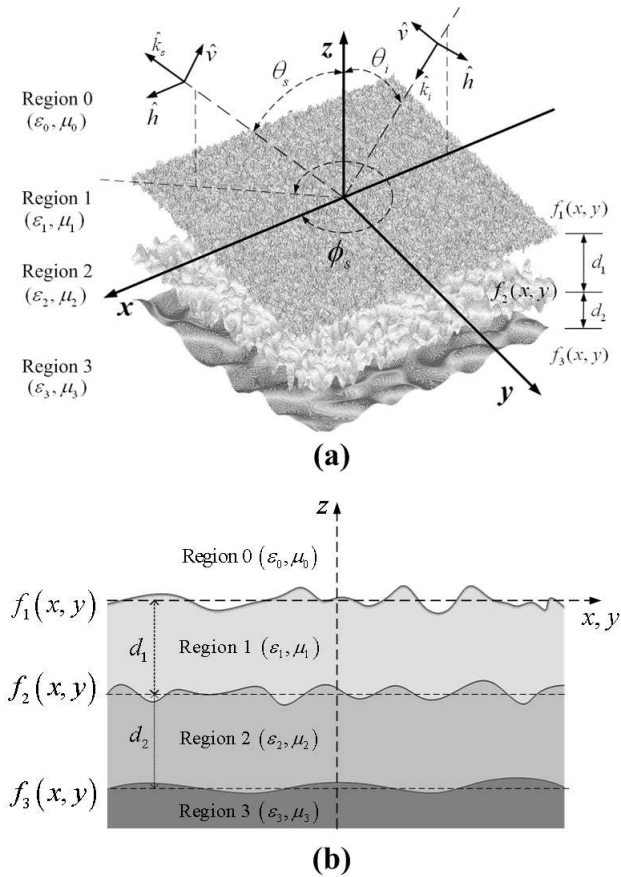
Figure 3.1: Geometry of 3D scattering from multiple rough surfaces (a) and its cross-section (b)

3.2 Problem Geometry and Formulation

3.2.1 Problem Geometry

Geometry of the 3D scattering from multilayer rough surfaces is illustrated in Figure 3.1, where j surfaces $f_1, f_2, \ldots, f_j$ divide the space into $j + 1$ regions. The upper region (region 0) is free space with $\varepsilon_0 = 1$ and $\mu_0 = 1$. The lower j regions are layers with homogeneous or depth-varying dielectric properties described by $\varepsilon_j(z)$, $\mu_j(z)$. Thickness of the jth layer is denoted by d_j. To apply EBCM, we assume periodic boundary conditions for

47

the rough surfaces, such that each surface profile satisfies

$$f_j(x,y) = f_j(x+nL_x, y+mL_y), \quad \forall\, m,n \in \mathbb{Z}$$

where L_x and L_y are periods along x- and y-directions respectively.

The incidence plane is coincident with the x-z plane and the projection of the incident wave vector points towards the positive x-direction. Polarization of the incident field is defined to be horizontal (H) or TE polarized when the electric field is parallel with the x-y plane and vertical (V) or TM polarized when the magnetic field is parallel to the x-y plane.

3.2.2 Single-Surface Scattering Matrix

Scattering matrix of a single rough surface is obtained using the stabilized extended boundary condition method (SEBCM) we presented in Chapter 2. Here we summarize its formulation of scattering matrix as

$$\bar{\bar{S}} = \begin{bmatrix} D_b^{(0)} & 0 & 0 & 0 & 0 & 0 \\ 0 & D_b^{(0)} & 0 & 0 & 0 & 0 \\ 0 & 0 & D_b^{(0)} & 0 & 0 & 0 \\ 0 & 0 & 0 & D_a^{(1)} & 0 & 0 \\ 0 & 0 & 0 & 0 & D_a^{(1)} & 0 \\ 0 & 0 & 0 & 0 & 0 & D_a^{(1)} \end{bmatrix} \cdot \bar{\bar{P}} \cdot \bar{\bar{T}}^{-1} \cdot \begin{bmatrix} D_a^{(0)} & 0 & 0 & 0 \\ 0 & D_a^{(0)} & 0 & 0 \\ 0 & 0 & D_b^{(1)} & 0 \\ 0 & 0 & 0 & D_b^{(1)} \end{bmatrix}^{-1}$$

(3.1)

where the matrix $\bar{\bar{T}}$ relates the surface electric and magnetic currents to the incoming wave, while the matrix $\bar{\bar{P}}$ relates the outgoing wave, i.e., the scattered fields, with the surface currents. They are expressed as in Eq.(2.25) and Eq.(2.27). The matrix entries in each sub-matrix block are shown in Eq.(2.28) and Eq.(2.29).

Diagonal matrices in Eq.(3.1) are from the z-coordinate transformation in SEBCM, which ensures that the extended boundaries are away from the actual rough surface, and therefore stabilizes the solution.

3.2.3 Reflection and Transmission Matrices of Homogeneous and Vertical Dielectric Profiles

Through a homogeneous layer, wave propagation can be described by the matrix,

$$\bar{\bar{\Phi}}_{dj}^+ = \begin{bmatrix} \phi_{dj}^+ & 0 & \cdots & 0 \\ 0 & \phi_{dj}^+ & \cdots & 0 \\ \vdots & \vdots & \ddots & \vdots \\ 0 & 0 & \cdots & \phi_{dj}^+ \end{bmatrix} \tag{3.2}$$

where $\phi_{dj}^+ = e^{+ik_{jzmn}\Delta d}$ and Δd is the layer thickness. In the case of a layer with rough interfaces at the top and the bottom, $\Delta d = d_j - |f_{max,j}| - |f_{min,j-1}|$, where d_j is the separation between the interface mean-planes, $f_{max,j}$ is the deviation of the highest point on the bottom interface and $|f_{min,j-1}|$ is the deviation of the lowest point of the upper interface.

For an inhomogeneous medium with a dielectric profile along depth, the profile can be stratified and discretized into a stack of homogeneous differential layers as in [26]. With the differential layer thicknesses being sufficiently small compared with the wavelength (e.g., $\lambda/10$) and the profile gradient, the original inhomogeneous layer can be modeled accurately. By knowing the reflection and transmission matrices obeying Fresnel's law at each planar interface between the differential layers, we can write:

$$R_{j,j+1}^{TE} = \frac{k_{z,j} - k_{z,j+1}}{k_{z,j} + k_{z,j+1}} \tag{3.3}$$

$$T_{j,j+1}^{TE} = \frac{2k_{z,j}}{k_{z,j} + k_{z,j+1}} \tag{3.4}$$

$$R_{j,j+1}^{TM} = \frac{\varepsilon_{j+1}k_{z,j} - \varepsilon_j k_{z,j+1}}{\varepsilon_{j+1}k_{z,j} + \varepsilon_j k_{z,j+1}} \tag{3.5}$$

$$T_{j,j+1}^{TM} = \frac{2\varepsilon_{j+1}k_{z,j}}{\varepsilon_{j+1}k_{z,j} + \varepsilon_j k_{z,j+1}} \tag{3.6}$$

As discussed in [26], the total reflection and transmission matrices of the stratified layers
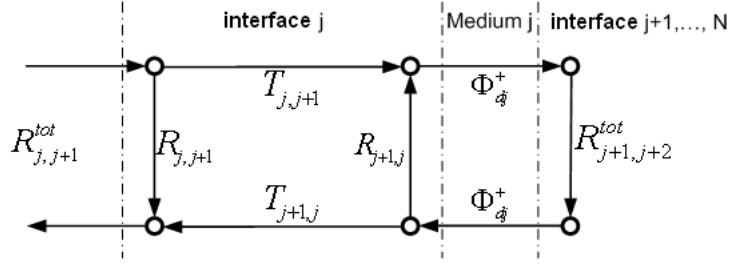
Figure 3.2: Cascading of reflection and transmission matrices of the jth interface with that of the $(j+1)$ to Nth interfaces underneath through the propagation matrix of the jth medium.

can be obtained by recursively cascading the single-interface reflection and transmission matrices from bottom to top with the propagation matrix in each layer, as illustrated in Fig.3.2, where the scenario of cascading the jth interface with the $(j+1)$th to Nth interfaces is shown. In this figure, every arrow indicates a direction of wave propagation. $R_{j,j+1}$ and $R_{j+1,j}$ are reflection coefficients when wave propagating from the $(j+1)$th medium to the jth medium and vice versa respectively. $T_{j,j+1}$ and $T_{j+1,j}$ are the transmission coefficients of the jth interface in both directions. The total reflection coefficient $R^{tot}_{j,j+1}$ can be found by summation of two propagation paths $R_{j,j+1}$ and $T_{j+1,j}\Phi^+_{d_j}R^{tot}_{j+1,j+2}\Phi^+_{d_j}T_{j,j+1}$; the latter path needs to be divided by the loop $R_{j+1,j}\Phi^+_{d_j}R^{tot}_{j+1,j+2}\Phi^+_{d_j}$ that describes the interaction between the jth interface and the rest interfaces below it. Similarly, the total transmission coefficient $T^{tot}_{j,j+1}$ can be found from the path $T_{j,j+1}\Phi^+_{d_j}T^{tot}_{j+1,j+2}$ being divided by the interaction loop. With $\bar{\bar{R}}_{j,j+1} = \text{diag}\{R_{j,j+1}\}$ and $\bar{\bar{T}}_{j,j+1} = \text{diag}\{T_{j,j+1}\}$ for all propagation modes, we can write,

$$\bar{\bar{R}}^{tot}_{j,j+1} = \bar{\bar{R}}_{j,j+1} + \frac{\bar{\bar{T}}_{j,j+1}\bar{\bar{\Phi}}^+_{dj}\bar{\bar{R}}^{tot}_{j+1,j+2}\bar{\bar{\Phi}}^+_{dj}\bar{\bar{T}}_{j+1,j}}{\bar{\bar{I}} - \bar{\bar{R}}_{j+1,j}\bar{\bar{\Phi}}^+_{dj}\bar{\bar{R}}^{tot}_{j+1,j+2}\bar{\bar{\Phi}}^+_{dj}} \tag{3.7}$$

$$\bar{\bar{T}}^{tot}_{j,j+1} = \frac{\bar{\bar{T}}_{j,j+1}\bar{\bar{\Phi}}^+_{dj}\bar{\bar{T}}^{tot}_{j+1,j+2}}{\bar{\bar{I}} - \bar{\bar{R}}_{j+1,j}\bar{\bar{\Phi}}^+_{dj}\bar{\bar{R}}^{tot}_{j+1,j+2}\bar{\bar{\Phi}}^+_{dj}} \tag{3.8}$$

where $\bar{\bar{R}}^{tot}_{j,j+1}$ and $\bar{\bar{T}}^{tot}_{j,j+1}$ are the total reflection and transmission matrices for layers below the jth layer.

50

Figure 3.3: Cascading of scattering matrix of the jth rough surface with that of the $(j+1)$ to Nth surfaces underneath through the propagation matrix of the jth medium region. The total scattering matrix of the entire layered structure can be found by recursively repeating this cascading.

3.2.4 Scattering Matrix Approach

Knowing single-surface scattering matrix of every rough interface and the propagation matrix in each layer of the medium, the aggregate scattering matrix of the multilayer structure is obtained using the scattering matrix approach illustrated in Figure 3.3.

Similar to the computation of the reflection and transmission matrices of the stratified layers, we recursively cascade the scattering matrices of all rough surfaces from bottom to top through medium propagation matrices. Hence, the aggregate scattering matrix is,

$$\bar{\bar{S}}_{11,j}^{tot} = \bar{\bar{S}}_{11,j} + \frac{\bar{\bar{S}}_{21,j}\bar{\bar{\Phi}}_{dj}^{+}\bar{\bar{S}}_{11,j+1}^{tot}\bar{\bar{\Phi}}_{dj}^{+}\bar{\bar{S}}_{12,j}}{\bar{\bar{I}} - \bar{\bar{S}}_{22,j}\bar{\bar{\Phi}}_{dj}^{+}\bar{\bar{S}}_{11,j+1}^{tot}\bar{\bar{\Phi}}_{dj}^{+}} \tag{3.9}$$

$$\bar{\bar{S}}_{21,j}^{tot} = \frac{\bar{\bar{S}}_{21,j}\bar{\bar{\Phi}}_{dj}^{+}\bar{\bar{S}}_{21,j+1}^{tot}}{\bar{\bar{I}} - \bar{\bar{S}}_{22,j}\bar{\bar{\Phi}}_{dj}^{+}\bar{\bar{S}}_{11,j+1}^{tot}\bar{\bar{\Phi}}_{dj}^{+}} \tag{3.10}$$

$\bar{\bar{S}}_{22,j}^{tot}$ and $\bar{\bar{S}}_{12,j}^{tot}$ can be computed similarly by cascading recursively from top to bottom.

3.2.5 Computation of Scattering Cross Section

From the aggregate scattering matrix of the multilayer rough surface structure, Floquet mode coefficients of the scattered fields corresponding to any given incident wave can be found, from which the bistatic scattering cross section can be calculated from the following

51

relations derived in chapter 2:

$$\sigma_{hh}(\theta_s, \phi_s) = \frac{L_x L_y k_0^2}{4\pi^2 \cos\theta_i} \cos^2\theta_s |b_{mn\phi}^{(h)}|^2 \tag{3.11}$$

$$\sigma_{vh}(\theta_s, \phi_s) = \frac{L_x L_y k_0^2}{4\pi^2 \cos\theta_i} \cos^2\theta_s |b_{mn\theta}^{(h)}|^2 \tag{3.12}$$

$$\sigma_{hv}(\theta_s, \phi_s) = \frac{L_x L_y k_0^2}{4\pi^2 \cos\theta_i} \cos^2\theta_s |b_{mn\phi}^{(v)}|^2 \tag{3.13}$$

$$\sigma_{vv}(\theta_s, \phi_s) = \frac{L_x L_y k_0^2}{4\pi^2 \cos\theta_i} \cos^2\theta_s |b_{mn\theta}^{(v)}|^2 \tag{3.14}$$

with

$$b_{mn\phi}^{(h)} = -\frac{b_{mnx}}{k_{0mnz}^2}\sin\phi_s + \frac{b_{mny}}{k_{0mnz}^2}\cos\phi_s \tag{3.15}$$

$$b_{mn\theta}^{(h)} = \frac{b_{mnx}}{k_{0mnz}^2}\cos\theta_s\cos\phi_s + \frac{b_{mny}}{k_{0mnz}^2}\cos\theta_s\sin\phi_s - \frac{b_{mnz}}{k_{0mnz}^2}\sin\theta_s \tag{3.16}$$

$$b_{mn\phi}^{(v)} = \frac{b_{mnx}}{k_{0mnz}^2}\cos\theta_s\cos\phi_s + \frac{b_{mny}}{k_{0mnz}^2}\cos\theta_s\sin\phi_s - \frac{b_{mnz}}{k_{0mnz}^2}\sin\theta_s \tag{3.17}$$

$$b_{mn\theta}^{(v)} = -\frac{b_{mnx}}{k_{0mnz}^2}\sin\phi_s + \frac{b_{mny}}{k_{0mnz}^2}\cos\phi_s \tag{3.18}$$

where (ϕ_s, θ_s) defines the observation direction.

3.3   Model Validation

To validate the multilayer SEBCM solutions, comparisons with both approximate analytical solutions and accurate full-wave numerical methods are performed. Numerical simulations of multilayer rough surfaces of small roughnesses are performed first, whose 1st-order small perturbation method (SPM1) solutions are available.

Two cases are shown here for comparisons with SPM1. The first one includes two rough

Table 3.1: SIMULATION PARAMETERS FOR TWO-ROUGH-SURFACE CASE FOR VALIDATION WITH SPM1.

kh_1	kl_{c1}	kh_2	kl_{c2}	ε_1	ε_2	d	Surf. Type
0.15	1.5	0.05	1.5	4	7	$\lambda_0/5$	Gauss. corr.
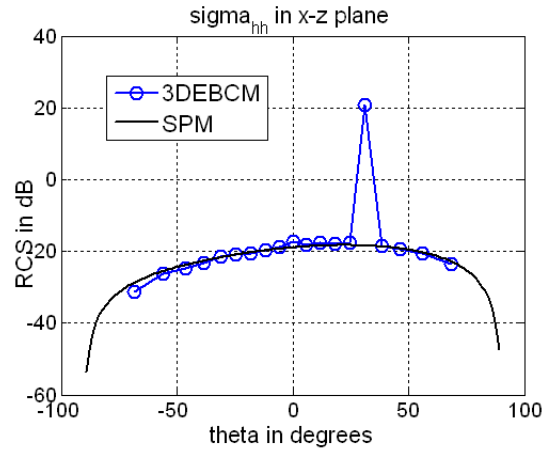
(a)
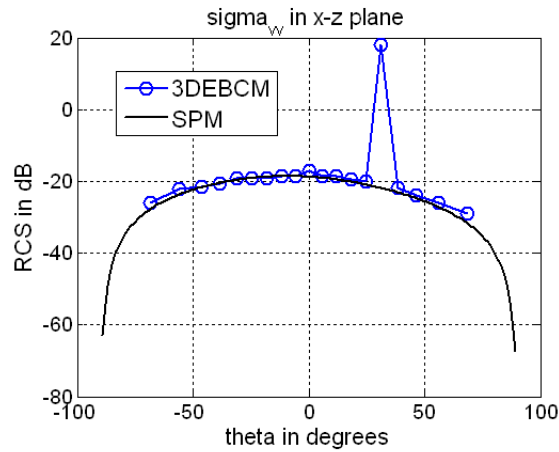
(b)

Figure 3.4: Comparison of co-pol scattering cross sections between SEBCM and SPM1 for two-rough-surfaces with parameters in Table 3.1.

surfaces bounding homogeneous lossless media. Statistics of each interface as well as the dielectric properties in every medium layer are listed in Table 3.1. Surface separation for this case is $d = \lambda_0/5$. The co-polarized scattering cross section results in Figure 3.4 show very good agreement between SEBCM and SPM1 solutions.

The second case of small roughnesses has three rough interfaces and lossy media in

Table 3.2: Simulation Parameters for Three-Rough-Surface Case for Validation with SPM1.

kh_1	kl_{c1}	kh_2	kl_{c2}	kh_3	kl_{c3}	Surf. Type
0.15	1.0	0.1	1.0	0.05	1.0	Gauss. corr.

ε_1	ε_2	ε_3	d
$5.4 + i0.44$	$11.27 + i1.0$	$4.31 + i0.32$	$\lambda_0/5$
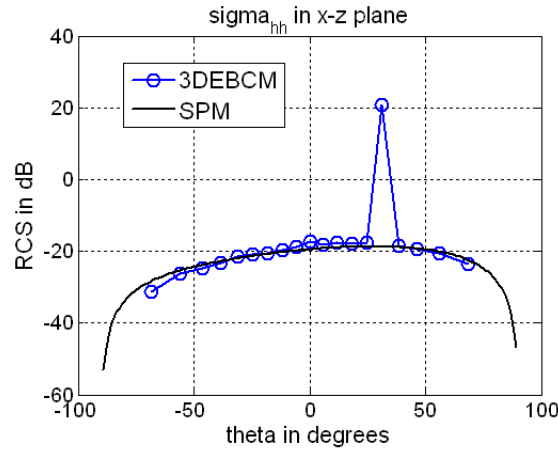
(a)
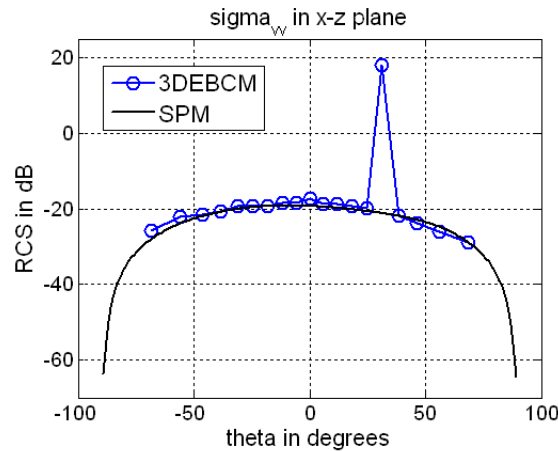
(b)

Figure 3.5: Comparison of co-pol scattering cross sections between SEBCM and SPM1 for three-rough-surfaces with parameters in Table 3.2.

between. As shown from the values listed in Table 3.2, the middle two layers are assumed to have higher permittivities than the bottom layer, which is a typical soil moisture distribution after rain events. Roughnesses of the surface and subsurfaces decrease downwards, and

the surface separations are both $\lambda_0/5$. Very good agreement between SEBCM and SPM1 results can be seen in Figure 3.5.

Table 3.3: SIMULATION PARAMETERS FOR TWO-ROUGH-SURFACE CASE FOR VALIDATION WITH SPM AND MOM.

kh_1	kl_{c1}	kh_2	kl_{c2}	ε_1	ε_2	d	Surf. Type
$\pi/5$	2π	$\pi/10$	π	5.4+0.44i	11.27+i	$\lambda_0/5$	Gauss. corr.
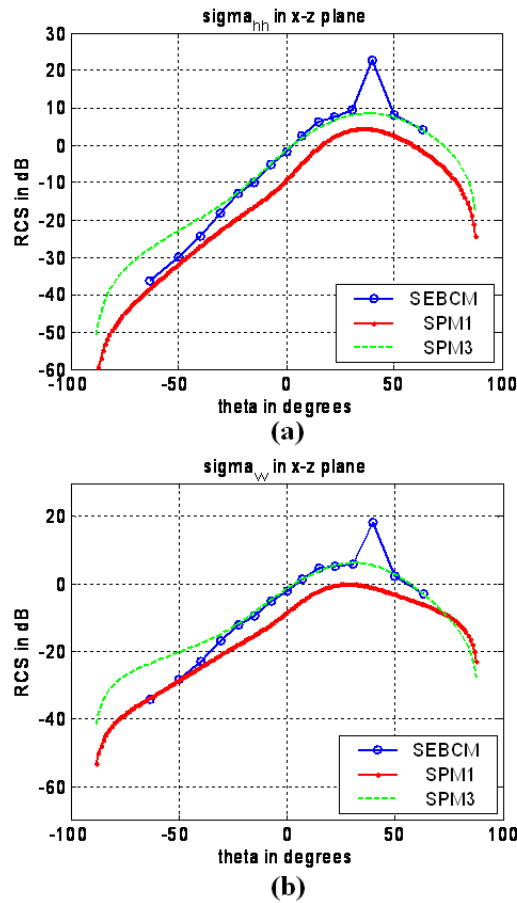
Figure 3.6: Comparison of co-pol scattering cross sections between SEBCM and SPM3 for two-rough-surfaces with parameters in Table 3.3.

For larger roughnesses, we compared two-rough-surface results with SPM3 (1st to 3rd order small perturbation method) and method of moments (MoM) solutions recently available to us [27]. Table 3.3 lists the simulation parameters. Figure 3.6 shows the comparisons

among SEBCM, SPM1, and SPM3. As can be seen, SPM1 is not valid any more for this case of large roughness. SEBCM and SPM3 agree for the most part except at large angles in the backward directions. It is unclear whether the discrepancies are due to inaccuracies of SEBCM, SPM3, or both.

With increased surface separation, $d = 0.8\lambda_0$, Figure 3.7 compares the incoherent components of the scattered fields obtained from SEBCM, SPM, and MoM. In the backward directions with large angles, SEBCM agrees well with SPM1; MoM and SPM3 predict higher values in these directions. In the backscattering direction (monostatic case) as well as the entire forward scattering directions, the agreement between SEBCM and MoM is very good.

The case of a smoother surface is also compared for the incoherent components of the scattered fields as shown in Figure 3.8. The simulation parameters are shown in Table 3.4. Good agreements can be seen between SEBCM, SPM3, and MoM.

Comparing these three solutions in the computational aspect, SPM3 has the highest ef-

Table 3.4: SIMULATION PARAMETERS FOR TWO-ROUGH-SURFACE CASE FOR VALIDATION WITH SPM AND MOM.

kh_1	kl_{c1}	kh_2	kl_{c2}	ε_1	ε_2	d	Surf. Type
$\pi/25$	π	$\pi/25$	π	5.4+0.44i	11.27+i	$\lambda_0/5$	Gauss. corr.

ficiency as an analytical approach but with limited validity over roughness. While SEBCM and MoM can both be applied to large roughnesses, MoM needs to solve a much larger number of unknowns for the same problem geometry than SEBCM, since MoM unknowns represent spacial discretization and the segment is usually one tenth of the wavelength. Particularly, the advantage of SEBCM in computational efficiency becomes more obvious when the number of layers increases.
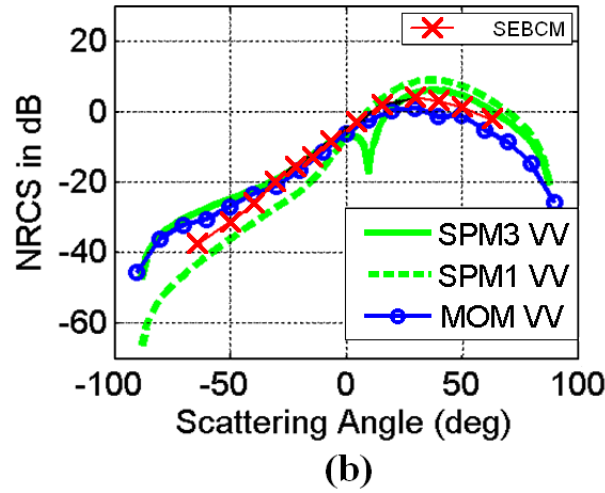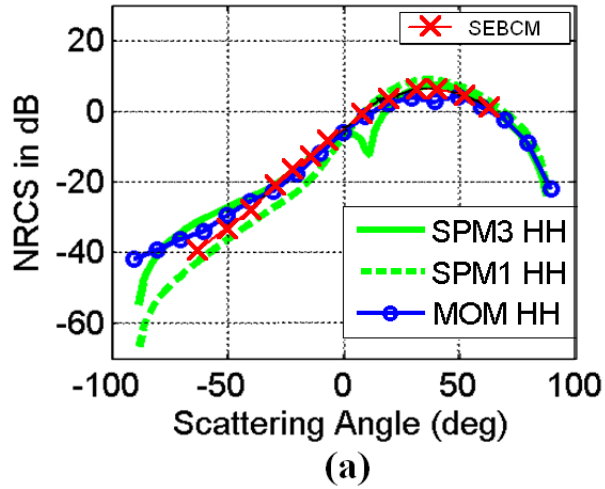
Figure 3.7: Comparison of incoherent scattering cross sections between SEBCM, SPM and MoM for two-rough-surfaces with $d = 0.8\lambda_0$ and the rest parameters in Table 3.3.

3.4 Simulation Results

The validated multilayer SEBCM model is further utilized for studying the scattering cross section sensitivity to variations of the geophysical parameters in the subsurface with the goal of investigating soil moisture. These parameters include surface separation, subsurface roughness, and subsurface layer soil moisture content. Simulations are performed at both L-band (1.2GHz) and P-band (435MHz) frequencies. All results shown in this section are for incidence angle of $40°$ and use Gaussian surfaces with exponential correlation
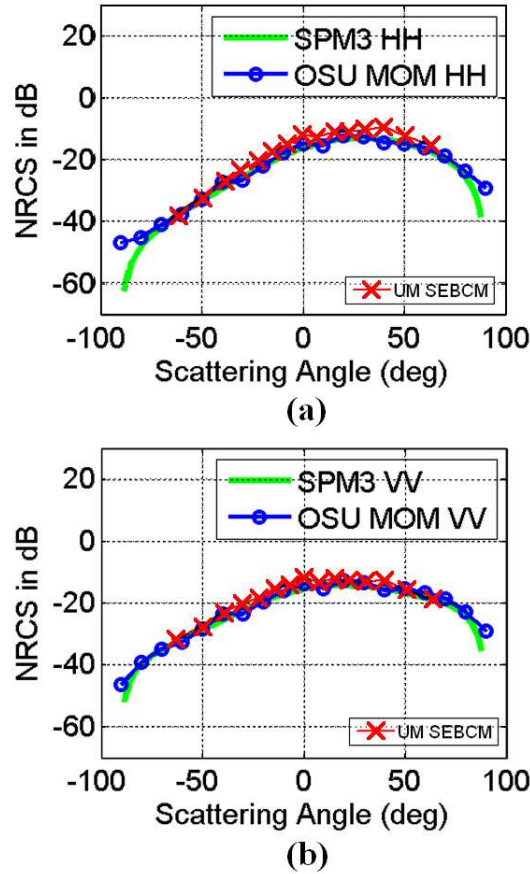
Figure 3.8: Comparison of incoherent scattering cross sections between SEBCM, SPM and MoM for two-rough-surfaces with parameters in Table 3.4.

function, which are generated by constructing their spectrum and using inverse Fourier transform (Appendix A). The results are obtained by averaging 20 realizations.

3.4.1 Perturbations in Layer Separation

First, we simulated two-rough-surface cases with various surface separations: $d = 30$ cm, 50 cm, and 100 cm. As can be seen from the parameters listed in Table 3.5, with the same correlation length, the top surface is rougher than the bottom one; and the lower-most layer is assumed to have higher moisture content than the middle layer.

Figure 3.9 shows the results of the co-polarized scattered fields at P-band. The zoomed-in views are presented in the lower part of the figure, from which $\sim$2 dB difference can be

58

Table 3.5: SIMULATION PARAMETERS FOR TWO-ROUGH-SURFACE CASE FOR PERTURBATIONS IN SURFACE SEPARATION.

frequency	kh_1	kl_{c1}	kh_2	kl_{c2}
435MHz	0.15	1.0	0.1	1.0

ε_1	ε_2	d
$5.4 + i0.44$	$11.27 + i1.0$	30 cm, 50 cm, 100 cm
		$(0.435\lambda_0, 0.726\lambda_0, 1.451\lambda_0)$
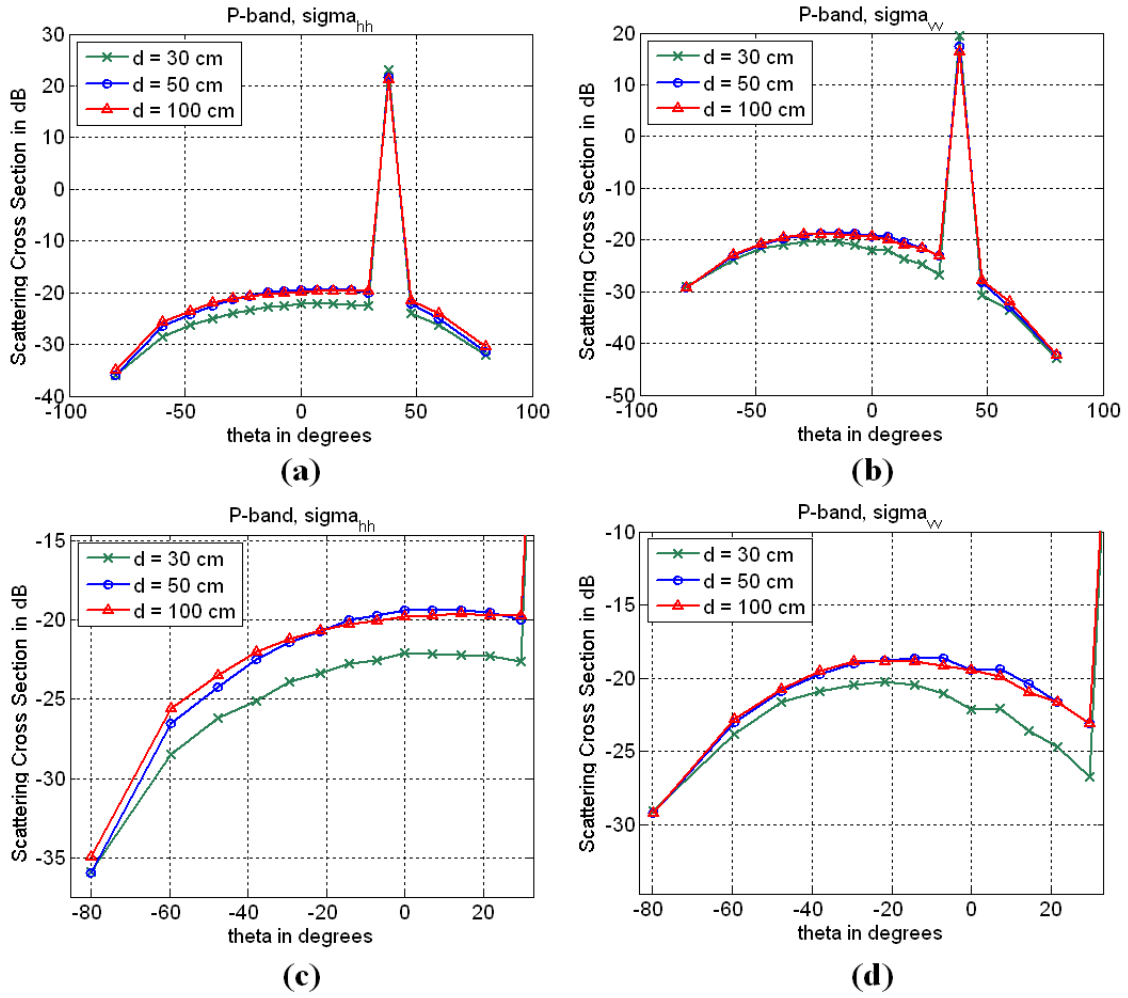
Figure 3.9: Scattering from two-rough-surfaces at P-band as a function of the surface separation: (a) σ_{hh}; (b) σ_{vv}; (c) zoomed-in view of σ_{hh}; (d) zoomed-in view of σ_{vv}. (Table 3.5)
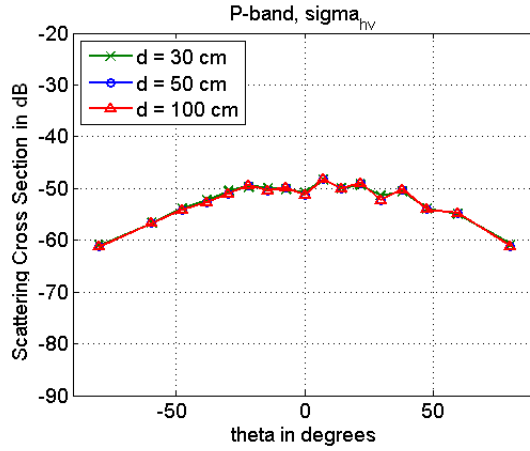
Figure 3.10: Cross-pol scattering from two-rough-surfaces at P-band as a function of the surface separation. (Table 3.5)

seen between results of 30 cm and 50 cm separations in the backscattering direction. Only a small difference appears between results of 50 cm and 100 cm separations, which is due to the limited penetration depth at P-band. The penetration depth can be estimated from [29] using,

$$\delta_p = \frac{\lambda_0 \sqrt{\varepsilon'}}{2\pi\varepsilon''} \tag{3.19}$$

when $\varepsilon''/\varepsilon' < 0.1$. At P-band, $\delta_p \approx 57.97$ cm, meaning that, in both the 50 cm and 100 cm separation cases, the subsurface is barely detected, and therefore their backscattering coefficients appear similar.

At L-band, simulation results do not show observable differences for these surface separations due to the small penetration depth of this frequency, which is estimated to be $\sim$21 cm.

The cross-polarized fields are shown in Figure 3.10, their sensitivity to the layer separation change is small.

3.4.2 Perturbations in Subsurface Roughness

Fixing the layer separation to be 10 cm, scattered fields from the two-rough-surface structure are simulated for both P-band and L-band as a function of subsurface statistics

to study the scattering sensitivity to the subsurface roughnesses. In these simulations, the sand/clay composition is assumed to be 0.66/0.1 in the middle layer, and 0.36/0.4 in the bottom layer. Values of 5% and 20% moisture contents are assumed in the middle and bottom layers, respectively. The dielectric permittivities in each layer at every frequency are calculated and listed in Table 3.6 and 3.7, using the model in [49] and [50].

Keeping the top surface statistics and the subsurface correlation-length-to-standard-deviation ratio $l_{c2}/h_2 = 10$ constant, simulations with increasing subsurface roughness standard deviation h_2 ($h_2 = 0.25$ cm, 1 cm, 2 cm, and 3 cm) are done at both 1.2GHz and 435MHz.

Table 3.6: SIMULATION PARAMETERS FOR TWO-ROUGH-SURFACE CASE FOR PERTURBATIONS IN SUBSURFACE ROUGHNESS AT L-BAND.

frequency	m_{v1}	m_{v2}	d
1.2GHz	5%	20%	10 cm
	$(6.15 + i0.44)$	$(14.16 + i1.6)$	$(0.4\lambda_0)$

h_1	l_{c1}/h_1	h_2	l_{c2}/h_2
1.5cm	6	0.25cm, 1cm, 2cm, 3cm	10
$(0.06\lambda_0)$		$(0.01\lambda_0, 0.04\lambda_0, 0.08\lambda_0, 0.12\lambda_0)$	

Table 3.7: SIMULATION PARAMETERS FOR TWO-ROUGH-SURFACE CASE FOR PERTURBATIONS IN SUBSURFACE ROUGHNESS AT P-BAND.

frequency	m_{v1}	m_{v2}	d
435MHz	5%	20%	10 cm
	$(6.15 + i0.95)$	$(14.23 + i3.14)$	$(0.145\lambda_0)$

h_1	l_{c1}/h_1	h_2	l_{c2}/h_2
1.5cm	6	0.25cm, 1cm, 2cm, 3cm	10
$(0.02\lambda_0)$		$(0.004\lambda_0, 0.015\lambda_0, 0.03\lambda_0, 0.044\lambda_0)$	

Results in L-band show very small difference (< 0.1 dB) between cases of $h_2 = 0.25$ cm and $h_2 = 3$ cm. Whereas, the P-band results shown in Figure 3.11 appear difference of ~ 9 dB in both HH and VV backscattering cross sections for the subsurface roughness changing from 0.25 cm to 3 cm.

Table 3.8: Simulation Parameters for Two-Rough-Surface Case for Perturbations in Subsurface Roughness at P-band with Larger Layer Separation.

frequency	m_{v1}	m_{v2}	d
435MHz	5%	20%	30 cm
	$(6.15 + i0.95)$	$(14.23 + i3.14)$	$(0.435\lambda_0)$

h_1	l_{c1}/h_1	h_2	l_{c2}/h_2
1.5cm	6	0.25cm, 1cm, 2cm, 3cm	10
$(0.02\lambda_0)$		$(0.004\lambda_0, 0.015\lambda_0, 0.03\lambda_0, 0.044\lambda_0)$	

Figure 3.11: Scattering from two-rough-surface at P-band as a function of the subsurface roughness with layer separation of 10 cm: (a) σ_{hh}; (b) σ_{vv}. (Table 3.7)

Moreover, at P-band, another case with the same roughness parameters but an increased surface separation (30 cm) is further simulated to examine its effect on the scattering sensitivity to the subsurface roughness. The simulation parameters are shown in Table 3.8. As expected, increasing the layer separation reduces the difference to ~5 dB for the same range of roughness change as shown in Figure 3.12.

3.4.3 Perturbations in Subsurface Layer Soil Moisture

Sensitivity of the total scattering cross section to the subsurface layer moisture content relates directly to the requirements of radar system design for subsurface soil moisture
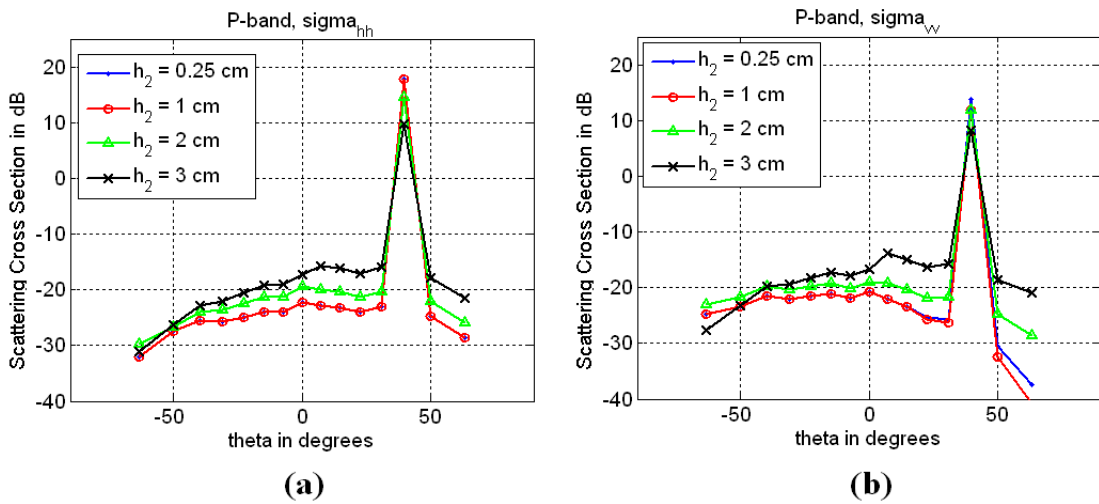
Figure 3.12: Scattering from two-rough-surface at P-band as a function of the subsurface roughness with layer separation of 30 cm: (a) σ_{hh}; (b) σ_{vv}. (Table 3.8)
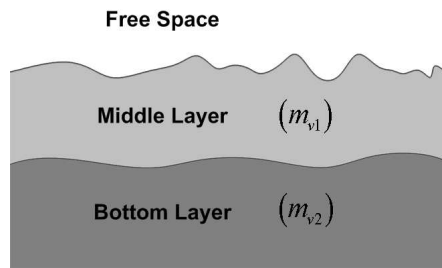
Figure 3.13: Soil moisture in subsurface layers.

sensing. Using the multilayer SEBCM model, we are capable of simulating the scattering from the two-rough-surface structure as a function of the bottom layer moisture content at P-band (shown in Figure 3.13). Same sand/clay compositions are used as above; surface separation is 10 cm. Simulations are done for the middle layer moisture content being 5% and 15% respectively. In either case, the bottom layer moisture is increased from 5% to 30% to observe changes in the scattered field. Corresponding permittivities, as well as the surface and subsurface roughness statistics, are listed in Table 3.9 and 3.10.

Results are shown in Figure 3.14 and Figure 3.15 for the middle layer moisture content being 5% and 15% respectively. In Figure 3.14, as m_{v2} increases from 5% to 30%, ~6 dB difference can be observed, whereas in Figure 3.15, this difference is reduced to ~2 dB.

63

Table 3.9: SIMULATION PARAMETERS FOR TWO-ROUGH-SURFACE CASE FOR PERTURBATIONS IN SUBSURFACE LAYER MOISTURE CONTENT AT P-BAND WITH LOWER MOISTURE CONTENT IN THE MIDDLE LAYER.

frequency	h_1	l_{c1}/h_1	h_2	l_{c2}/h_2	d
435MHz	2cm	10	1cm	10	cm
	$(0.029\lambda_0)$		$(0.015\lambda_0)$		$(0.145\lambda_0)$

m_{v1}	m_{v2}
5%	5%, 10%, 15%, 20%, 25%, 30%
$(6.17+i0.95)$	$(5.15+i1.26, 7.8+i1.98, 10.85+i2.59,$
	$14.23+i3.14, 17.94+i3.67, 21.95+i4.17)$

Table 3.10: SIMULATION PARAMETERS FOR TWO-ROUGH-SURFACE CASE FOR PERTURBATIONS IN SUBSURFACE LAYER MOISTURE CONTENT AT P-BAND WITH HIGHER MOISTURE CONTENT IN THE MIDDLE LAYER.

frequency	h_1	l_{c1}/h_1	h_2	l_{c2}/h_2	d
435MHz	2cm	10	1cm	10	10 cm
	$(0.029\lambda_0)$		$(0.015\lambda_0)$		$(0.145\lambda_0)$

m_{v1}	m_{v2}
15%	5%, 10%, 15%, 20%, 25%, 30%
$(13.24+i1.63)$	$(5.15+i1.26, 7.8+i1.98, 10.85+i2.59,$
	$14.23+i3.14, 17.94+i3.67, 21.95+i4.17)$

This is consistent with the expectation that since the increased moisture content raises the middle layer loss, a small amount of energy from the subsurface can propagate through the middle layer, i.e., the scattered fields are less sensitive to changes in the bottom layer.

3.4.4 Media with Dielectric Profiles

Subsurface soil moisture typically has a depth-varying profile. Hence, instead of assuming homogeneous medium layers, media with dielectric profiles provide a more realistic model of soil moisture below the surface. With the multilayer SEBCM, we are able to solve the scattering from multilayer rough surfaces within arbitrary depth-varying dielectric profiles.

An example of soil moisture profile is shown in Figure 3.16 (a), where the subsurface
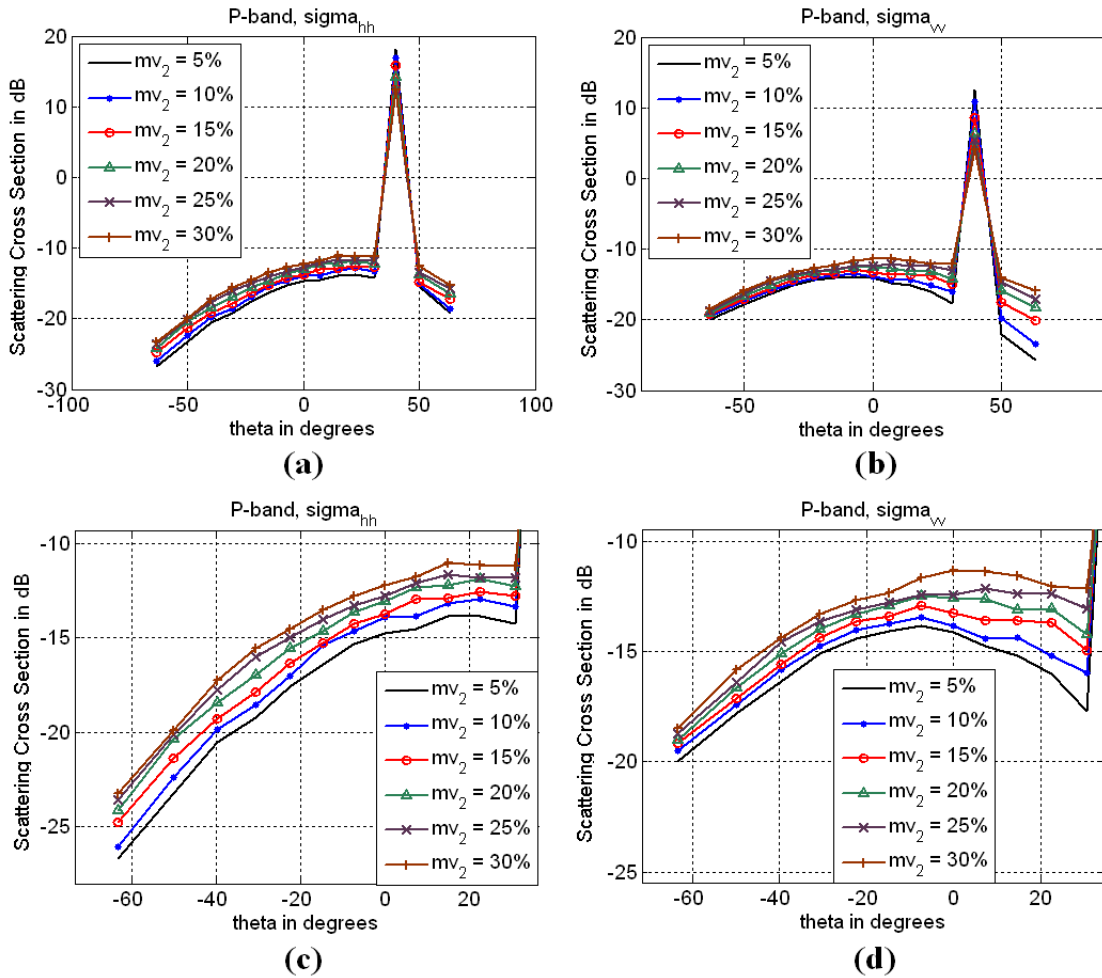
Figure 3.14: Scattering from two-interface layers at P-band as a function of the bottom layer soil moisture with the middle layer soil moisture of 5 %: (a) σ_{hh}; (b) σ_{vv}; (c) zoomed view of σ_{hh}; (d) zoomed view of σ_{vv}. (Table 3.9)

interface location is marked at 30 cm below the top surface. This subsurface is, for example, a result of soil composition change, that is, where the sand/clay composition changes from 0.66/0.1 in the upper layer to 0.36/0.4 in the lower layer. Figure 3.16 (b) plots the corresponding real and imaginary parts of the relative permittivity profile using the model in [49] and [50], where sharper changes can be seen at -30 cm for both curves. Statistics of both surfaces are shown in Table 3.11.

Figure 3.16 (c) and (d) show the multilayer SEBCM solutions of the total scattering. The co-polarized radar cross sections are plotted in Figure 3.16 (c), and the cross-polarized
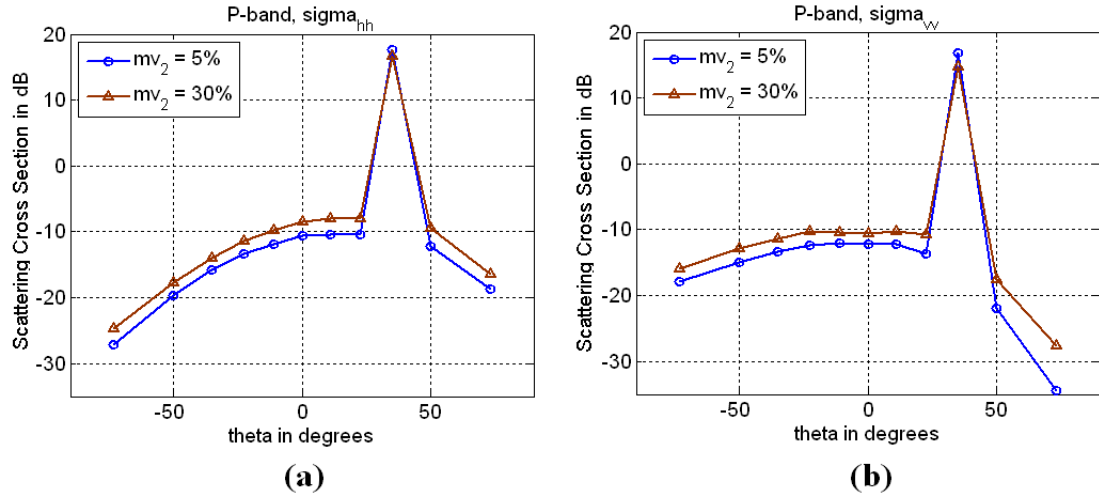
Figure 3.15: Scattering from two-interface layers at P-band as a function of the bottom layer soil moisture with the middle layer soil moisture being increased to 15 %: (a) σ_{hh}; (b) σ_{vv}. (Table 3.10)

Table 3.11: SIMULATION PARAMETERS FOR TWO-ROUGH-SURFACE CASE WITH A DIELECTRIC PROFILE IN THE MEDIA.

frequency	h_1	l_{c1}	h_2	l_{c2}
435MHz	3cm	50cm	3cm	50cm
	$(0.044\lambda_0)$	$(0.725\lambda_0)$	$(0.044\lambda_0)$	$(0.725\lambda_0)$

middle soil composition	bottom soil composition	d
sand = 0.66, clay = 0.1	sand = 0.36, clay = 0.4	30 cm
		$(0.145\lambda_0)$

components are shown in Figure 3.16 (c), from which the reciprocity of σ_{hv} and σ_{vh} can be seen.

Another example of scattering from soil moisture profile is shown in Figure 3.17, where all parameters keep the same except that a different moisture profile is used (Figure 3.17(a)). This profile has enhanced water content in the top layer, which results in a little larger RCS. The difference between σ_{hh} and σ_{vv} is small (as well as in the previous example). However, their coherent phase different in backscattering is observable as shown in Figure 3.18.

66
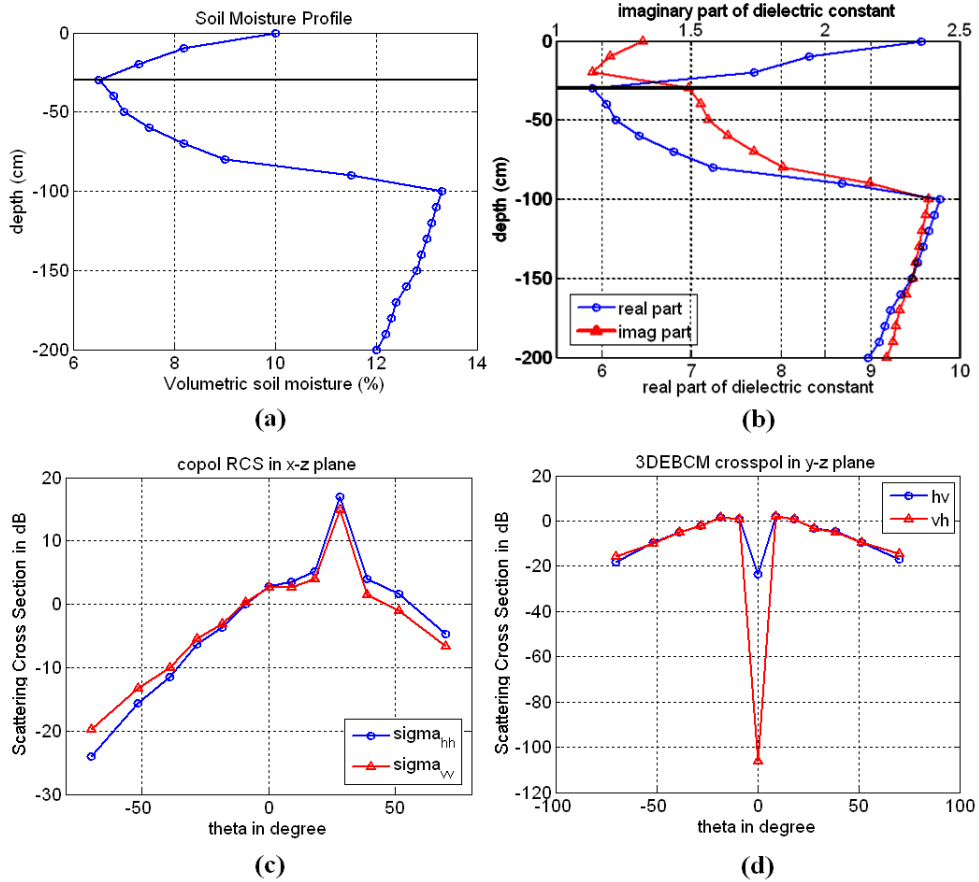
Figure 3.16: Scattering from media with a depth-varying dielectric profile and two rough surfaces at P-band: (a) volumetric soil moisture content, where the line indicates the location of the subsurface; (b) the correspondent profile of dielectric constant; (c) co-polarized RCS; (d) cross-polarized RCS. (Table 3.11)

3.5 Summary and Conclusion

A solution to three-dimensional electromagnetic scattering from multilayer rough surfaces within homogeneous or inhomogeneous media is developed and presented in this chapter using the scattering matrix approach and the stabilized extend boundary condition method (SEBCM). The SEBCM is applied to compute the single-surface scattering matrix of every rough surface in the geometry. Its large validity domain over surface roughness allows the application of the multilayer model to cases involving very rough surfaces. Through the scattering matrix approach, surface scattering matrices and medium propagation matrices are cascaded to obtain the total scattering from the multilayer structure. This

67
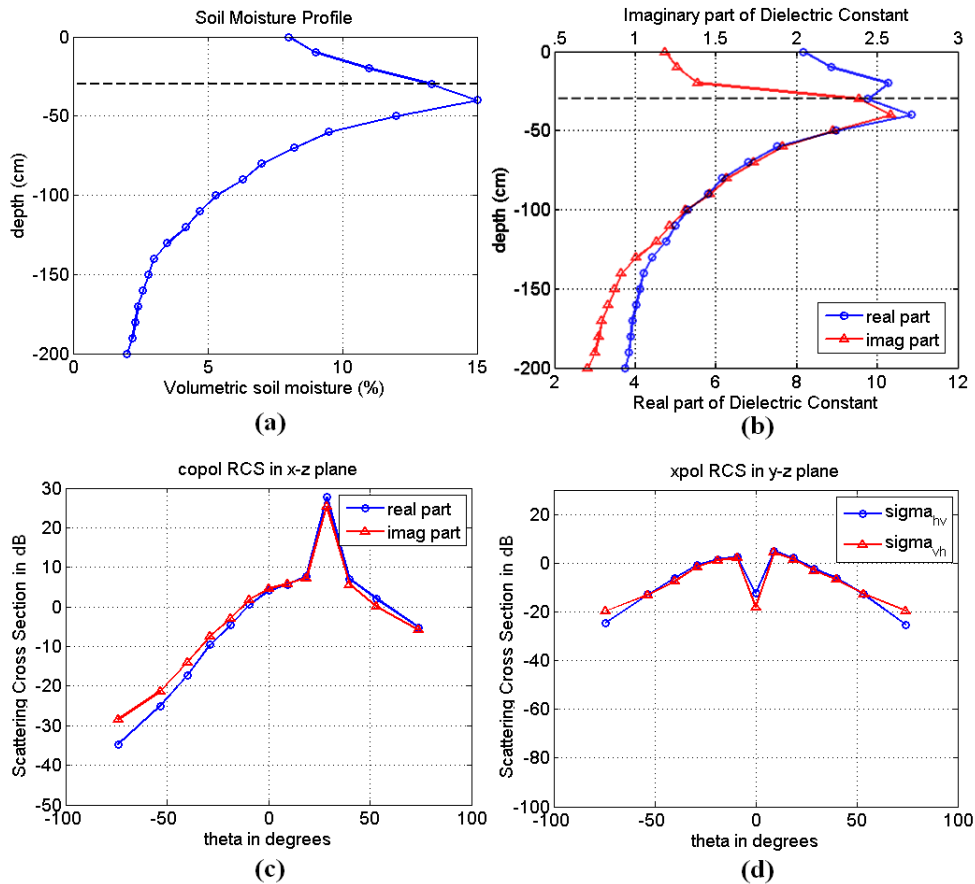
Figure 3.17: Scattering from media with a depth-varying dielectric profile and two rough surfaces at P-band: (a) volumetric soil moisture content, where the line indicates the location of the subsurface; (b) the correspondent profile of dielectric constant; (c) co-polarized RCS; (d) cross-polarized RCS. (Table 3.11)

approach enables us to efficiently extend the model to more subsurface layers. With high computational efficiency of the SEBCM compared to the numerical methods, this multi-layer SEBCM may be the most feasible approach currently available for solving multilayer rough surface scattering problem involving large roughnesses.

Besides the model validation with SPM and MoM, we presented in this work a sensitivity study utilizing the multilayer SEBCM model. In this study, total scattering cross sections at P-band and L-band are simulated with variations in the ground parameters including surface separation, subsurface roughness, and sublayer moisture content. Simulation results provide new and helpful information for applications of subsurface soil moisture
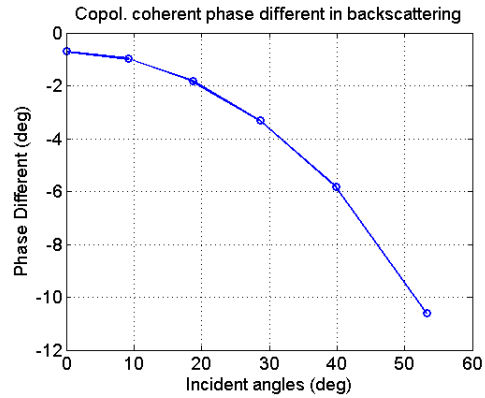
Figure 3.18: Copolarized coherent phase difference in the case of the moisture profile in Figure 3.17.

remote sensing. As expected, the L-band EM scattering is not very sensitive to changes in the subsurface and sublayer properties appearing lower than its limited penetration depth of approximately 10 cm. On the other hand, sensitivity of the P-band wave scattering depends greatly on the moisture content of the top layer and the subsurface layers. Within the penetration depth and with relatively dry soil on top, the P-band scattering cross sections appear quite sensitive to the subsurface roughness and sublayer moisture content. This sensitivity is largely reduced by increasing the top layer soil. We also showed the capability of solving scattering from multilayer surfaces within media with depth-varying dielectric properties using the multilayer SEBCM, which simulates the soil with a moisture profile distribution. The multilayer SEBCM model developed here can provide important information for radar system design for subsurface remote sensing. Moreover, once combined with volume scattering contributions of random media within the soil layers, this model can further be used to study the role of vegetation roots and other inclusions in enhanced sensing of soil moisture, which will be presented in next chapter.

69

CHAPTER 4

Scattering from Random Media in Multilayer Rough Surfaces

In this chapter, a 3D scattering model from layered arbitrarily random rough surfaces with embedded discrete random scatterers is constructed based on the scattering matrix approach, which is discussed in the previous chapter. Scattering matrix of a single rough surface is found using the stabilized extended boundary condition method (SEBCM) presented in Chapter 2. Meanwhile, by finding the T-matrices of discrete scatterers using analytical or numerical methods, the random medium scattering solution is found based on the recursive T-matrix approach or generalized iterative extended boundary condition method (GIEBCM), and near-to-far field transformed numerical plane wave expansion of the vector spherical harmonics. Solutions provided in this work include multiple scattering effects among the medium scatterers and between subsurfaces and sublayers. The high computational efficiency and accuracy of this method enable it to serve as a powerful tool for studying the role of vegetation roots and other sublayer inhomogeneities in retrieval of subsurface and root-zone soil moisture from radar measurements.

4.1 Introduction

Subsurface remote sensing provides important information in many applications, such as monitoring the changes in the subsurface structures for facility constructions and landslide warning, locating the permafrost depth to assess the impact of global warming causing loss of wetlands and civil infrastructure damage, as well as mapping of the soil moisture profiles in bare or vegetated areas. The latter is one of the critical components in modeling the global water and energy cycle in support of global climate change studies as well as improving long-term weather forecasts.

For subsurface remote sensing, low frequency radar systems need to be used; their large penetration depth enables the measurement of electromagnetic scattering from deep soil layers. However, media comprising the subsurfaces in nature are usually inhomogeneous; soils typically have buried rocks, ice particles, or vegetation roots. Hence, impact of these buried objects on the total radar signal needs to be understood and calculated. In particular, for retrieval of soil moisture profiles in the root zone of vegetated areas, the effect of vegetation roots on radar measurements needs to be accurately modeled. Assessment of the scattering contribution from the vegetation roots and incorporation of their effect in root-zone soil moisture retrieval algorithms demand an efficient and accurate forward scattering model of layered rough surfaces with buried discrete random media, which is the focus of this chapter.

To simulate the sublayer inhomogeneities, we consider three types of scatterers as examples: spheres, short-cylinders, and root-structured cylinder clusters. Spherical scatterers are good models of rocks and ice particles, which usually have small dielectric constant (< 10) [29]. Cylinders and cylinder clusters are used to simulate the tree roots as shown in Figure 4.2. Properties of the vegetation roots having impact on the radar measurements are highly influenced by soil conditions. From few studies of low frequency dielectric properties of the vegetation roots, the dielectric constant of the root is estimated to vary largely from ~ 5 to ~ 40 depending on the temperature and water content [29][51][52]. A basic cylinder cluster can be constructed according to the natural tree root pattern [53].

The random medium scattering solutions required in subsurface sensing applications should include the coherent and high-order effects within the medium, which is critical for getting accurate predictions of backscattering coefficients. During the past several decades, several approaches have been developed for solving scattering from random media. For example, methods based on radiative transfer equations, which are derived based on power conservation and field intensity tracking through the media, are commonly applied. However, these methods are incoherent approaches ignoring coherent interactions among scatterers. Other methods, including those based on analytical derivations (e.g., the effective field approximation and the quasi-crystalline approximation) and those based on wave theory, consider only low-order scattering.

In this work, scattering from discrete random media consisting of spheres or short-cylinders is solved using the recursive Transition matrix (T-matrix) method, which was developed two decades ago [35] but has never been efficiently used for random media applications and especially in the field of microwave remote sensing. The T-matrix approach has high computational efficiency and includes higher order interactions among scatterers, providing rather accurate solutions. As required by this method, the T-matrix of every single scatterer within the medium needs to be obtained first: the T-matrix of a spherical scatterer can be found from the Mie-scattering coefficients [16]; and the T-matrix of a short-cylinder is calculated using the extended boundary condition method (EBCM) [26], which gives very efficient solution compared to the available numerical solutions such as method of moments (MoM).

The above methodology has its limitations when applying to the root-like cylindrical clusters: 1) the recursive T-matrix method requires the external circumscribed spheres of the scatterers not being overlapped; 2) the T-matrix solution of a single cylinder using EBCM is not accurate when the length-to-diameter ratio of the cylinder being much larger than 1. Both limitations are encountered in solving scattering from the root-like cylindrical clusters. Therefore, we developed the generalized iterative extended boundary condition method (GIEBCM), based on the work in [54] that solves only the horizontally or verti-

cally arranged long cylinders.

The T-matrix describing the total scattering from the medium needs to be further transformed to scattering matrix (S-matrix) for incorporation to the layered media scattering model. An efficient way of transforming T-matrix to S-matrix exists in 2D, but has never been reported in 3D. This requires knowing both the multipole expansion of plane waves and the plane wave expansion of vector spherical harmonics. The former expansion has been developed already in an analytical form, while the latter one does not exist analytically, but a numerical plane wave expansion of the scalar spherical harmonics has been shown in [55]. However, the far field calculation using this method would lose accuracy due to the computational errors. In this work, we expanded the vector spherical harmonics numerically in terms of plane waves based on further development of the work in [55], and combined it with a near-to-far field transformation. This makes the T-matrix to S-matrix conversion feasible and therefore useful for remote sensing applications for the first time.

For scattering from rough surfaces, the stabilized extended boundary condition method (SEBCM) we discussed in chapter 2 is used, which is capable of solving scattering from surfaces with large roughnesses at high efficiency. From the scattering matrices derived above, scattering from the overall multilayered structure with buried random media can be found by scattering matrix cascading. Validation of the random media scattering is done by comparing with the experimental measurements; and results of the scattering from rough surfaces with the buried random media will be shown.

The model constructed in this work can be used to estimate the impact of the tree and crop roots or other buried inhomogeneities on the radar measurement of subsurface soil moisture. It can therefore incorporate the vegetation roots as one of the parameters in the algorithms for root-zone soil moisture retrieval. It is important to note that the effects of above-ground vegetation are not the subject of investigation in this dissertation. The radar response of vegetation has been studied extensively in the past, and will be assume to be available independently of the subsurface model developed here. This work, therefore, is concerned with investigating the effects of subsurface scatterers and layering structure on

altering the radar response from the ground.

4.2 Problem Geometry
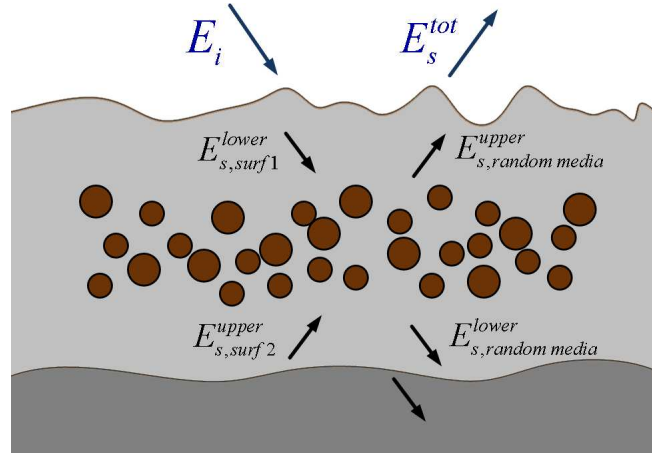
Figure 4.1: Scattering from rough surfaces with buried random spheres

For inhomogeneities other than roots buried in the ground sublayer, such as rocks, ice particles, and so on, spherical scatterers can be used as a basic model. Geometry of scattering from multiple spherical scatterers between surface and subsurface is shown in Figure 4.1. Every sphere has dielectric property defined by its permittivity ε_s and permeability μ_s. Size of the sphere is determined by the radius a. The dielectric properties and dimensions can vary among the scatterers. These spherical scatterers can distributed randomly or with certain pre-defined pattern. The distribution can be fully described by the sphere center locations.

The background medium has dielectric property of $(\varepsilon_{bg}, \mu_{bg})$; it simulates the soil with given water content.

When the area is vegetated, the problem geometry becomes more complex. As shown in Figure 4.2, root of a single plant can be viewed as a cluster of cylinders distributed in a certain pattern. This is a good root model when the plants are away from each other with sufficient distances, such as a sparse woods/forest. However, for an area with higher vege-
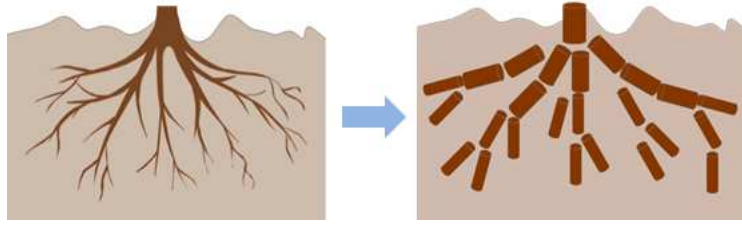
Figure 4.2: Simulating roots with cylinders

tation density, randomly distributed cylinders are better modeling the situation as shown in Figure 4.3.

The cylindrical scatterer has dielectric property defined by its permittivity ε_s and per-
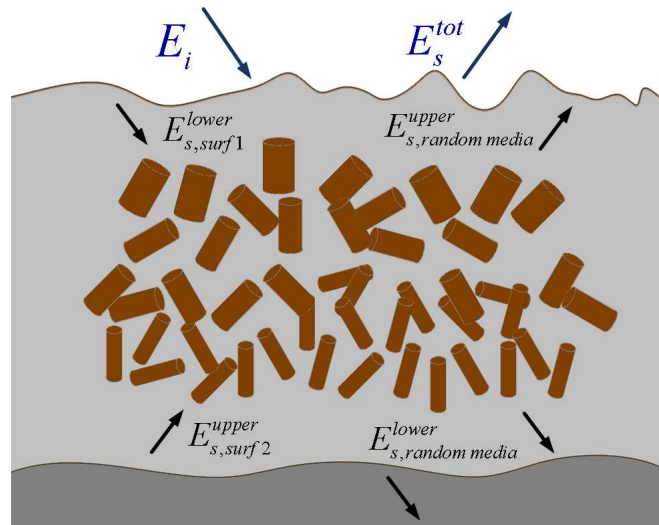
Figure 4.3: Scattering from rough surfaces with buried random cylinders

meability μ_s. Size of the cylinder is determined by the length L and the radius a of its cross section. The dielectric properties and dimensions can vary among the scatterers. Distribution of the scatterers is random, and can be described by their center locations and orientation angles (θ_s, ϕ_s). The background medium has dielectric property of $(\varepsilon_{bg}, \mu_{bg})$.

4.3 Analysis and Formulation

The total scattering from the layered structure of rough surfaces with buried media is solved by cascading their scattering matrices as discussed in Chapter 3. Here we will focus on solving the scattering matrix from the buried inhomogeneities.

For media of spherical and cylindrical scatterers, we obtain its scattering matrix from the transition matrix, which is found by using the recursive T-matrix method for spherical and short-cylindrical scatterers, and generalized iterative extended boundary condition method for long- or root-like cylindrical clusters. Details of the computation are given as following.

4.3.1 Single Scatterer T-matrix

Single spherical scatterer T-matrix

The T-matrix of a single sphere can be found from the Mie-scattering coefficients expressed as [16],

$$\bar{\bar{T}}_{1(1)} = \begin{bmatrix} \bar{\bar{T}}_M & 0 \\ 0 & \bar{\bar{T}}_N \end{bmatrix} \tag{4.1}$$

$$\bar{\bar{T}}_M = \mathrm{diag}\left\{ -\frac{j_n(k_s a)[ka\,j_n(ka)]' - j_n(ka)[k_s a\,j_n(k_s a)]'}{j_n(k_s a)[ka\,h_n(ka)]' - h_n(ka)[k_s a\,j_n(k_s a)]'} \right\} \tag{4.2}$$

$$\bar{\bar{T}}_N = \mathrm{diag}\left\{ -\frac{k_s^2 a^2 j_n(k_s a)[ka\,j_n(ka)]' - k^2 a^2 j_n(ka)[k_s a\,j_n(k_s a)]'}{k_s^2 a^2 j_n(k_s a)[ka\,h_n(ka)]' - k^2 a^2 h_n(ka)[k_s a\,j_n(k_s a)]'} \right\} \tag{4.3}$$

b. Single Short Cylindrical Scatterer T-matrix

T-matrix of a short-length (length-to-diameter ratio < 3.5) can be found using the extended boundary condition method (EBCM) in [26] as,

$$\bar{\bar{T}} = -\mathrm{Rg}\bar{\bar{Q}} \cdot \bar{\bar{Q}}^{-1} \tag{4.4}$$

where

$$\bar{\bar{Q}} = \left[\begin{array}{cc} \left[Q_{nm,lk}^{MM} \right] & \left[Q_{nm,lk}^{MN} \right] \\ \left[Q_{nm,lk}^{NM} \right] & \left[Q_{nm,lk}^{NN} \right] \end{array} \right] \tag{4.5}$$

Matrix $\mathrm{Rg}\bar{\bar{Q}}$ relates the surface unknowns with the scattered field, while matrix $\bar{\bar{Q}}$ relates the incident waves with the surface unknowns. The surface unknowns and the fields are all expanded in terms of vector spherical harmonics denoted as $\bar{M}$ and $\bar{N}$. The matrix elements $Q_{nm,lk}^{MM}$, $Q_{nm,lk}^{MN}$, $Q_{nm,lk}^{NM}$, and $Q_{nm,lk}^{NN}$ can be obtained from the surface integral of vector spherical harmonics as

$$Q_{nm,lk}^{MM} = \frac{(-1)^m k_0^2}{n(n+1)} \int_S ds' \hat{n}' \cdot \left[\left(\frac{\mu_0 k_1}{\mu_1 k_0} \right) \cdot \mathrm{Rg}\bar{N}_l^k(k_1, \bar{r}') \times \bar{M}_n^{-m}(k_0, \bar{r}') \right.$$
$$\left. - \mathrm{Rg}\bar{M}_l^k(k_1, \bar{r}') \times \bar{N}_n^{-m}(k_0, \bar{r}') \right] \tag{4.6}$$

$$Q_{nm,lk}^{MN} = \frac{(-1)^m k_0^2}{n(n+1)} \int_S ds' \hat{n}' \cdot \left[\left(\frac{\mu_0 k_1}{\mu_1 k_0} \right) \cdot \mathrm{Rg}\bar{M}_l^k(k_1, \bar{r}') \times \bar{M}_n^{-m}(k_0, \bar{r}') \right.$$
$$\left. - \mathrm{Rg}\bar{N}_l^k(k_1, \bar{r}') \times \bar{N}_n^{-m}(k_0, \bar{r}') \right] \tag{4.7}$$

$$Q_{nm,lk}^{NM} = \frac{(-1)^m k_0^2}{n(n+1)} \int_S ds' \hat{n}' \cdot \left[\left(\frac{\mu_0 k_1}{\mu_1 k_0} \right) \cdot \mathrm{Rg}\bar{N}_l^k(k_1, \bar{r}') \times \bar{N}_n^{-m}(k_0, \bar{r}') \right.$$
$$\left. - \mathrm{Rg}\bar{M}_l^k(k_1, \bar{r}') \times \bar{M}_n^{-m}(k_0, \bar{r}') \right] \tag{4.8}$$

$$Q_{nm,lk}^{NN} = \frac{(-1)^m k_0^2}{n(n+1)} \int_S ds' \hat{n}' \cdot \left[\left(\frac{\mu_0 k_1}{\mu_1 k_0} \right) \cdot \mathrm{Rg}\bar{M}_l^k(k_1, \bar{r}') \times \bar{N}_n^{-m}(k_0, \bar{r}') \right.$$
$$\left. - \mathrm{Rg}\bar{N}_l^k(k_1, \bar{r}') \times \bar{M}_n^{-m}(k_0, \bar{r}') \right] \tag{4.9}$$

where k_0 and k_1 are the wave numbers in the exterior and interior regions of the cylinder respectively; μ_0 and μ_1 denote permeability in these two regions. $\mathrm{Rg}\bar{\bar{Q}}$ replaces the $\bar{M}_{n,-m}$ and $\bar{N}_{n,-m}$ with the regular form $\mathrm{Rg}\bar{M}_{n,-m}$ and $\mathrm{Rg}\bar{N}_{n,-m}$.
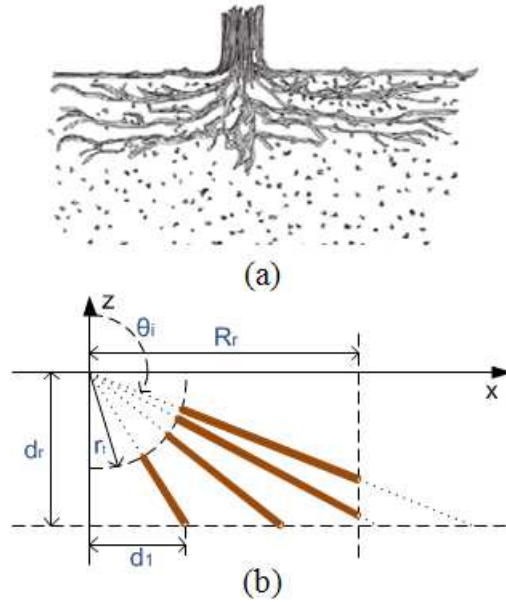
Figure 4.4: Modeling the basic root structure according to (a) [53].

Root-structured cylinder clusters

To simulate the tree roots, a basic structure is built as shown in Figure 4.4. According to [53], instead of growing downward at steep angles from the base of the tree trunk, most trees spread their roots near the surface, where soil conditions provide nutrients and moisture ($\sim$ 85% tree roots are within the top 0.5 m of soil). Usually the roots extend the range of one (at least) to three times of the radius of the canopy spread or two or three times the height of the tree. Therefore, we confine the root cylinders in the depth d_r and range R_r, starting from the range r_t, which is the diameter of the trunk. Uniformly distributing in the azimuth plane at ϕ_i, every root branch has N root cylinders counting from nadir. The elevation angle of the ith cylinder is defined as $\theta_i = \pi - \tan^{-1}(i \cdot d_1 / d_r)$ to have increasing density near the surface. The lower end is at $(i \cdot d_1 / \sin \theta_i, \theta_i, \phi_i)$, if $\theta_i > \theta_t = \pi - \tan^{-1}(R_r/d_r)$, otherwise, the cylinder end is at $(R_r / \sin \theta_i, \theta_i, \phi_i)$. Top ends of the cylinders are at (r_t, θ_i, ϕ_i). In this model, d_1 determines the root density, which is a function of soil moisture.

Its T-matrix is found using the generalized iterative extended boundary condition method that will be presented in Section 4.3.3.

4.3.2 Recursive T-matrix Method

The recursive T-matrix method is used to solve electromagnetic scattering from multiple scatterers. Details of this approach are discussed in [26], here the solution is briefly summarized here.

For a cluster of multiple spheres, the recursive process starts from the T-matrix of a single scatterer, and deduce the $(n+1)$-scatterer T-matrix from the n-scatterer T-matrix using the following translational matrices for coordinate transformation,

$$\bar{\bar{\alpha}}_{ji} = \begin{bmatrix} \bar{\bar{A}}_{ji}^{(h)} & \bar{\bar{B}}_{ji}^{(h)} \\ \bar{\bar{B}}_{ji}^{(h)} & \bar{\bar{A}}_{ji}^{(h)} \end{bmatrix} \quad (4.10) \qquad \bar{\bar{\beta}}_{ji} = \begin{bmatrix} \bar{\bar{A}}_{ji}^{(j)} & \bar{\bar{B}}_{ji}^{(j)} \\ \bar{\bar{B}}_{ji}^{(j)} & \bar{\bar{A}}_{ji}^{(j)} \end{bmatrix} \quad (4.11)$$

the recursive procedure can be described using Eq.(4.12) and Eq.(4.13),

$$\bar{\bar{T}}_{n+1(n+1)}{\cdot}\bar{\bar{\beta}}_{n+1,0} = \left[\bar{\bar{I}} - \bar{\bar{T}}_{n+1(1)}{\cdot}\bar{\bar{\alpha}}_{n+1,0}{\cdot}\bar{\bar{\tau}}_{(n)}{\cdot}\bar{\bar{\alpha}}_{0,n+1} \right]^{-1}{\cdot}\bar{\bar{T}}_{n+1(1)}{\cdot}\left[\bar{\bar{\beta}}_{n+1,0} + \bar{\bar{\alpha}}_{n+1,0}{\cdot}\bar{\bar{\tau}}_{(n)} \right] \quad (4.12)$$

$$\bar{\bar{\tau}}_{(n+1)} = \bar{\bar{\tau}}_{(n)} + \left[\bar{\bar{\beta}}_{0,n+1} + \bar{\bar{\tau}}_{(n)}{\cdot}\bar{\bar{\alpha}}_{0,n+1} \right]{\cdot}\bar{\bar{T}}_{n+1(n+1)}{\cdot}\bar{\bar{\beta}}_{n+1,0} \quad (4.13)$$

where the subscript $m(n)$ of $\bar{\bar{T}}$ denotes that the T-matrix is for n scatterers in the presence of m scatterers. The aggregate T-matrix of n scatterers is

$$\bar{\bar{\tau}}_{(n)} = \sum_{i=1}^{n} \bar{\bar{\beta}}_{0i} \cdot \bar{\bar{T}}_{i(n)} \cdot \bar{\bar{\beta}}_{i0} \quad (4.14)$$

This method takes into account higher order interactions among scatterers, and provides accurate solutions at very high computational efficiency.

4.3.3   Generalized Iterative Extended Boundary Condition Method

When solving the transition matrix (T-matrix) of a root-like cylindrical cluster, we encounter with two limitations with methods mentioned above. First of all, the extended boundary condition method can solve T-matrix of a cylinder with only limited length-to-diameter ratio, which cannot be applied to those slender cylinders in the root-like cluster. Meanwhile, the recursive T-matrix method can only be applied when the external circumscribed spheres of the scatterers are not overlapped, which is not the case in the root-model either. In order to solve the T-matrix of the root-like cluster, we developed the generalized iterative extended boundary condition method.

The basic idea of this method has been discussed in [54], where it is only be developed for horizontally or vertically arranged cylinders. With the three-dimensional frame transformation, we are able to generalize and implement the method for arbitrary distributed cylinders.

To model the scattering from the cylindrical cluster, we treat the structure as cascaded
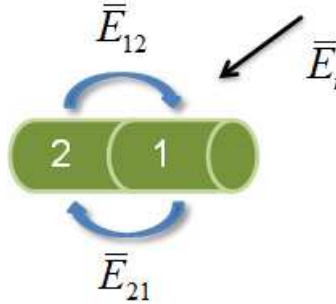
Figure 4.5: Cascaded sub-cylinders

short-length sub-cylinders (Figure 4.5), whose T-matrix is found using EBCM. We divide the long cylinders into a series of shorter ones to ensure convergence of the multipole expansions. The scattering from the cascaded subcylinders can be found using an iterative

technique [54], which is summarized below.

$$\begin{bmatrix} a_{ex,j}^{(M)} \\ a_{ex,j}^{(N)} \end{bmatrix} = \begin{bmatrix} a_{inc,j}^{(M)} \\ a_{inc,j}^{(N)} \end{bmatrix} + \sum_{i \neq j, 1 \leq i \leq N} \bar{\bar{\alpha}}_{ji} \cdot \begin{bmatrix} a_{sca,i}^{(M)} \\ a_{sca,i}^{(N)} \end{bmatrix} \qquad (4.15)$$

$$\begin{bmatrix} a_{sca,j}^{(M)} \\ a_{sca,j}^{(N)} \end{bmatrix} = T^{(j)} \cdot \begin{bmatrix} a_{ex,j}^{(M)} \\ a_{ex,j}^{(N)} \end{bmatrix} \qquad (4.16)$$

The process starts with assumption of no scattering from other sub-cylinders ($a_{sca,i}^{(M)} = 0$, $a_{sca,i}^{(N)} = 0$). Therefore, the exciting field on every sub-cylinder is the incident field under its coordinate frame as indicated in Eq.4.15. The scattered field from every sub-cylinders can be found using its T-matrix as in Eq.4.16. The exciting fields all sub-cylinders are updated by the calculated scattered fields through frame transformations using the translational matrices noted as $\bar{\bar{\alpha}}_{ji}$ in Eq.4.15. This process is repeated until the scattered fields from all sub-cylinders converge. Therefore, the total scattering from the cluster is obtained from the superposition of scattering from all sub-cylinders as

$$\begin{bmatrix} a_{sca, tot}^{(M)} \\ a_{sca, tot}^{(N)} \end{bmatrix} = \sum_{1 \leq i \leq N} \bar{\bar{\alpha}}_{0i} \cdot \begin{bmatrix} a_{sca,i}^{(M)} \\ a_{sca,i}^{(N)} \end{bmatrix} \qquad (4.17)$$

Translation between the main frame and the arbitrary cylinder frame is the key of applying this method to random distributed cylinders. To do this, we use two zxz-rotations and one z-axis translation. In Figure 4.6, the translation from the sub-cylinder frame to the main frame is illustrated. In the first zxz-rotation, the two z-rotations do nothing, but the x-rotation points the cylinder axis $\hat{z}_c$ to the main origin O. The cylinder axis $\hat{z}_c$ is $(\sin\theta_c \cos\phi_c, \sin\theta_c \sin\phi_c, \cos\theta_c)$, where θ_c and ϕ_c are the angles determining the cylinder orientation referring to the main frame. Therefore, the rotated frame (x'_c, y'_c, z'_c) has its z'_c to be $\hat{d}_{oc} = (\sin\theta_{oc} \cos\phi_{oc}, \sin\theta_{oc} \sin\phi_{oc}, \cos\theta_{oc})$. Note that, since cylinder is axis-symmetric, we can define $\hat{x}_c = \hat{z}_c \times \hat{d}_{oc}$. After the z-axis translation, we need to rotate the frame (x''_c, y''_c, z''_c) to be parallel to the main frame (x_0, y_0, z_0). This is done by rotating first

Figure 4.6: Translation from the sub-cylinder frame to the main frame

Table 4.1: EULER ANGLES FOR ROTATIONS OF THE TRANSLATION FROM THE SUB-CYLINDER FRAME TO THE MAIN FRAME.

Rotation description	α	β	γ
Rotate the cylinder axis pointing to the main frame origin	0	$\cos^{-1}\left(\hat{z}_c \cdot \hat{d}_{oc}\right)$	0
Rotate the cylinder frame to be parallel to the main frame	$\frac{5\pi}{2} - \phi_{oc}$	θ_{oc}	$\begin{array}{ll}\cos^{-1}\left(\hat{x}_c'' \cdot \hat{x}_c'''\right) & \hat{x}_c'' \cdot \hat{z}_0 \geq 0 \\ 2\pi - \cos^{-1}\left(\hat{x}_c'' \cdot \hat{x}_c'''\right) & \hat{x}_c'' \cdot \hat{z}_0 < 0\end{array}$

$^{*}\hat{x}_c''' = \hat{z}_c'' \times \hat{z}_0$

around $\hat{z}_c''$-axis to align $\hat{x}_c''$ to $\hat{x}_c''' = \hat{z}_c'' \times \hat{z}_0$; then rotating around $\hat{x}_c'''$ to point $\hat{z}_c''$ to $\hat{z}_0$. The Euler angles used in these two rotations are listed in Table 4.1.

Similarly, with two *zxz*-rotations and one *z*-axis translation, we can transform from the main frame to the sub-cylinder frame as illustrated in Figure 4.7. Euler angles used in this process are listed in Table 4.2.

Above generalized extended boundary condition method developed will only solve the scattered field for one given incident field. In order to solve the T-matrix of the object, we need multiple independent incidence. Note that, the process discussed above does not require the plane wave incidence. Therefore, we can construct arbitrary incidence with any composition of spherical harmonics; and for better computational efficiency and stability, the identity matrix is used as the incidence matrix, that is, every column of the matrix is
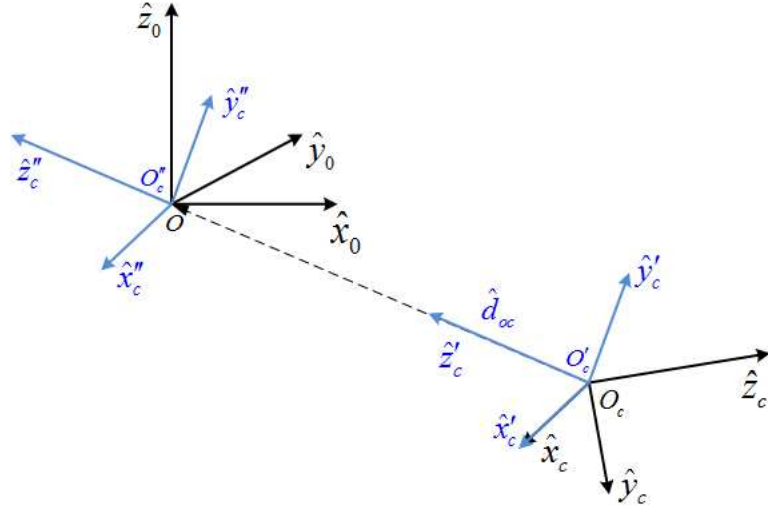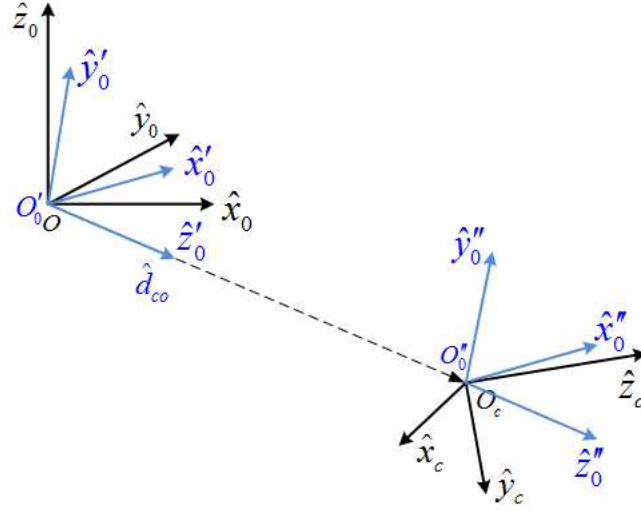
Figure 4.7: Translation from the main frame to the sub-cylinder frame

Table 4.2: EULER ANGLES FOR ROTATIONS OF THE TRANSLATION FROM THE MAIN FRAME TO THE SUB-CYLINDER FRAME.

Rotation description	α	β	γ
Rotate z_0 axis pointing to the sub-cylinder frame origin	0	θ_{co}	$\frac{\pi}{2} + \phi_{co}$
Rotate to be parallel to the sub-cylinder frame	0	$\cos^{-1}\left(\hat{z}_c \cdot \hat{d}_{co}\right)$	$\begin{array}{ll} \cos^{-1}\left(\hat{x}_0'' \cdot \hat{x}_0'''\right) & \hat{x}_0''' \cdot \hat{y}_0'' \geq 0 \\ 2\pi - \cos^{-1}\left(\hat{x}_0'' \cdot \hat{x}_0'''\right) & \hat{x}_0''' \cdot \hat{y}_0'' < 0 \end{array}$

$^*\hat{x}_0''' = \hat{z}_0'' \times \hat{z}_c$

used as the multipole expansion coefficients of the incident field.

Assuming unknown T-matrix $\bar{\bar{T}}_{total}^{cluster}$, for every incidence, there is

$$\left[\begin{array}{c} a_{sca}^{(M)} \\ a_{sca}^{(N)} \end{array} \right] = \bar{\bar{T}}_{total}^{cluster} \cdot \left[\begin{array}{c} a_{inc}^{(M)} \\ a_{inc}^{(N)} \end{array} \right] \tag{4.18}$$

Therefore, for the identity incidence matrix, the scattering solutions form a matrix $\bar{\bar{C}}_{sca}$ as

$$\bar{\bar{C}}_{sca} = \bar{\bar{T}}_{total}^{cluster} \cdot \bar{\bar{I}} \tag{4.19}$$

Hence, the T-matrix $\bar{\bar{T}}_{total}^{cluster}$ can be found as $\bar{\bar{C}}_{sca}$.

4.3.4 T-matrix to S-matrix Transformation

The efficient way of obtaining scattering matrix from transition matrix is using transformation of basis, i.e., finding the multipole expansion of plane waves and the plane wave expansion of spherical harmonics. The former one has been found in an analytical expression [26] [16]; however, the analytical form of the latter one has not been deduced. In [55], the numerical plane wave expansion of scalar spherical harmonics has been presented. Here, we expanded the vector spherical harmonics $\bar{M}$ and $\bar{N}$ numerically in terms of plane waves as

$$
\text{Rg}M_\theta^{nm} = \frac{-i j_n(k_0 r)}{N} \sum_{p,l} e^{im\frac{2\pi}{N}l} \left\{ \frac{\cos\theta_p}{2} B_{np}^{m+1} \right.
$$
$$
\left. + \frac{\cos\theta_p}{2}(n+m)(n-m+1)B_{np}^{m-1} - m\sin\theta_p B_{np}^m \right\} e^{i\bar{k}(\theta_p,\phi_l)\cdot\bar{r}} \qquad (4.20)
$$

$$
\text{Rg}M_\phi^{nm} = \frac{-j_n(k_0 r)}{2N} \sum_{p,l} e^{im\frac{2\pi}{N}l} \left\{ B_{np}^{m+1} - (n+m)(n-m+1)B_{np}^{m-1} \right\} e^{i\bar{k}(\theta_p,\phi_l)\cdot\bar{r}}
$$

$$
\text{Rg}N_\theta^{nm} = \frac{1}{N(2n+1)} \cdot \left\{ j_{n+1}(k_0 r) \sum_{p,l} e^{im\frac{2\pi}{N}l} \cdot \right.
$$
$$
\left[\frac{\cos\theta_p}{2} \left[n(n-m+1)(n-m+2)B_{n+1,p}^{m-1} - nB_{n+1,p}^{m+1} \right] \right.
$$
$$
\left. -\sin\theta_p n(n-m+1)B_{n+1,p}^m \right] e^{i\bar{k}(\theta_p,\phi_l)\cdot\bar{r}} + j_{n-1}(k_0 r)\sum_{pl} e^{im\frac{2\pi}{N}l} \cdot
$$
$$
\left[\frac{\cos\theta_p}{2} \left[(n+1)B_{n-1,p}^{m+1} - (n+1)(n+m)(n+m-1)B_{n-1,p}^{m-1} \right] \right.
$$
$$
\left. - \sin\theta_p(n+1)(n+m)B_{n-1,p}^m \right] e^{i\bar{k}(\theta_p,\phi_l)\cdot\bar{r}} \right\} \qquad (4.21)
$$

$$\text{Rg}N_\phi^{nm} = \frac{i}{2N(2n+1)} \cdot \left\{ j_{n+1}(k_0 r) \sum_{p,l} e^{im\frac{2\pi}{N}l} \cdot \right.$$

$$\left[n(n-m+1)(n-m+2)B_{n+1,p}^{m-1} + nB_{n+1,p}^{m+1} \right] e^{i\bar{k}(\theta_p,\phi_l)\cdot\bar{r}}$$

$$- j_{n-1}(k_0 r) \sum_{pl} e^{im\frac{2\pi}{N}l} \cdot \left[(n+1)(n+m)(n+m-1)B_{n-1,p}^{m-1} \right.$$

$$\left. \left. + (n+1)B_{n-1,p}^{m+1} \right] e^{i\bar{k}(\theta_p,\phi_l)\cdot\bar{r}} \right\} \tag{4.22}$$

where

$$\bar{\bar{B}} = \bar{\bar{R}}^{-1} = \left[B_{np}^m \right] = \begin{bmatrix} B_{|m|,1}^m & B_{|m|,2}^m & \cdots & B_{|m|,\bar{N}+1}^m \\ B_{|m|+1,1}^m & B_{|m|+1,2}^m & \cdots & B_{|m|+1,\bar{N}+1}^m \\ \vdots & \vdots & \ddots & \vdots \\ B_{|m|+\bar{N},1}^m & B_{|m|+\bar{N},2}^m & \cdots & B_{|m|+\bar{N},\bar{N}+1}^m \end{bmatrix} \tag{4.23}$$

and

$$\bar{\bar{R}} = \left[R_{np}^m \right] = \begin{bmatrix} R_{|m|,1}^m & R_{|m|+1,1}^m & \cdots & R_{|m|+\bar{N},1}^m \\ R_{|m|,2}^m & R_{|m|+1,2}^m & \cdots & R_{|m|+\bar{N},2}^m \\ \vdots & \vdots & \ddots & \vdots \\ R_{|m|,\bar{N}+1}^m & R_{|m|+1,\bar{N}+1}^m & \cdots & R_{|m|+\bar{N},\bar{N}+1}^m \end{bmatrix} \tag{4.24}$$

with

$$R_{np}^m = R_n^m(\theta_p) = i^n (2n+1) \frac{(n-m)!}{n+m)!} P_n^m(\cos\theta_p) \tag{4.25}$$

Since the expansion is valid based on the fact that the Bessel functions $j_n(kr) \approx 0$ when $k_0 r < \bar{N} - N_0$, where $\bar{N}$ is the truncation number in the expansion and N_0 is a small integer relaxation constant for a given range of n, m, r, the validity of the expansion is limited to near field due to a non-arbitrarily large N caused by the numerical error. To address this problem, we expand the spherical harmonics in the near-field and obtain the far-field expansions through the near-to-far field transformation by mode-matching, which replaces systematically the spherical Bessel functions in the near-field with the spherical Hankel functions in far-field. Hence, the matrix transforming the vector spherical harmonics to the far-field plane waves is constructed as $\bar{\bar{U}}$.

Note the matrix transforming the incident plane wave to spherical waves as $\bar{\bar{P}}$, which is formed using the multipole expansion coefficients of the incident plane wave and Addition theorem. The scattering matrix $\bar{\bar{S}}$ can be obtained from the T-matrix $\bar{\bar{T}}$ by

$$\bar{\bar{S}} = \bar{\bar{U}} \cdot \bar{\bar{T}} \cdot \bar{\bar{P}} \tag{4.26}$$

Validation of this transformation can be seen in Figure 4.8, where we show the comparison of the scattering patterns using the T-to-S matrix transformation and the direct computation. The far field we simulated here is for two spheres located along x-axis with two wavelength separation and 0.01 wavelength radius and dielectric constant of 3. And for this case, where the spherical harmonics up to 5th order and up to 20th order harmonics in translation are used, computational time is saved by 4 order of magnitude.
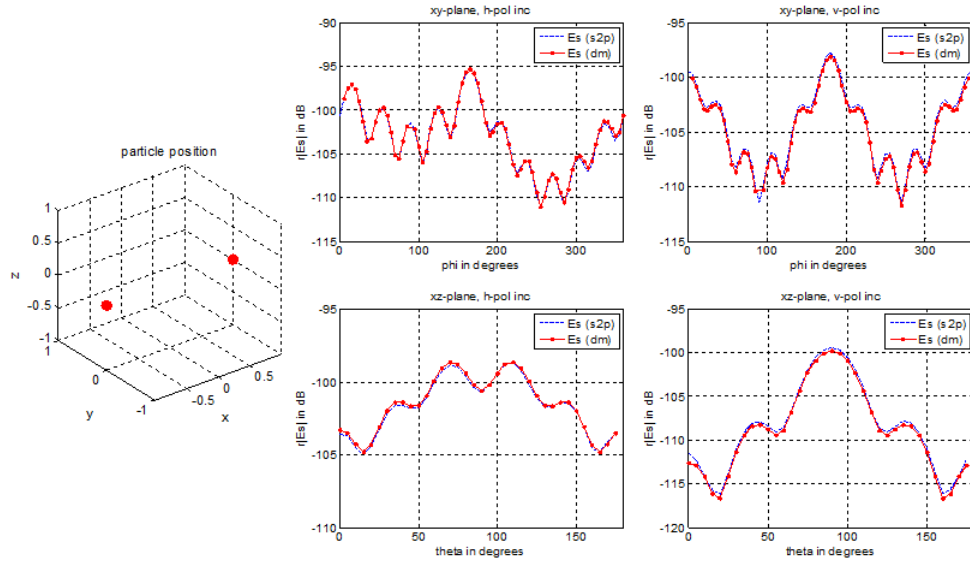
Figure 4.8: Validation of the T-to-S matrix transformation.

4.4 Experimental Validation of Scattering from Randomly Distributed Spheres and Cylinders

4.4.1 Measurement Setup

Experimental validation of our random media scattering solution has been done. The measurement setup is shown in Figure 4.9 (a). This setup is based on vector network analyzer and switching matrix with operation frequency range of 2.2 GHz to 2.8 GHz. As illustrated in Figure 4.9 (b), 14 receivers and 1 transmitter are mounted on an octagon. At every transmitter or receiver, an 'E'-shape patch antenna (Figure 4.10) is used.

After the system calibration, the switching matrix connects each receiver in turn and
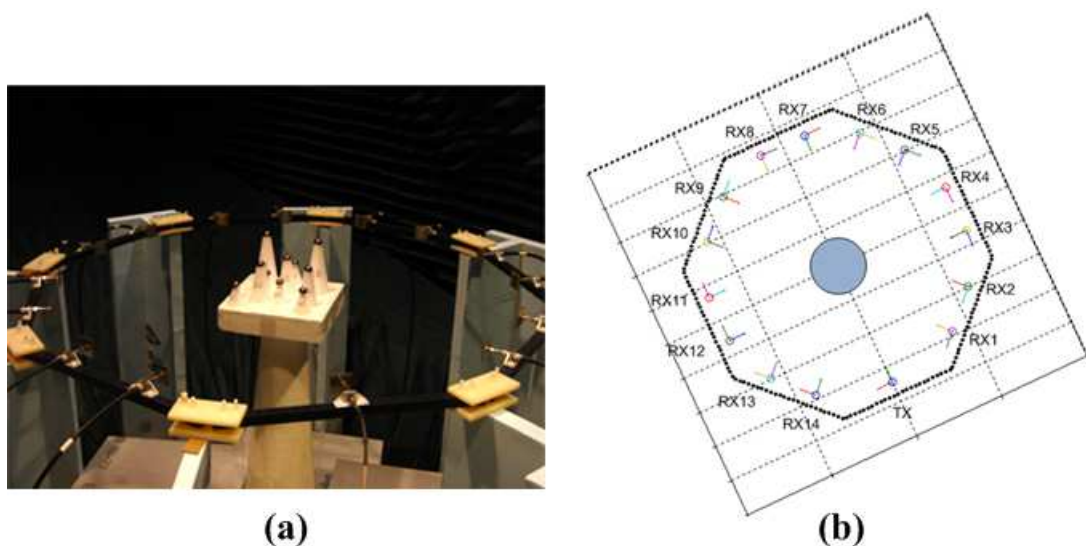
Figure 4.9: Measurement setup and top view

the transmitter to the network analyzer as a two-port network, the scattering parameters of which are measured. Therefore, sensitivity of this setup is limited by the switch isolation, which is 30 dB. By rotating the antennas, measurements are done for HH and VV polarizations.

During experiments, measurement objects are placed in the center of the octagon. Position of the object platform is well recorded. Examples of the objects can be found in figures
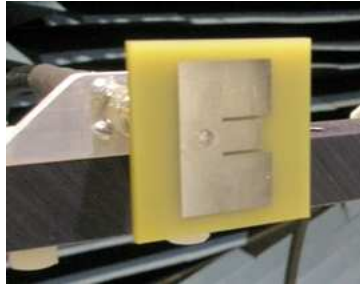
Figure 4.10: 'E'-shape patch antenna

in Section 4.4.3 and 4.4.4. Both PEC and plastic spheres are used as scatterers, as well as PEC cylinders. They are arranged 'randomly' on a grid at different heights or orientations, which are recorded as simulation inputs.

4.4.2 Simulation using Propagation Model

As mentioned above, the measured values in the experiments are scattering parameters (S-parameters), which are voltage ratios. However, the object scattering solved by the recursive T-matrix algorithm is in T-matrix. Therefore, for comparison, further processing is needed to obtain the S-parameter from the T-matrix.

As seen from the experimental setup, the transmission parameter S_{ji} between antennas
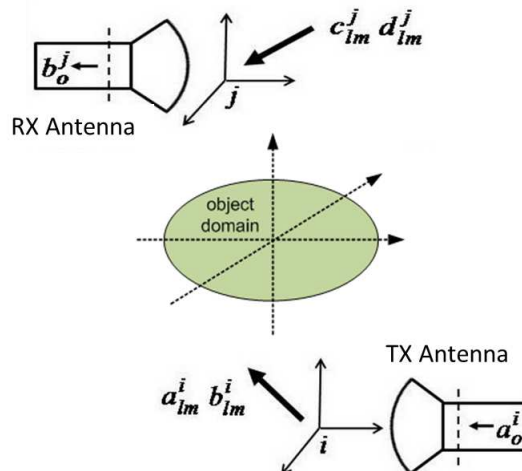
Figure 4.11: Propagation model

j and i in the presence of the object (Figure 4.11) is the one needed and can be obtained using the antenna model in [56] as

$$
S_{ji} = \begin{bmatrix} u_c^j \\ u_d^j \end{bmatrix}^T \begin{bmatrix} D_r^j & 0 \\ 0 & D_r^j \end{bmatrix} \begin{bmatrix} A_{js} & B_{js} \\ B_{js} & A_{js} \end{bmatrix} \begin{bmatrix} D_s^T & 0 \\ 0 & D_s^T \end{bmatrix}
$$
$$
\cdot T \cdot \begin{bmatrix} D_s & 0 \\ 0 & D_s \end{bmatrix} \begin{bmatrix} A_{si} & B_{si} \\ B_{si} & A_{si} \end{bmatrix} \begin{bmatrix} D_t^i & 0 \\ 0 & D_t^i \end{bmatrix}^T \begin{bmatrix} t_a^i \\ t_b^i \end{bmatrix} \tag{4.27}
$$

where the transmit coefficients t_a^i and t_b^i convert the outgoing waves a_o^i in the transmission line to the multipole expansion coefficients a_{lm}^i and b_{lm}^i of the radiated fields at the transmit antenna; and the receive coefficients u_c^j and u_d^j convert the field coefficients c_{lm}^j and d_{lm}^j at the receive antenna to the incoming waves b_o^j. The transmit and receive coefficients of the patch antennas are determined from the CAD model [56].

4.4.3   Validation Results - Spherical Scatterers

The simulation predicted S_{21} and the measured S_{21} between every receiver and the transmitter are compared over the frequency range of 2.2 GHz to 2.8 GHz. Examples of these comparisons can be seen in Figure 4.13, offering a direct and close view of the validation results at individual receivers. To overview the results at all 14 receivers, we further interpolate the measurement data over frequency and estimate deviations of the predicted values from the measured ones. Deviation in magnitude of S_{21} between one receiver and the transmitter is calculated as

$$
\sigma = \sqrt{\frac{1}{N_f} \sum_{i=1}^{N_f} \left(\frac{S_{21,i}^{sim} - S_{21,i}^{meas}}{S_{21,i}^{meas}} \right)^2} \tag{4.28}
$$

where N_f is the number of interpolation points along frequency. Phase deviation is calculated as the difference between the predicted and measured phase of S_{21}. Results at all receivers are compiled and presented below for different object setups.

Incidence Field without Objects

Before validating the predictions of scattering, we first measure S_{21} between every receiver and the transmitter in the absence of objects (i.e., incident field alone) to, on one hand, calibrate the measurements later taken with the objects, and on the other hand, validate the propagation model Eq.(4.27).

Validation results of the propagation model is shown in Figure 4.12, presenting the
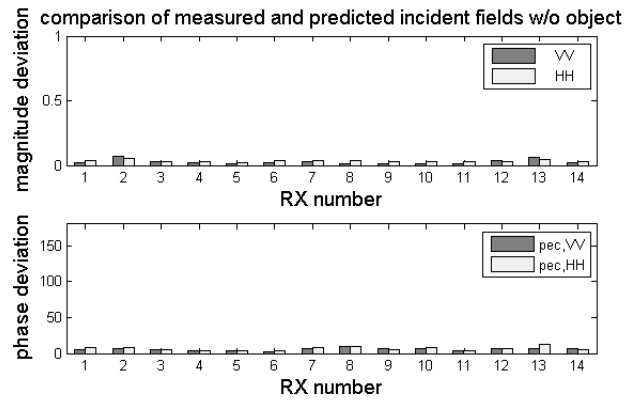
Figure 4.12: Comparison of the measured and predicted incident field

comparison between the predicted S_{21} and measured S_{21} of incident field alone. Less than 0.1 and 15° deviations can be observed in magnitude and phase respectively, indicating very good agreements between the simulation predication and the measurement.

Spherical Scatterers

For objects of spherical scatterers, PEC and plastic spheres with the same size of diameter of 2.54 cm are used. Dielectric constant of the plastic ones is ∼3.7. Locations of all spheres in the setup are recorded as one of the inputs to the simulation predicting the object scattering.

i. PEC spheres:

We start with the symmetric setup in one horizontal plane as shown in the left side

of Figure 4.14. As examples of observations at individual receivers, Figure 4.13 shows comparisons over frequency at receiver (RX) #9 and #14. Good agreement can be seen in magnitude comparisons of both S_{21}s with or without the object. Slightly larger phase deviation ($\sim 25°$) appears in the results with the object. Especially at the low frequency end at RX #14, the phase cannot be determined due to a signal level lower than the system sensitivity. This results a large deviation in phase as can be seen in Figure 4.14.

In the compiled results in Figure 4.14, average of 0.2 and 30° deviations can be seen in
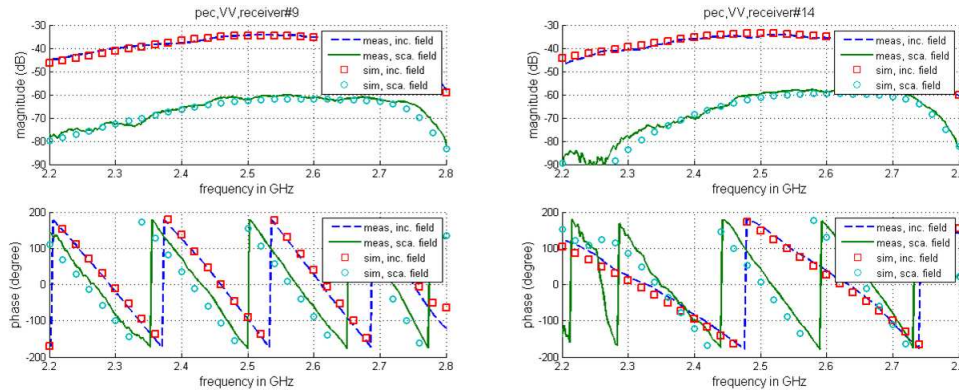
Figure 4.13: Comparison of predicted and measured S_{21} over frequency at RX#9 and RX#14 in the setup of Figure 4.14.

magnitude and phase respectively, showing the validation of the scattered field prediction. Meanwhile, large deviations can also be seen at certain receivers. There are mainly two causes: 1) a low signal level that cannot be measured accurately by the system; 2) interactions among antennas, which are not considered in the simulation.

The second setup is shown in Figure 4.15, where the spheres are randomly located in one horizontal plane (2D randomness). Results are presented in the same figure: average of 0.2 and $\sim 40°$ deviations can be seen in magnitude and phase respectively.

Then we create 3D 'randomness' as shown in Figure 4.16 and Figure 4.17 for five and ten spheres respectively. A general agreement indicates the validation of the predications.

i. Dielectric spheres:

With the same setups of above PEC spheres, we repeat the measurements using dielec-
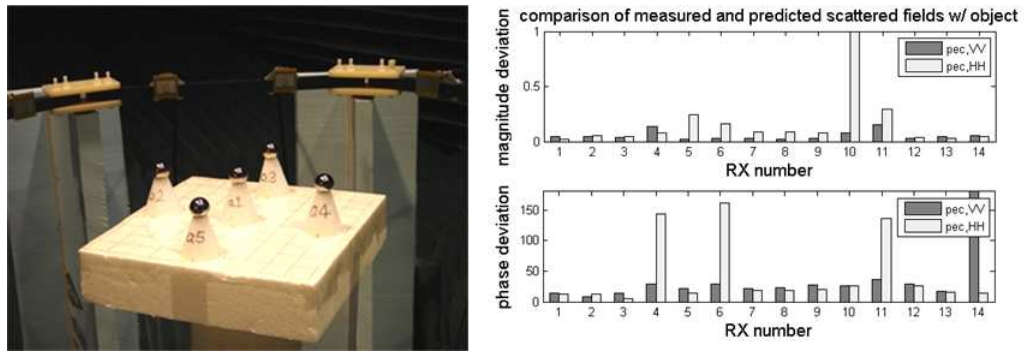
Figure 4.14: PEC spheres: deviations of the predicted S_{21} from the measured S_{21} for symmetric arrangement in a plane.
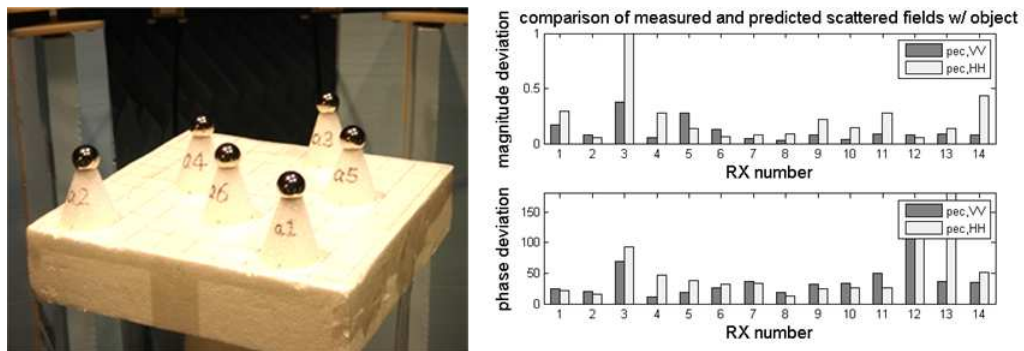
Figure 4.15: PEC spheres: deviations of the predicted S_{21} from the measured S_{21} for 2D randomness.

Figure 4.16: PEC spheres: deviations of the predicted S_{21} from the measured S_{21} for 3D randomness of 5 spheres.

tric ones. Results are shown in Figure 4.18 to Figure 4.21, from which we can tell that the transmission prediction using the recursive T-matrix method is valid for dielectric cases as well.
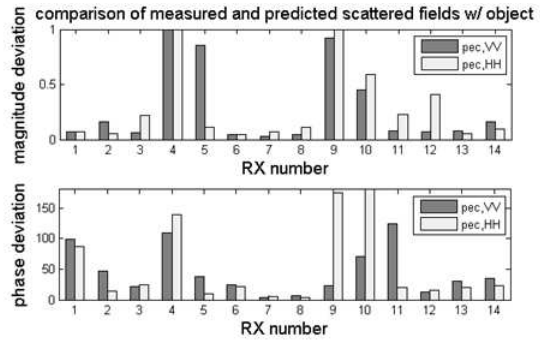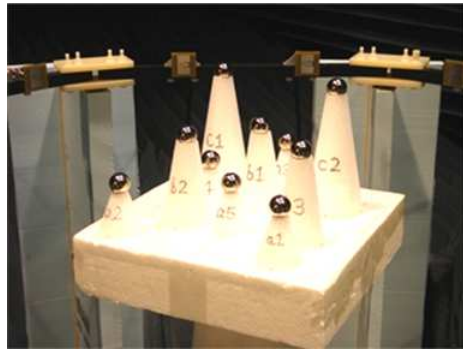
Figure 4.17: PEC spheres: deviations of the predicted S_{21} from the measured S_{21} for 3D randomness of 10 spheres
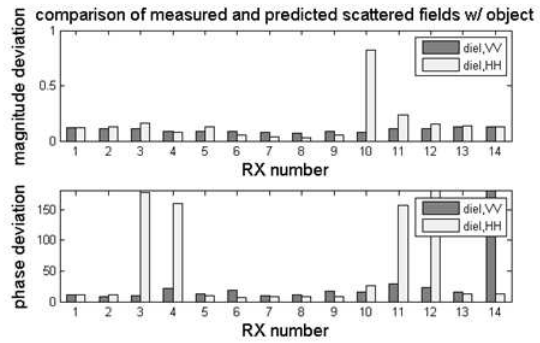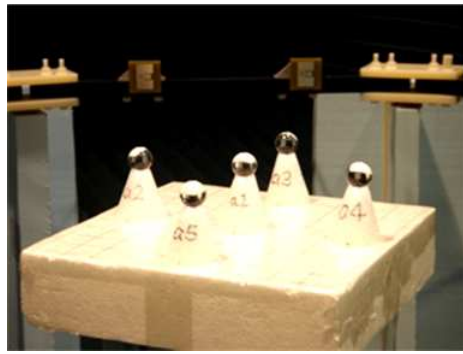
Figure 4.18: Dielectric spheres: deviations of the predicted S_{21} from the measured S_{21} for symmetric arrangement in a plane.
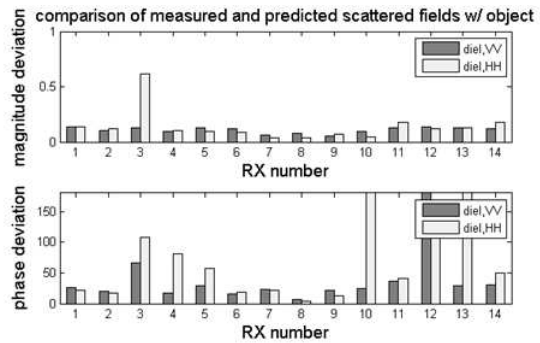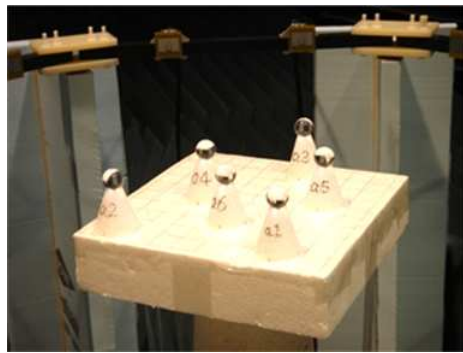
Figure 4.19: Dielectric spheres: deviations of the predicted S_{21} from the measured S_{21} for 2D randomness.

4.4.4 Validation Results - Cylindrical Scatterers

The predicted results using the recursive T-matrix method is compared with the measurements first for evaluating the improvement of the generalized iterative extended bound-

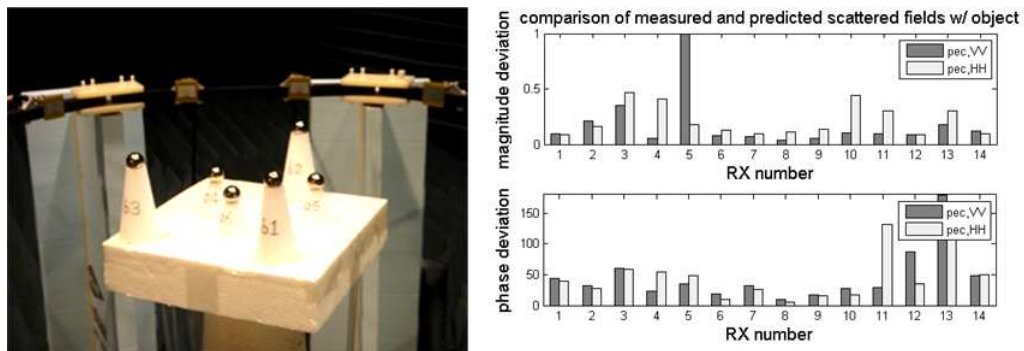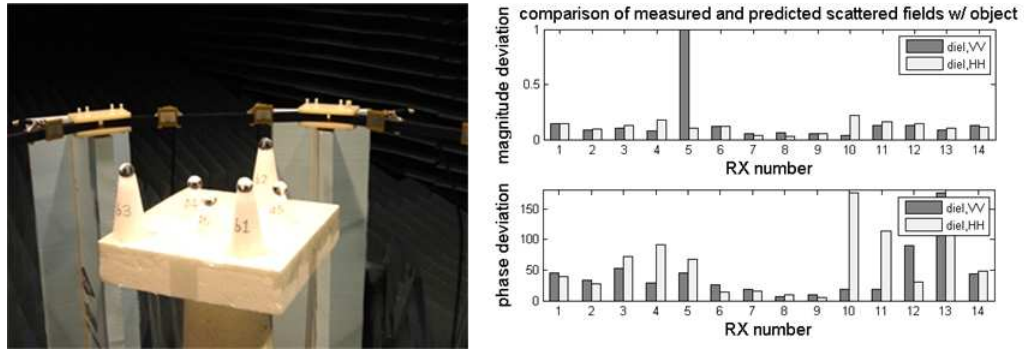Figure 4.20: Dielectric spheres: deviations of the predicted S_{21} from the measured S_{21} for 3D randomness of 5 spheres.
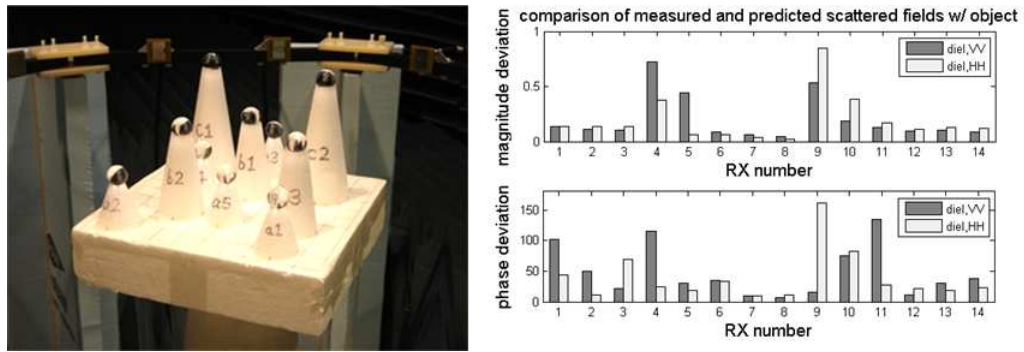
Figure 4.21: Dielectric spheres: deviations of the predicted S_{21} from the measured S_{21} for 3D randomness of 10 spheres.

ary condition method (GIEBCM). In the setup, cylinders with length of 5.08 cm and 7.62 cm are used. Diameters of all cylinders are 2.06 cm (13/16 inch). Center location and the orientation angle of every cylinder are recorded.

Validation result is presented in Figure 4.22 for the setup shown in the same figure. Comparison in magnitude indicates general agreement between the predicted and measured fields, however, larger deviation appears in the phase comparison. There are several explanations for this: in the aspect of simulation, T-matrix of a single cylinder can be less accurate due to larger length-to-diameter ratio, also, the number of modes used in the recursive T-matrix method may be inadequate since the scatterer is bigger; meanwhile, in the aspect of the measurement, bigger error can exist in recording locations and orientations of the cylinders.
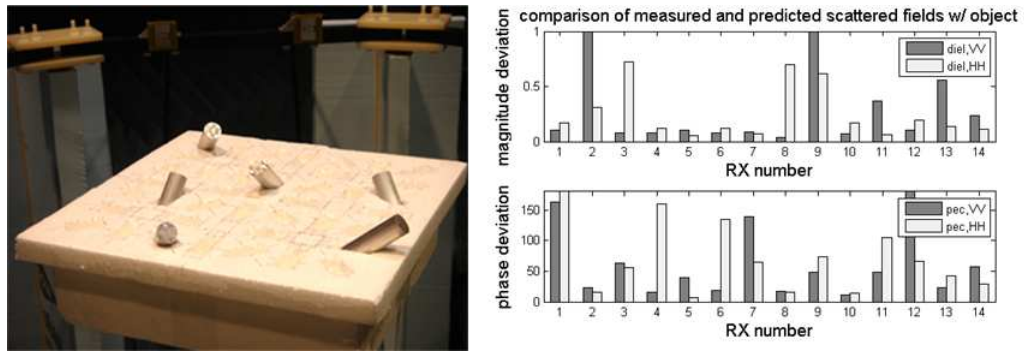
Figure 4.22: PEC cylinders (diameter: 2.06 cm): deviations of the predicted S_{21} from the measured S_{21} using the recursive T-matrix method

For the same setup, the results the generalized iterative extended boundary condition method (GIEBCM) is shown in Figure 4.23, where a better agreement can be seen, especially in phase.
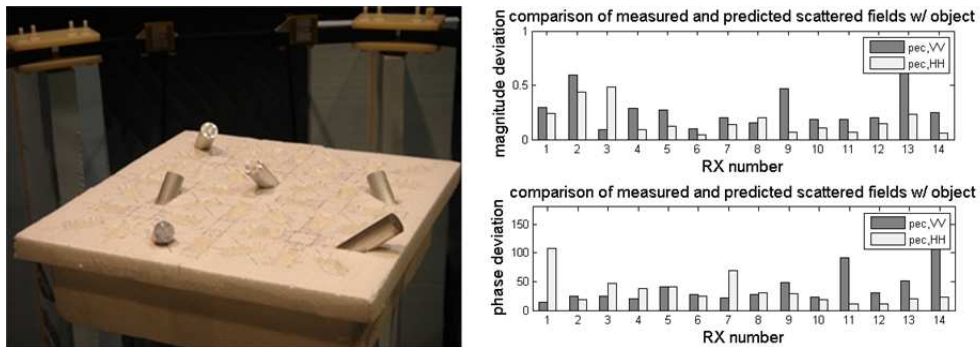
Figure 4.23: PEC cylinders (diameter: 2.06 cm): deviations of the predicted S_{21} from the measured S_{21} using the GIEBCM

Besides, several setups of PEC cylinders of varied diameters are measured and compared with the simulation predictions.

The thinnest cylinders used have diameter of 0.95 cm (3/8 inches), with lengths of 5.08 cm or 7.62 cm. The comparisons started with the simplest setup of a single cylinder as shown in Figure 4.24. Then, more cylinders are added to the setup as shown in Figure 4.25 to Figure 4.27. Results show good agreements in general, especially in phase comparisons.
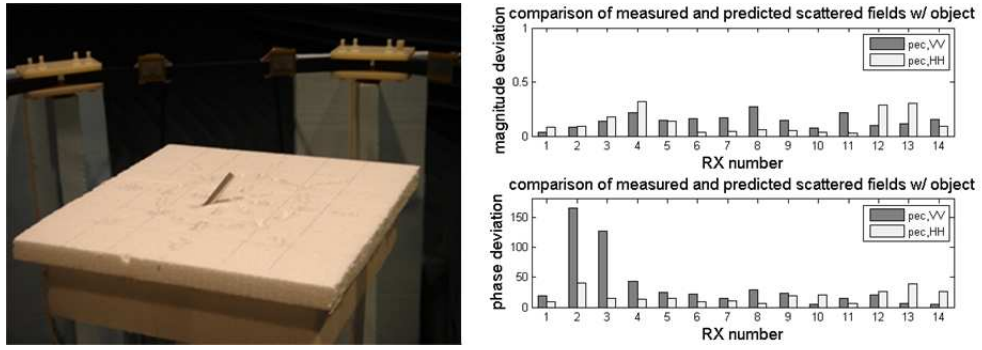
Figure 4.24: PEC cylinders (diameter: 0.95 cm), case 1: deviations of the predicted S_{21} from the measured S_{21} using the GIEBCM.
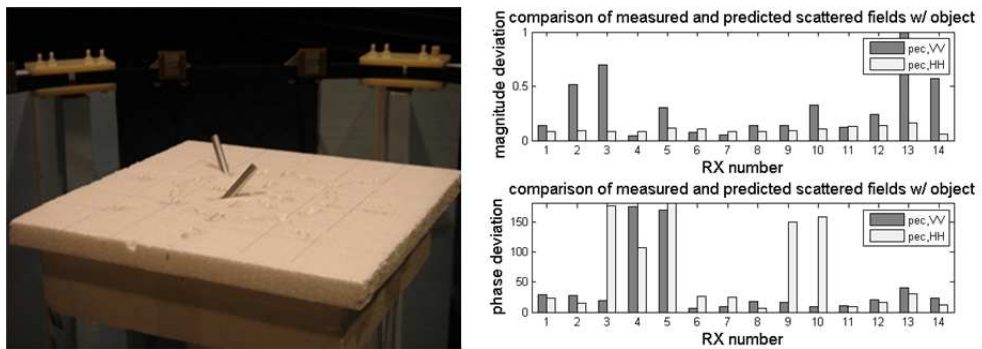
Figure 4.25: PEC cylinders (diameter: 0.95 cm), case 2: deviations of the predicted S_{21} from the measured S_{21} using the GIEBCM.
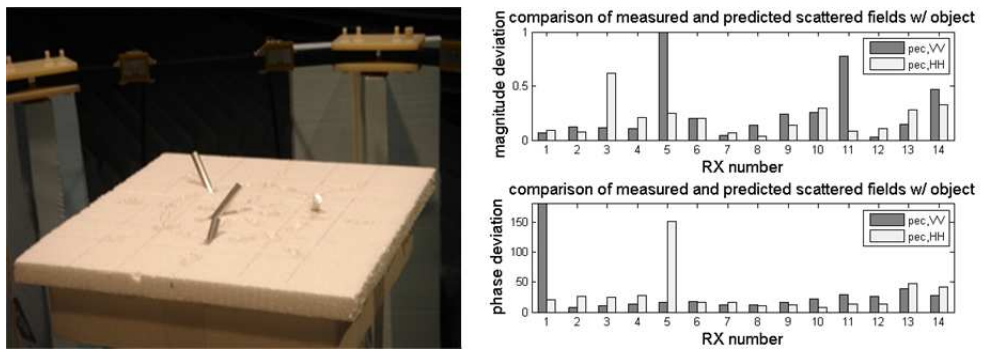
Figure 4.26: PEC cylinders (diameter: 0.95 cm), case 3: deviations of the predicted S_{21} from the measured S_{21} using the GIEBCM.

Similar comparisons are done for cylinders with diameter of 1.59 cm (5/8 inch) as shown in Figure 4.28 to Figure 4.30. As more cylinders are added into the setup, deviations of the predications from the measurements increase, however, validation of the predications

can still be seen.
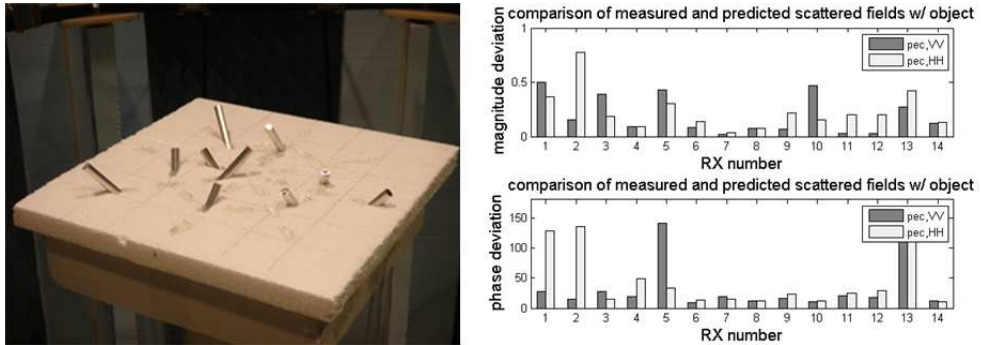
Figure 4.27: PEC cylinders (diameter: 0.95 cm), case 4: deviations of the predicted S_{21} from the measured S_{21} using the GIEBCM.
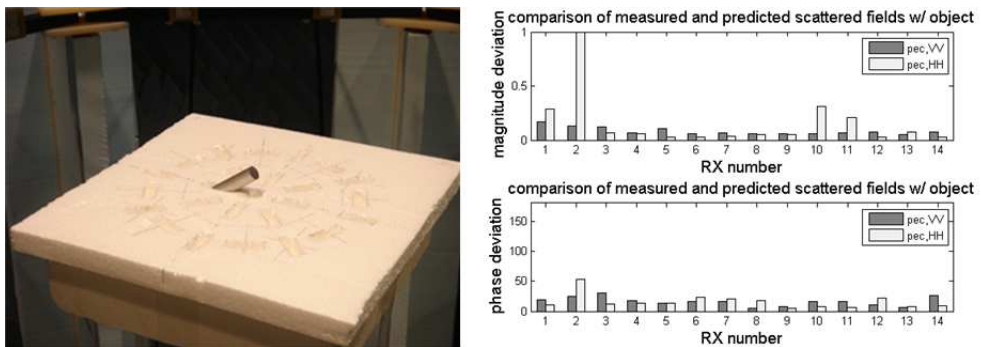
Figure 4.28: PEC cylinders (diameter: 1.59 cm), case 1: deviations of the predicted S_{21} from the measured S_{21} using the GIEBCM.
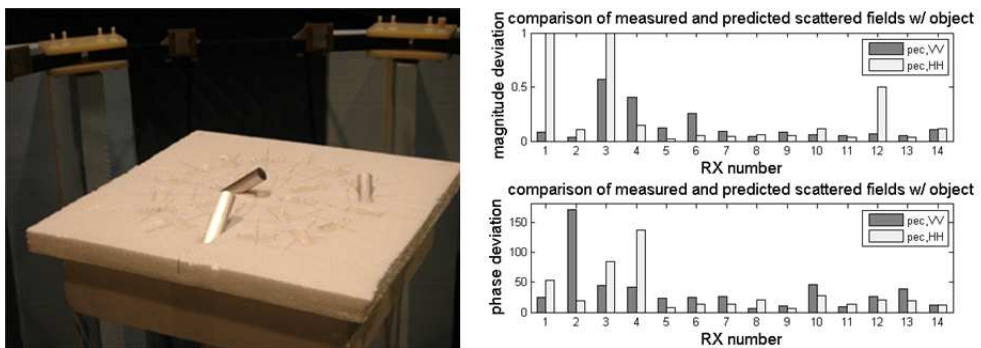
Figure 4.29: PEC cylinders (diameter: 1.59 cm), case 2: deviations of the predicted S_{21} from the measured S_{21} using the GIEBCM.
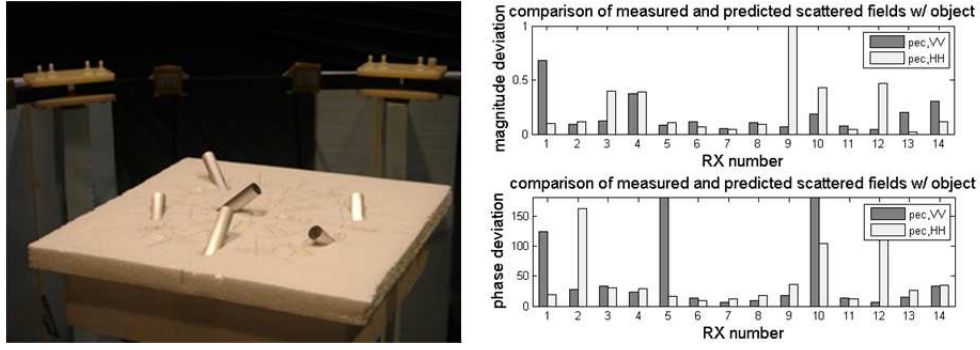
Figure 4.30: PEC cylinders (diameter: 1.59 cm), case 3: deviations of the predicted S_{21} from the measured S_{21} using the GIEBCM.

4.5 Results of Scattering from Random Media in Multi-layer Rough Surfaces

Scattering from the buried inhomogeneities is combined with the scattering from rough surfaces. Here we show the results of scattering from single rough surface with different buried media.

Figure 4.31 illustrates the geometry of a single rough surface with random distributed spherical scatterers underneath. The simulation parameters for this case is in Table 4.3, where h and l_c are the rms height and correlation length of the surface respectively. The volumetric fraction of the media is 5%, with spherical scatterers of radius a and dielectric constant ε_s. ε_{bg} is the background dielectric constant of the media, and d_{sep} denotes the separation between the surface mean and the upper boundary of the media region.

Simulation results of this case is shown in Figure 4.31, where the scattering from the

Table 4.3: SIMULATION PARAMETERS FOR SINGLE ROUGH SURFACE WITH BURIED SPHERICAL RANDOM MEDIA (Figure 4.31).

frequency	$k_0 h$	l_c/h	f_v	media region	a	ε_s	ε_{bg}	d_{sep}
435MHz	0.046	10	5%	$8\lambda \times 8\lambda \times \lambda$	0.08λ	10	$6.17 + i0.95$	0.03λ

surface alone is plotted for comparison. Enhancement can be seen in all scattered field components, especially in the cross-pol component.
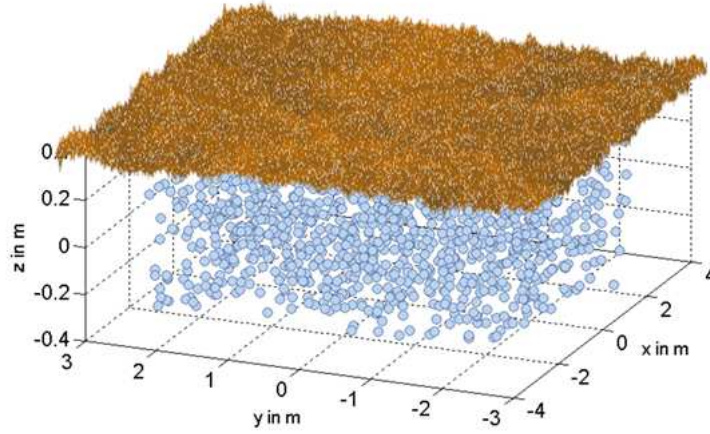
Figure 4.31: Scattering from single rough surface with buried spherical random media.

Table 4.4: SIMULATION PARAMETERS FOR SINGLE ROUGH SURFACE WITH BURIED CYLINDRICAL RANDOM MEDIA (Figure 4.33).

frequency	k_0h	l_c/h	f_v	media region	a	L	ε_{cyl}	ε_{bg}	d_{sep}
435MHz	0.046	10	5%	$8\lambda \times 8\lambda \times \lambda$	0.1λ	0.4λ	15	$6.17 + i0.95$	0.03λ

Keeping the rough surface on top, we change the media to randomly distributed short cylinders. The orientations of the cylindrical scatterers are shown in Figure 4.33, where we only present the media part.

Table 4.4 lists the simulation parameters for this geometry. The surface statistics are the same as the previous case; and the random media keeps the same volumetric fraction. The cylinders have radius a of 0.1λ and length L of 0.4λ. Contrast of the media to the background is enhanced by increasing the dielectric constant of the scatterers to be 15.

Simulation results are shown in Figure 4.34. More enhancement can be seen than the spherical media, likely due to the larger contrast.

Besides the random media simulated above, the simple root model is constructed as presented in section 4.3.1. The orientations of the sub-cylinders are shown in Figure 4.35. This structure replaces the above random media as the buried inhomogeneities underneath the surface for simulation.

The root structure parameters are shown in Table 4.5, the meanings of which are illus-

99
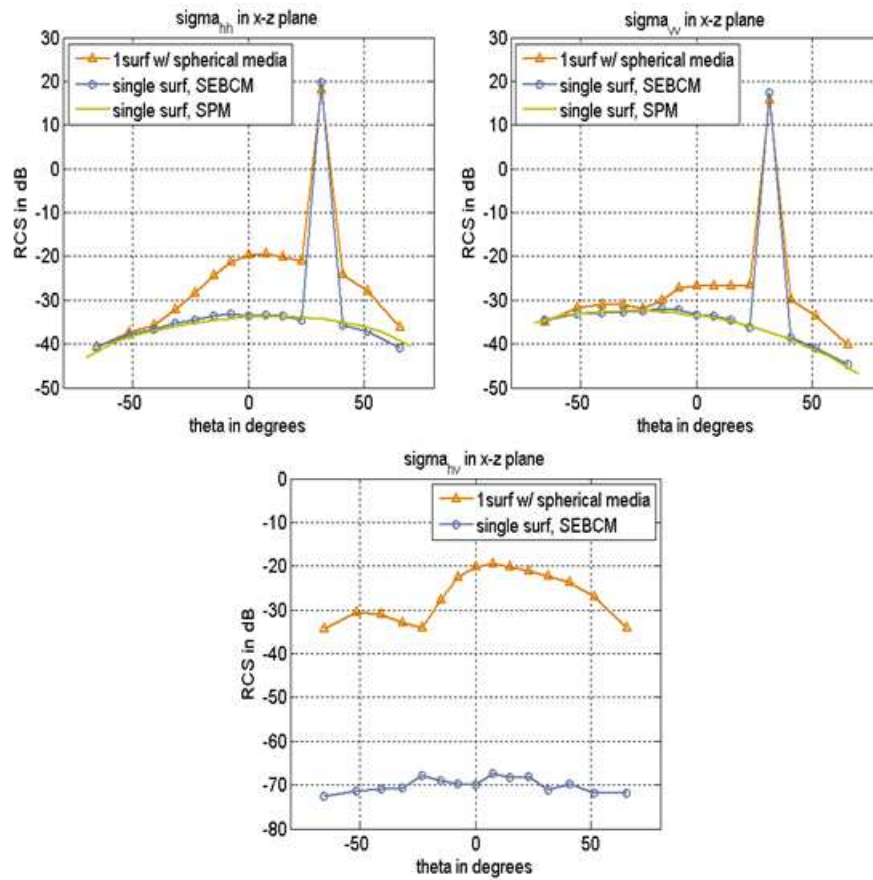
Figure 4.32: Results of scattering from single rough surface with buried spherical random media (Figure 4.31).
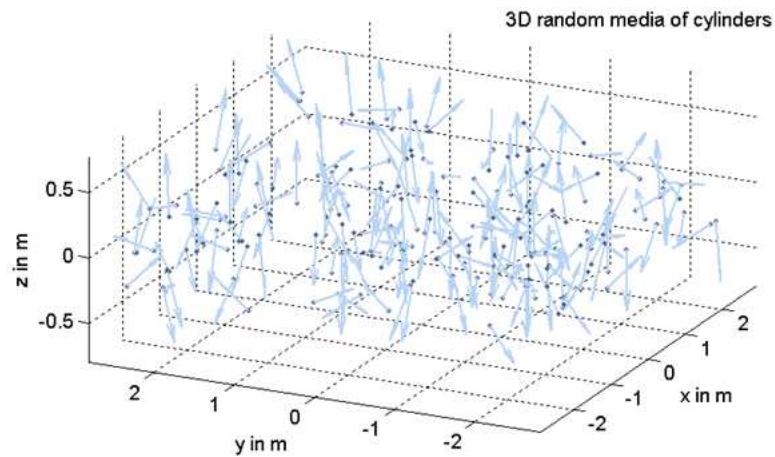
Figure 4.33: Scattering from single rough surface with buried cylindrical random media.

Table 4.5: SIMULATION PARAMETERS FOR SINGLE ROUGH SURFACE WITH BURIED SINGLE ROOT-LIKE CLUSTER (Figure 4.35).

frequency	$k_0 h$	l_c/h	ε_{bg}	d_{sep}
435MHz	0.046	10	$6.17 + i0.95$	0.03λ

root area	#root	root distr.	subcyl.info	
$R_r = 0.73\lambda$	$N_\phi = 6$	$d_t = 0.43\lambda$	$r_r = 0.045\lambda, L = 0.09\lambda$	
$d_r = 0.725\lambda$	$N_\theta = 2$	$r_t = 0.29\lambda$	$\varepsilon_{root} = 15$	
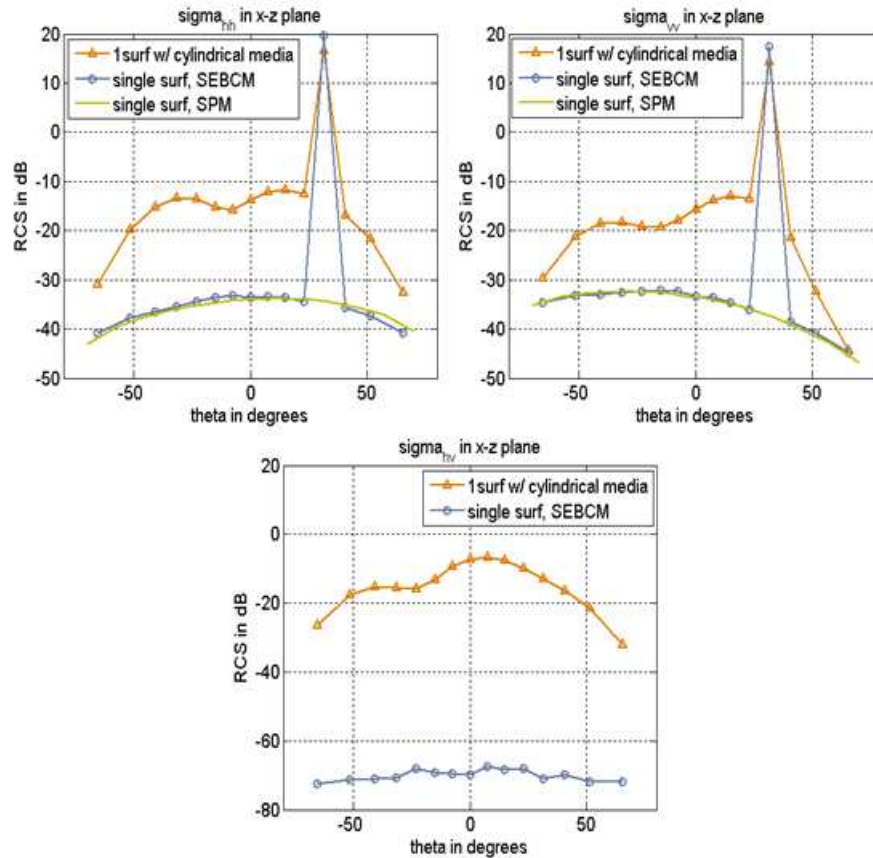
Figure 4.34: Results of scattering from single rough surface with buried cylindrical random media (Figure 4.33).

trated in Figure 4.4. With the same rough surface on top, the scattering is computed and shown in Figure 4.36. As can be seen from the comparisons, there is little change in the copol results. The enhancement in cross-pol result is much more observable.

To involve more root structures under the top surface, we arrange the root clusters
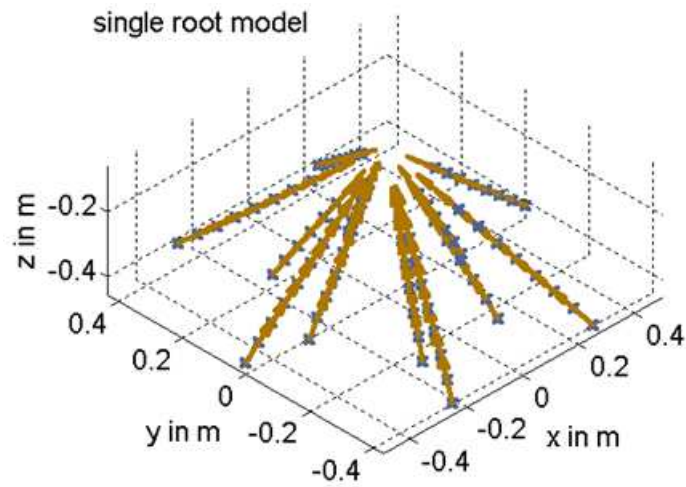
Figure 4.35: Scattering from single rough surface with single root-like cluster.
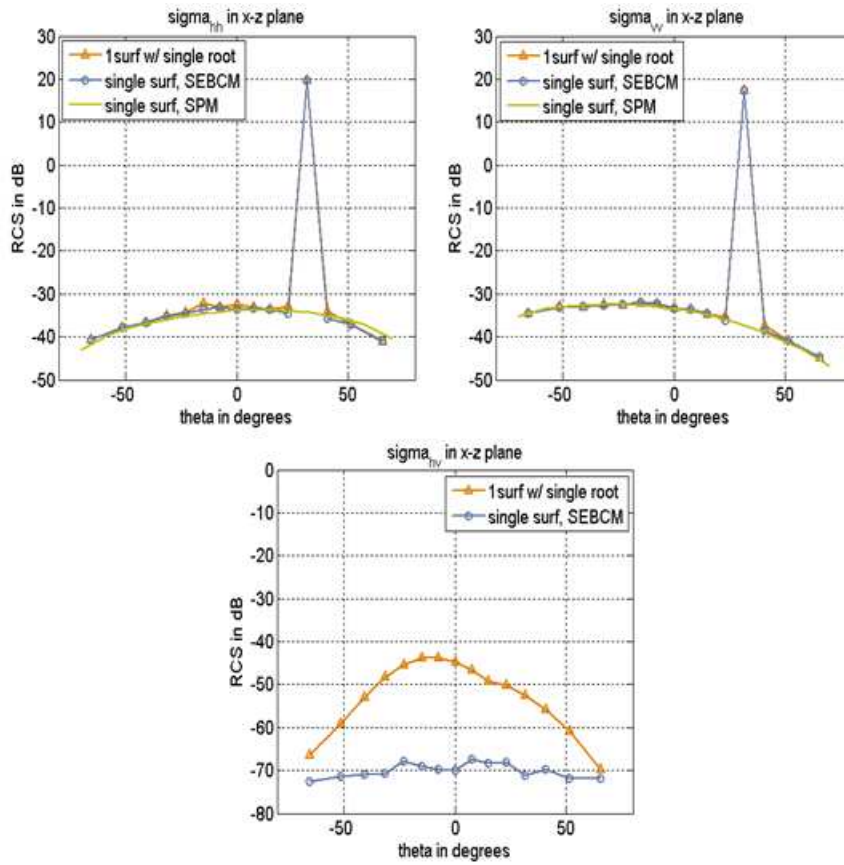
Figure 4.36: Results of scattering from single rough surface with single root-like cluster (Figure 4.35).
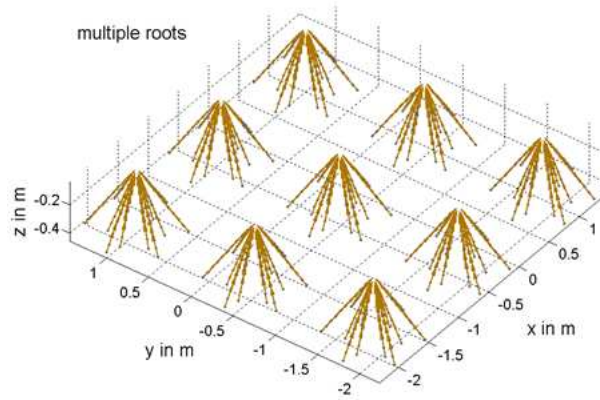
Figure 4.37: Scattering from single rough surface with multiple root-like cluster.

horizontally with separation d_{mg} of 0.06λ as shown in Figure 4.37. The parameters of the root cluster is same as in above single root case. All parameters can be found in Table 4.6.

Table 4.6: SIMULATION PARAMETERS FOR SINGLE ROUGH SURFACE WITH BURIED MULTIPLE ROOT-LIKE CLUSTER (Figure 4.37).

frequency	$k_0 h$	l_c/h	ε_{bg}	d_{sep}
435MHz	0.046	10	$6.17 + i0.95$	0.03λ

root area	#root	root distr.	subcyl.info
$R_r = 0.73\lambda$	$N_\phi = 6$	$d_t = 0.43\lambda$	$r_r = 0.045\lambda, L = 0.09\lambda$
$d_r = 0.73\lambda, d_{mg} = 0.06\lambda$	$N_\theta = 2$	$r_t = 0.29\lambda$	$\varepsilon_{root} = 15$

Simulation results shown in Figure 4.37 indicate larger change in co-pol and cross-pol components. A scattering pattern of the periodic arrangement of the root structure can be seen from the cross-pol plot.

In above simulations involving single rough surface, the results are valid if the surface is located outside the external sphere of the random media, since the scattering matrix of the random media (which is computed from its transition matrix) is only valid outside its external sphere. This sphere can be extremely large depending on the location of the coordinate origin. Therefore, the surface can be very close to the top of the random media. The result validity region will be studied in the future work.

103
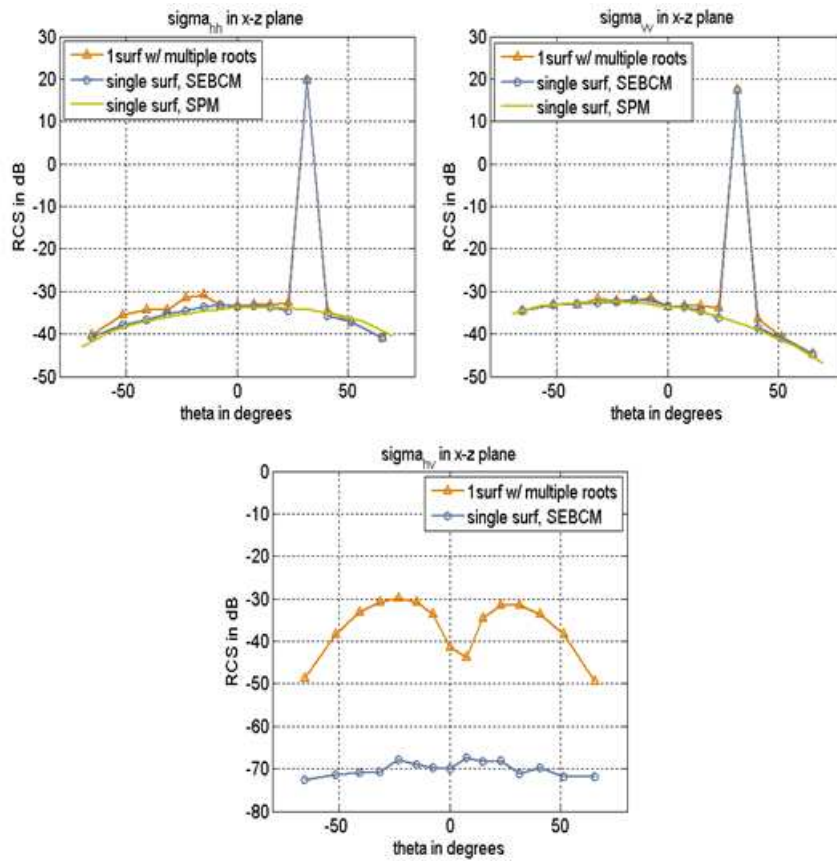
Figure 4.38: Results of scattering from single rough surface with multiple root-like cluster (Figure 4.37).
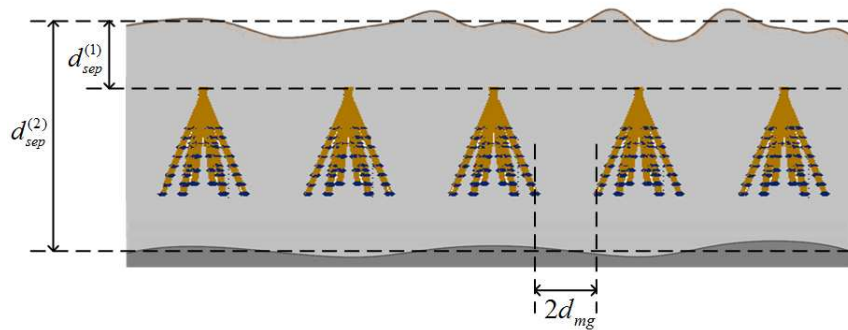
Figure 4.39: Illustration of the cross section of the two rough surface with buried root-like clusters

For the case of two rough surfaces with buried roots in the middle, where both rough surfaces need to be outside the external sphere of the multiple roots while maintaining

Table 4.7: SIMULATION PARAMETERS FOR TWO ROUGH SURFACES WITH BURIED ROOT-LIKE CLUSTER (Figure 4.39).

frequency	$h_1 = h_2$	$l_{c1} = l_{c2}$	ε_1	ε_2	$d_{sep}^{(1)}$	$d_{sep}^{(2)}$
435MHz	0.02λ	0.5λ	$5.4 + i0.44$	$11.27 + i$	0.06 m	0.414 m

| root area		#root	root distr.	subcyl.info
$R_r = 0.2$ m		$N_\phi = 6$	$d_t = 0.15$ m	$r_r = 0.016$ m, $L = 0.032$ m
$d_r = 0.2$ m, $d_{mg} = 0.2$ m		$N_\theta = 2$	$r_t = 0.1$ m	$\varepsilon_{root} = 15$

reasonable layer separations, superposition of single-root scattering matrices with phase corrections of the incident and scattered fields can be used. Here we simulated one case that is illustrated in Figure 4.39.

The root has similar pattern as the one in the previous case but with smaller dimensions, so that the external sphere of each root will not be overlapped with either the neighbor ones or the rough surfaces above and below the roots. The detailed parameters can be found in Table 4.7.

Results of scattering from the two rough surfaces without the roots, with one single root, and with multiple roots are simulated and compared. As shown in the copol results in Figure 4.40, existence of multiple roots between the two rough surfaces enhances largely the scattering in the backward directions, while the existence of a single root does little change to the scattering pattern. Enhancement due to the existence of both the single and multiple root(s) can be observed in the crosspol results.

4.6 Summary and Conclusion

In this chapter, a solution to three-dimensional electromagnetic scattering from rough surfaces with buried inhomogeneous media is developed and presented using scattering matrix approach. The scattering of the inhomogeneities is solved using the recursive T-matrix method for spherical and short-cylindrical scatterers, and generalized iterative extended boundary condition method (GIEBCM) for long or root-like cylinder clusters. The scat-
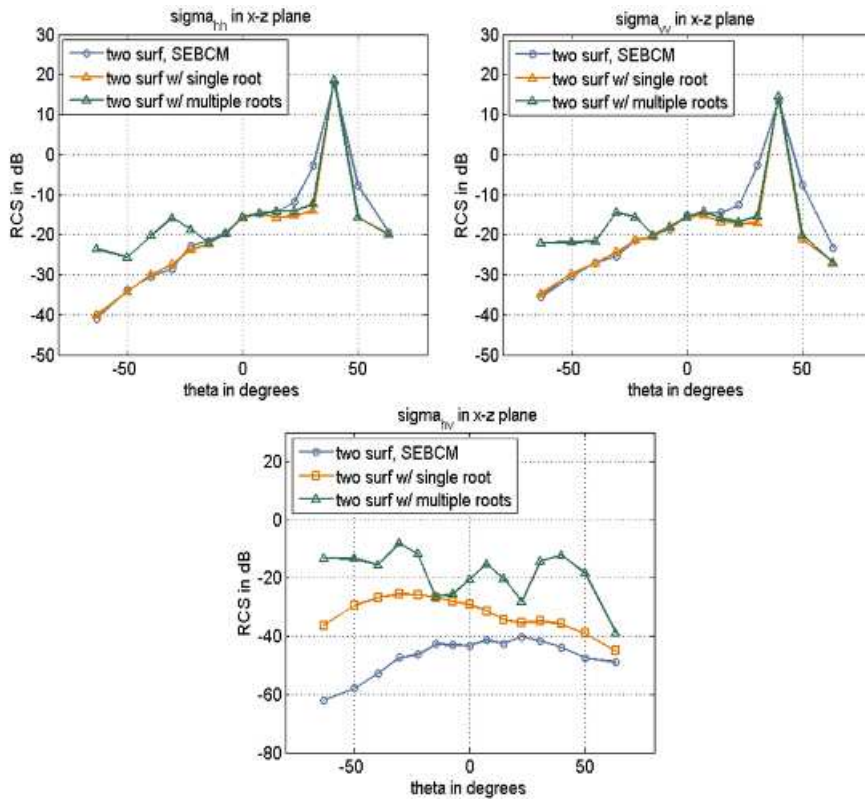
Figure 4.40: Results of the scattering cross section of the two rough surface with buried root-like clusters

tering solution obtained in T-matrix format is further transformed to scattering matrix for solving the layered problem. Both GIEBCM and the transformation from T-matrix to S-matrix are the contribution of this dissertation. The scattering matrix of the rough surface is found using the stabilized extend boundary condition method (SEBCM). This methodology has high computational efficiency and takes account of all interactions among the media and layers. The solution of the scattering from the inhomogeneities is validated experimentally. Results of the combinations of scattering from the rough surface and random media or root structures are shown in this chapter.

This is the first time that the volumetric scattering of the buried random media is considered in the 3D scattering from the ground; particularly, the vegetation roots are taken into account. As can be seen from the results, these inhomogeneities will have impacts on all scattering components, especially cross-pol components, depending on their contrast and

volumetric fraction. Further verification of the scattering from the combination of rough surfaces with random media will be done as our future work. The model constructed in this chapter can be used for study of the role of vegetation roots in the root-zone soil moisture retrieval.

CHAPTER 5

Investigation of Soil Moisture Dynamics with a Tower-Mounted Radar

This chapter describes an experimental tower-based multiple-low-frequency radar system and its applications in field measurements of soil moisture. This system is intended for surface, subsurface/root-zone, and subcanopy soil moisture detection, and may also be suitable for measurements of depth of fresh water from low altitudes. Its unique features are compact, remotely-controlled design and high output power. The sensitivity of this radar is further enhanced by forming a vertical synthetic aperture. Field measurements using this radar have been done in several locations. We will describe one of the main field experiments in this chapter - observation of the corn field over its growing season in Gainesville, FL. The results show the sensitivity of radar to soil moisture (even in the presence of vegetation) and roughness. Signal signature changes of the crop growth are also observed.

5.1   Introduction

Previous chapters covered the theoretical modeling of electromagnetic scattering from the ground surface and subsurface with or without buried inhomogeneities for soil moisture sensing. The utility of this model can be demonstrated by performing actual radar measure-

ments for soil moisture detection. Therefore, a new experimental multiple-low-frequency radar system is designed and built in this work, with which several field measurements have been carried out. As with any major hardware development, parts of this effort benefited from the collaboration of other group members.

Radar systems for soil moisture detection have been designed for spaceborne and airborne platforms, such as the Soil Moisture and Ocean Salinity (SMOS) mission [3] [4], RADARSAT-2 [5], the upcoming Soil Moisture Active and Passive (SMAP) [9] mission, and Airborne Microwave Observatory of Subcanopy and Subsurface (AirMOSS) mission. Comparing to these orbital or high-altitude systems, near-ground radar systems operating at lower altitudes are less expensive, less complex, and flexible to deploy. Hence, they could offer an attractive option for small area measurements and experiments. The Microwave Observatory of Subcanopy and Subsurface (MOSS) tower radar is a good example of such systems [8].

The MOSS radar system is a pulsed polarimetric radar. It was designed for subsurface soil moisture measurements operating at VHF, UHF, and L-band using a log-periodic antenna. Our new tower-mounted radar is based on the concept and preliminary design of the MOSS radar, with many key changes to improve performance:

- **Compact Design:** With a bistatic system design, internal RF source, and efficient mechanical structure, the entire system is confined within only dimensions of $30 \times 30 \times 60$ cm. This enhances the system reliability (especially during deployment and transportation), and allows it to be a stand-alone system mounted on the tower-top without the need to use very long RF and digital cables.

- **Higher Output Power:** By having a stand-alone system on the tower-top, signal power loss in the transmission between tower-top and ground modules is avoided. With a high gain power amplifier, the radar output power is enhanced to 2 watts (much more than twice of the MOSS radar). This increases the radar sensitivity to the ground return signal.

109

- **Auxiliary Capability:** Additional microcontroller and analog-to-digital converters (ADC) allow antenna position control, multi-spot temperature monitoring, and cooling/heating module operation. This largely simplifies the radar operation procedure, and extends the radar operating conditions. The radar status can be monitored under hot/cold environments to avoid potential damage.

- **Ease of Operation:** Wireless control of radar and antenna position from a laptop located on the ground improves the radar operational efficiency.

This system is tested and used in several field measurements such as surface and subsurface measurements at the Matthaei Botanical Gardens (Ann Arbor, MI), the seasonal soil moisture measurement at the Institute of Food and Agricultural Sciences (IFAS) (Gainesville, FL), as well as the subcanopy soil moisture detection at the University of Michigan Biological Station (Pellston, MI). In this chapter, the application of this radar at the IFAS of the University of Florida is mainly described, and its primary results are presented. As shown from the measurements, good radar stability and sensitivity to soil moisture and surface roughness are observed. The measurements of calibration targets (corner reflectors) of different sizes indicate the accuracy of differential measurements. For model validation, a ground structure consisting of a single rough surface with a dielectric profile using ground collected data has been simulated. The comparison with the radar measurements show the same trend of change in the measurement as the model predicted, however, an overestimation can be seen in the backscattering cross section from the radar measurements. This bias primarily points to the need for a more accurate near-field target calibration method and a near-ground scattering model, which will be addressed in future work.

5.2   System Design

This newly designed and built tower-based radar system covers three frequency bands: L-band (1000 MHz), P-band (430 MHz), and VHF (137 MHz). As shown in the system diagram (Figure 5.1), this is a PC-based, FPGA-controlled pulsed radar system. During ev-
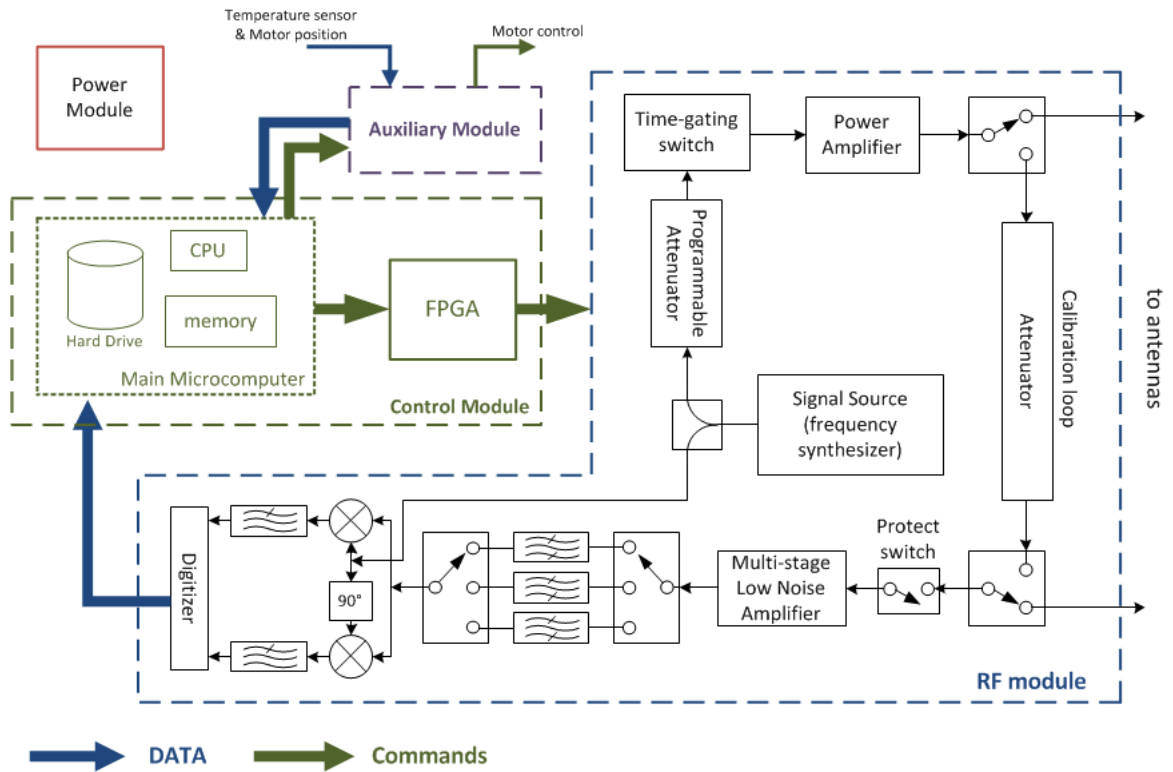
Figure 5.1: Radar system diagram

ery measurement, the radar sends a pulsed continuous wave (CW) signal toward the object and receives the scattered signal from it. The bandwidth of the radar at each center frequency is determined by the time-domain pulse width, typically around 50 ns ($\sim$ 20 MHz bandwidth).

The radar electronics are designed for a bi-static system but can be adapted to operate as a mono-static system. This radar system has four subsystems: control module, radio frequency (RF) module, auxiliary module, and power module.

The control module consists of a main microcomputer (including CPU, motherboard, memory, and hard drive), a field-programmable gate array (FPGA) sub-module, and a wireless network sub-module. The microcomputer runs a Windows operating system, allowing user remote access through the wireless connection. According to user's request, the microcomputer sends commands to the FPGA sub-module for execution. The FPGA sub-module has direct connections to all control wires and programming interfaces of switches
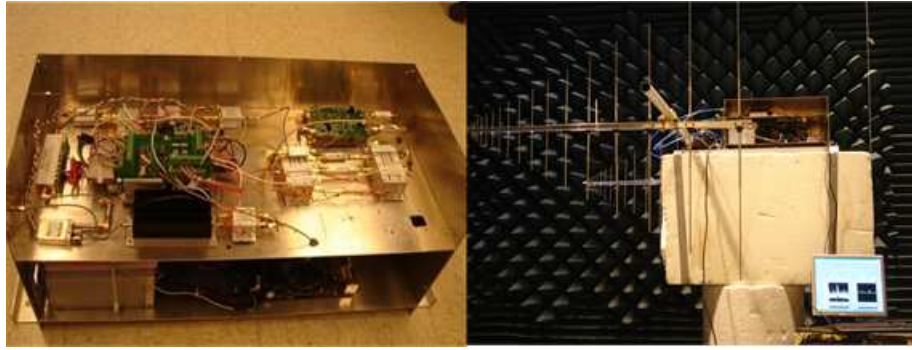
Figure 5.2: Radar system

and programmable sub-modules within the RF module. It interprets the commands from the microcomputer to control the logic signals and activates them with appropriate timing.

The RF module comprises the radio-frequency signal source, transmit chain, antennas, calibration loop, and receive chain RF electronics. The signal source is a frequency synthesizer with programming interface. It produces the CW signal at a programmed frequency covering from 100 MHz to 1.5 GHz. An external RF source can be used as well. Signal from the source goes through a coupler. One portion of the signal continues to the transmit chain, and the other portion acts as the local oscillator (LO) input to the in-phase/quadrature (I/Q)-demodulator in the receive chain. The signal continuing in the transmit chain passes a programmable attenuator and a switch that time-gates this CW signal to a pulse with a width of tens of nanoseconds. Width and timing of this pulse are programmable and controlled by the FPGA. The pulsed CW is amplified by a power amplifier. This signal goes either to the transmit antenna for radiation or to the calibration loop bypassing the antennas for internal calibration.

The signal collected from the object or the calibration signal is the input to the receive chain. The first stage of the receive chain is a low-loss protect switch. It turns on the receive path right before the expected arrival time of the return signal to protect the receive chain from the interference caused by the antenna cross-coupling and/or resonance. Received signal is amplified by a multiple-stage low-noise amplifier (LNA) and cleaned by the corresponding band-pass filter in the switchable filter bank. Then this signal is demodulated

to a baseband signal by an I/Q demodulator. The I/Q demodulator is a type of frequency down-converter mixing its input signal with the LO signal (coupled from the signal source in this system) and the 90-degree phase shifted LO signal to have both the real and the imaginary parts of the down-converted signal. Outputs from the I/Q demodulator are digitized by a fast sampling two-channel analog-to-digital converter (ADC) controlled by the main microcomputer and recorded to the hard drive. Traditionally, the digitizer is part of the digital subsystem, but for simplicity, I keep it under RF module.

Auxiliary module of this radar system has functions of temperature monitoring and antenna position control. It is based on a microcomputer with multiple ADCs and digital inputs/outputs (IOs). It reads voltage signals from temperature sensors through ADCs. The digital IOs switch the high-current relays for motor control of the antenna. This module communicates directly with the main microcomputer.

The power module of the radar transforms AC to DC and provides all voltages needed in the system through regulators.

The radar control software (using LabVIEW) runs on the main microcomputer. It builds the user interface for measurement control, data display, and radar status indication. For measurement control, it allows the user to switch between the calibration and measurement modes respectively, and to define pulse width, pulse timing, attenuation in transmit chain and calibration loop, receive chain switch-on timing, number of samples to average, parameters of the digitizer, and the data storage path. The software displays the on-site calibration and measurement results, and indicates the internal temperature and antenna look angles.

The subsystems described above are panel-mounted. The entire system (except antennas) fits into a space smaller than 50 cubic decimeters ($1 \times 1 \times 2$ feet) with weight less than 12 kg. This system provides a strong advantage in terms of cost, complexity, weight, and flexibility compared to network-analyzer based tower-mounted scatterometer systems. The radar can operate with any wide-band antenna in the 100-1200 MHz range, or alternately with multiple narrow-band antennas in the desired frequency ranges of operation. The antennas we used in the measurements are log-periodic antennas covering 105 to 1300 MHz

113

with gain of 11 to 13 dBi. The half power beamwidth is 70° to 60° in E-plane and 130° to 110° in H-plane.

5.3   Calibration

5.3.1   Internal Electronic Calibration

The internal electronic calibration provides system diagnostics before the antennas. The signal for this calibration goes through the calibration loop indicated in Figure 5.1. The typical internal calibration results are shown in Figure 5.3 and 5.4 for L-band and P-band respectively.
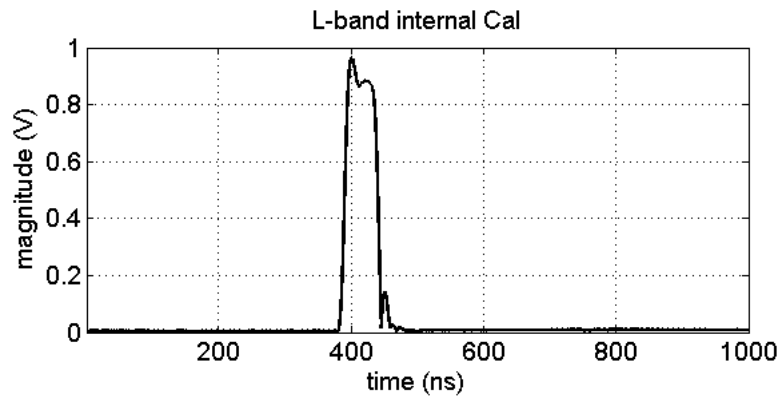
Figure 5.3: L-band internal electronic calibration

5.3.2   Sky Calibration

The sky calibration is to remove the spurious signal generated by the antennas from the measurements. Particularly, it is used to remove the cross-coupling between the transmit and receive antennas in this bistatic system as well as signal reflected due to antenna mismatch. The sky measurements are shown in Figure 5.5 and 5.6 for L- and P-band respectively. In L-band measurements, the protect switch is used to switch on the receive chain right before the arrival of the expected signal at the RX antenna, so that the antenna
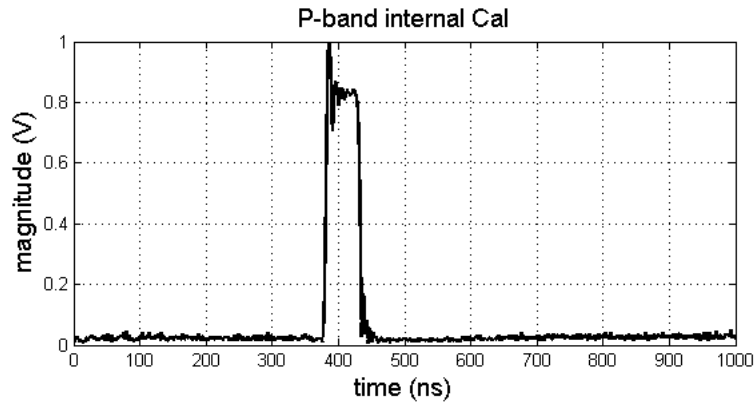
Figure 5.4: P-band internal electronic calibration

cross-coupling can be avoided. This switch is not used in P-band measurements due to the resonance problem caused by it. Therefore, the cross-coupling can be seen clearly in Figure 5.6. The sky measurements will be subtracted from the actual ground measurements (plotted as well in Figure 5.5 and 5.6) to complete the sky calibration.
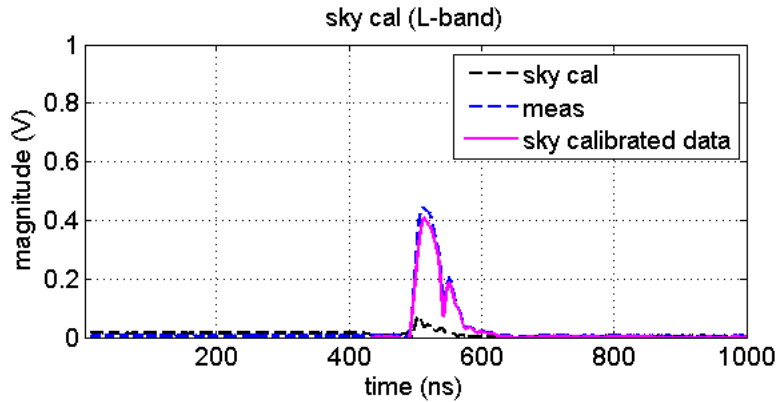
Figure 5.5: L-band sky measurement (with comparison to a ground measurement)

5.3.3 Corner Reflector (CR) Calibration

The measurements of targets with known radar cross section (RCS) calibrate the measured radar cross section RCSs of the unknown targets. In our measurements, we use a triangular trihedral corner-reflector (Figure 5.7).

There are several ways of calculating the corner reflector RCS. When the corner re-

115
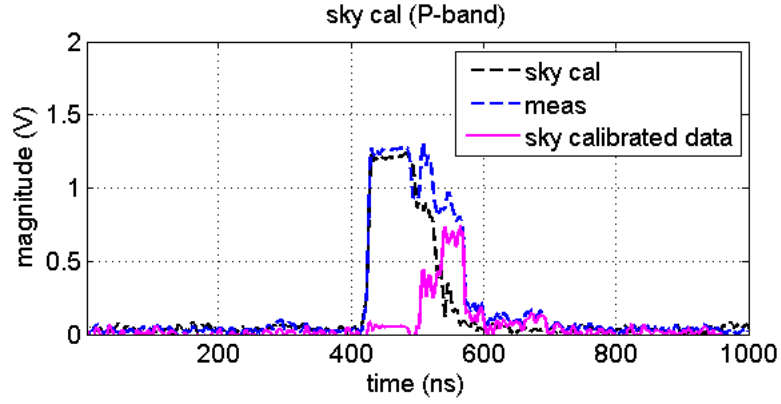
Figure 5.6: P-band sky measurement (with comparison to a ground measurement)

Figure 5.7: Corner reflector calibration

flector is sufficiently large (its dimension $> 10\lambda$) and located in the far-field of the antenna, the effective area can be found from [57]

$$A_{eff} = A \cdot (\cos\alpha\cos\phi\sin\theta + \sin\alpha\cos\theta) \qquad (5.1)$$

where $A = \frac{\sqrt{3}}{2}l^2$, θ_{bs} is the boresight angle from radar antenna, $\alpha = \arctan\frac{1}{\sqrt{2}}$ is as defined in Figure 5.8, and ϕ is the azimuth tilt angle.

Therefore, the RCS of the corner reflector is computed by

$$\sigma_{CR} = \frac{4\pi A_{eff}^2}{\lambda^2} = (\cos\alpha\cos\phi\sin\theta + \sin\alpha\cos\theta)\frac{3\pi l^4}{\lambda^2} \qquad (5.2)$$

116
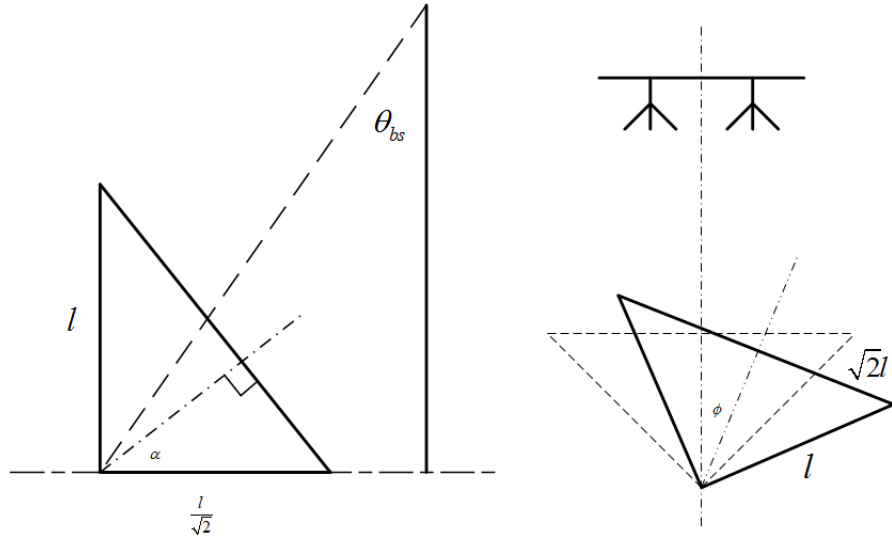
Figure 5.8: Corner reflector calibration geometry

A corrected expression for this geography optics (GO) solution predicts the maximum RCS of the CR as $\sigma_{CR} = \frac{4\pi l^4}{3\lambda^2}$ [57]. The corner reflector we used in the experiment has $l = 2.4157$m, which is sufficiently large for L-band. Without azimuth tilting ($\phi = 0$) and with elevation tilting $\theta_{bs} + 8° = 48°$, $\sigma_{CR} = 30.7$ dB for L-band.

The above approximation ignores the scattering from the edges of the reflector and assumes the plane wave incidence, which is not valid when the corner reflector is close to the antenna or in its near-field (true for P-band measurement). For more accurate RCS computation, numerical solutions must be used [58][59].

The focused signal return from the ground is compared with the focused measurement of the CR. As the CR RCS is known, the RCS from the ground can be estimated.

5.4 Radar Operation

The radar is mounted on a telescoping tower as shown in Figure 5.9. It is controlled through wireless connection from the ground laptop. The auxiliary module inside the radar controls the motor to rotate the antennas to the required angles for ground measurements and sky calibration.

Figure 5.9: Tower based measurements (left) and sky calibration (right)

To achieve better resolution and signal to noise ratio for ground measurements, a larger aperture is synthesized vertically by taking measurements at points of different antenna positions forming the elements of an array (Figure 5.10). This synthetic aperture is usually formed by 15 altitudes (recorded for signal processing) with step size of 10 cm and 20 cm for L-band (wavelength: 30 cm) and P-band (wavelength: 69.0 cm), respectively.

At each altitude, besides a set of internal calibration pulses, a large number of CW pulses (usually more than 300) are transmitted and received to average out the background noise. Measurement data are recorded to files and stored to the system hard drive.

5.5   Signal Processing

The stored raw data are the time domain real values of the I and Q channels at the outputs of the quad demodulator, which can be combined to form the complex datapoints. The sky measurement is subtracted from the ground measurements to remove system biases
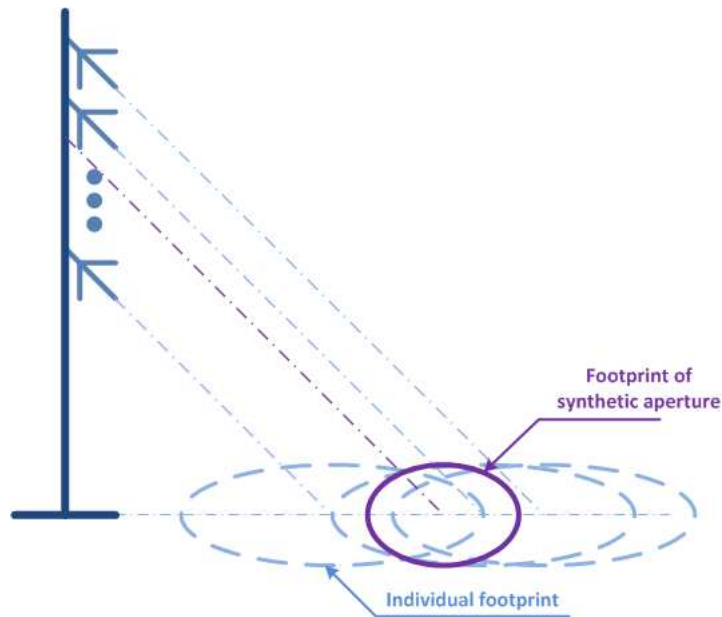
Figure 5.10: Focusing of the synthetic aperture

and antenna cross-coupling. The background measurement is subtracted from the corner-reflector (CR) measurements to keep only the signal returning from the CR. These datasets are then further processed to focus the beam.

To focus the beam, the middle point of the aperture is chosen as the reference point. Time shifts of different altitudes in reference to this point are calculated from the altitude records and the look angle. To perform the focusing, the signal envelops at different altitudes are used to reconstruct the full time-domain waveforms. The time shifts are applied to these full frequency waveforms, and the signals from all altitudes are superposed to give the focused array waveform. The results is effectively a constructive addition at the focus point of the array on the ground and a destructive addition at all other points. This way, we achieve an effective high gain from the synthesized array. Path loss correction can be applied to the measurements before performing the superposition.

Similar processing is done for CR measurements. When the CR used is small, pythagorean theorem can be used to calculate the time shift; the antenna pattern correction will be necessary.
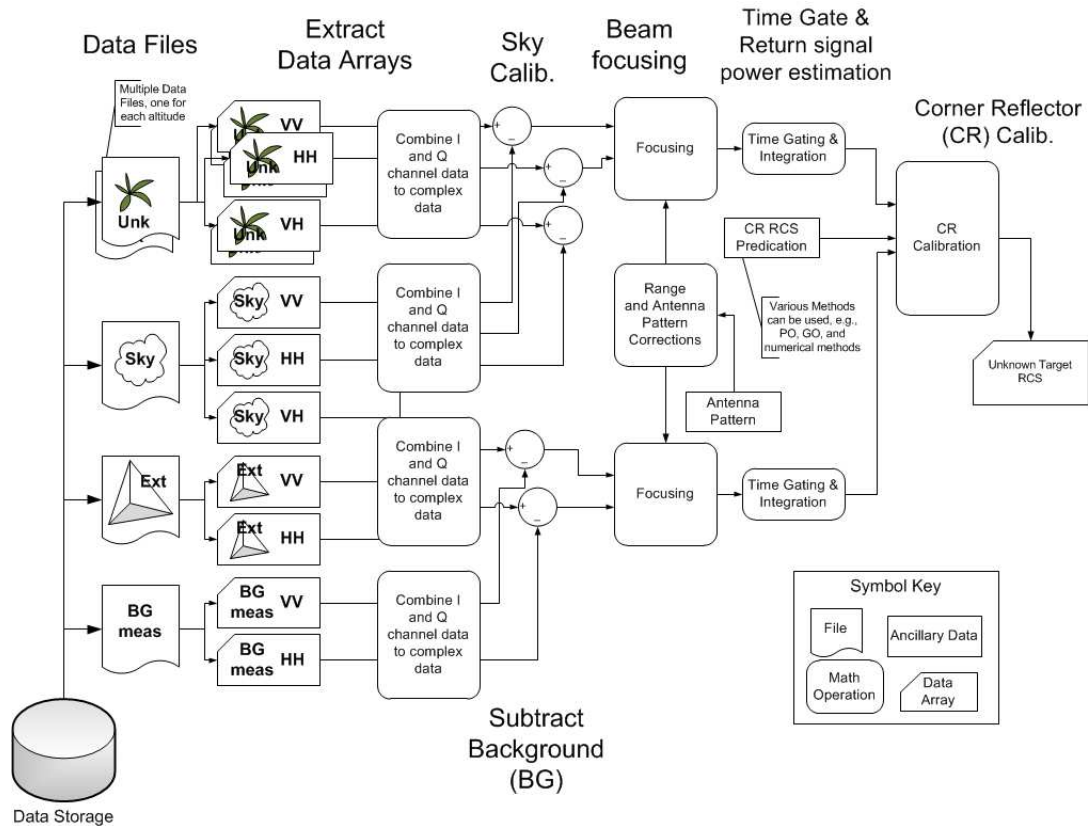
Figure 5.11: Data processing flow chart

Ground return signal power is determined from integrating the signal magnitude within the footprint corresponding to the estimated time interval of the focused pulse. Similarly, the CR return signal is determined, which is linearly related to its radar cross section (RCS). Since the CR RCS can be predicted theoretically, the RCS of the ground is obtained.

5.6 Field Measurement at UF IFAS

Measurements using this radar system have been performed at several locations for system testing and application. One of the main field measurements is carried out during the summer 2011 at the Institute of Food and Agricultural Sciences (IFAS), University of Florida, in Gainesville, FL (Figure 5.12), which is one of the field campaigns in the MicroWEX series [60].

120
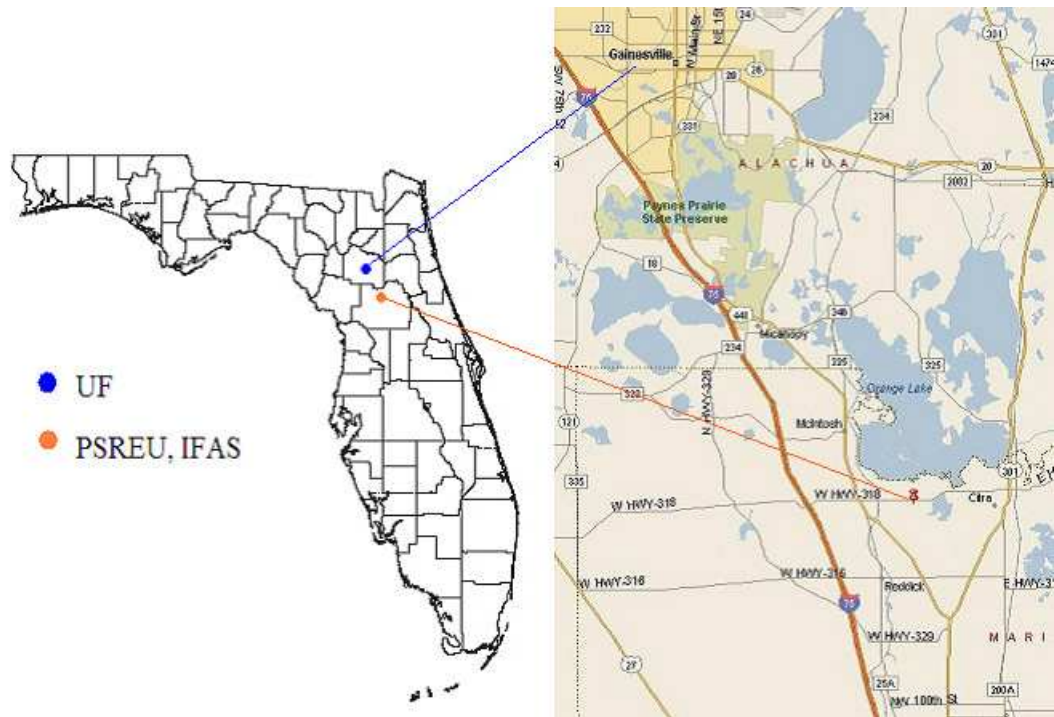
Figure 5.12: Field measurement location

The objective of this series of field campaigns is to understand the relationship between the microwave signatures and the soil moisture as the field conditions (e.g., temperature, water content, etc.) and biomass vary in a dynamic agricultural canopy throughout the growing season. During the summer 2011, a $\sim 200 \times 200$ square meters corn field was observed by multiple microwave remote sensing systems, including both radar and radiometer, from planting in June through harvest in September. Our radar is one of the remote observing sensors.

The radar measurements were taken every month during the period before-planting (bare soil) till harvest. The corresponding ground conditions, including soil moisture profile, soil temperature, precipitation, surface roughness, crop properties, are measured and collected using different sensors and approaches (such as time-domain reflectometer (TDR), thermistor, rain gauge, meshboard, etc.) at multiple locations by our collaborators from University of Florida. The ground data are the inputs to the scattering models for comparisons of model predictions and measurements. Moreover, as multiple systems were

121

observing the same field, comparison among different systems is of interest as well as the data from all systems become available in the future.

5.7   Primary Results

5.7.1   Repeatability Test
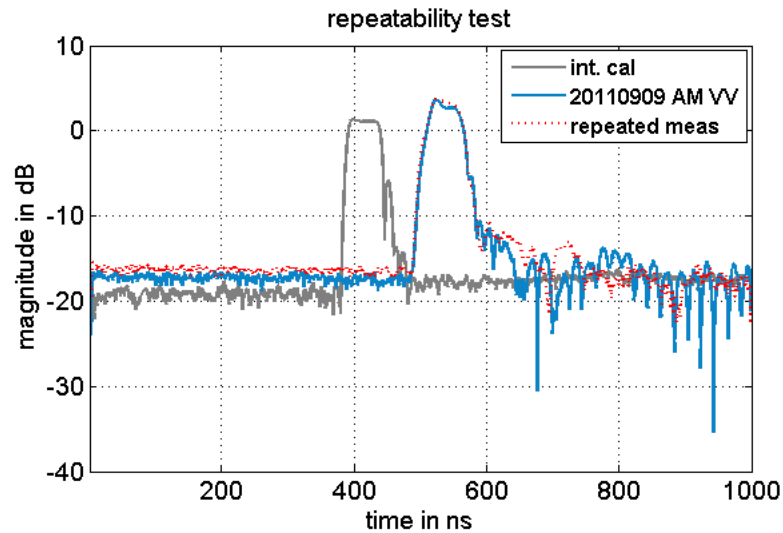
Figure 5.13: Repeatability test of the system

The repeatability of the radar system was tested by taking non-stop measurements sequentially. Two repeated measurement results can be seen in Figure 5.13, indicating the measurement stability of the system.

5.7.2   Corner Reflector Measurements

The radar measurements of the corner-reflectors are shown in Figure 5.14 for small CR ($l = 91.57$cm) and Figure 5.15 for large CR ($l = 241.57$cm). The measurements show difference between HH and VV components, which does not agree with the theoretical prediction. This can be caused by the misalignment of the CRs and the scattering from the edge of the reflectors. Nevertheless, the magnitude differences between the small and large
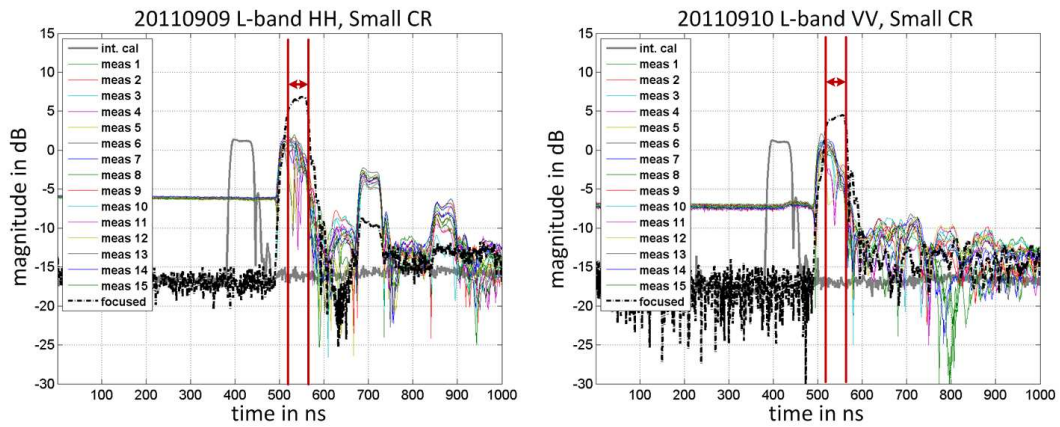
Figure 5.14: L-band Measurements of the small corner reflector
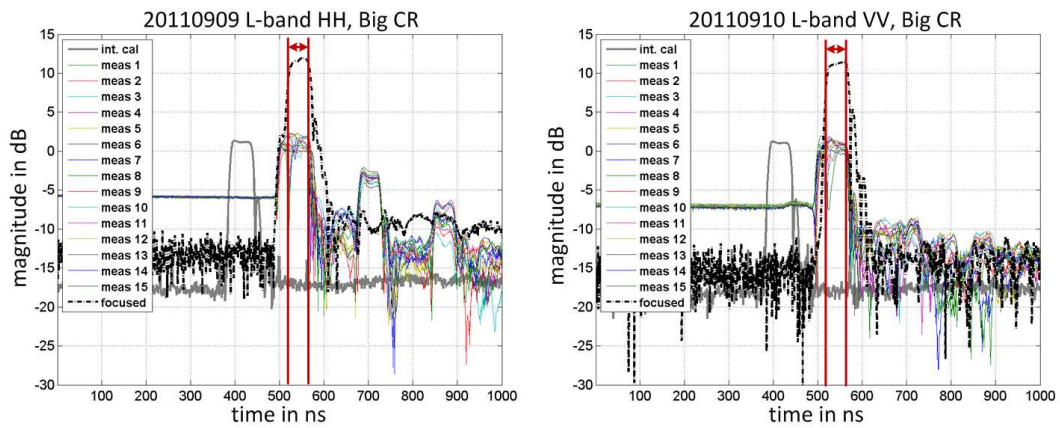
Figure 5.15: L-band Measurements of the big corner reflector

CRs are 5.5 dB in HH and 8.0 dB in VV. The theoretical predicted difference is 8.4 dB. The results of large CR will be used to calibrate the field measurements.

5.7.3 Bare Soil Measurements

Before planting the corn, four days of measurement were done to the bare soil under different conditions (unplowed and plowed, dry and wet). We will first show the measurement results, and compared them with the model predictions simulated using the ground truth that is determined from the ground sensors and meshboard measurements.
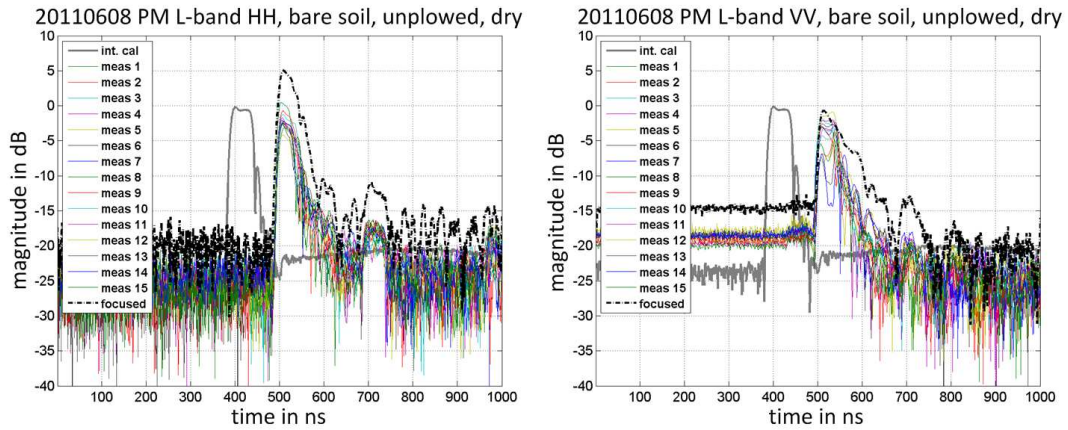
Figure 5.16: L-band Measurements of the unplowed dry field

Radar measurements

The radar measurements started on the day 2011/06/08 when the field was unplowed and dry. The field was plowed at the noon of 2011/06/09 and irrigated during the night of 2011/06/10. The radar measurement and focusing results under these conditions are shown in Figure 5.16, Figure 5.17, and Figure 5.18, where the unfocused signals are plotted in colored lines, and the focused signal is plotted using dashed line. By focusing the beam, the enhancement of the return signal from the ground can be seen clearly from these figures.

Figure 5.16 and Figure 5.17 plot the results of the dry field before and after being plowed. Compared with Figure 5.16, a signal appears more prominently in the plowed dry surface results (Figure 5.17) between 510 ns to 560 ns, which corresponds to the expected arrival time of the ground return. This return signal is increased even more in the plowed wet soil measurement (Figure 5.18).

Being calibrated with the CR measurements and the estimated footprint area, the RCSs of the field of bare soil under above different conditions are calculated from the radar measurements. They are compared with our model predictions in the next subsection.
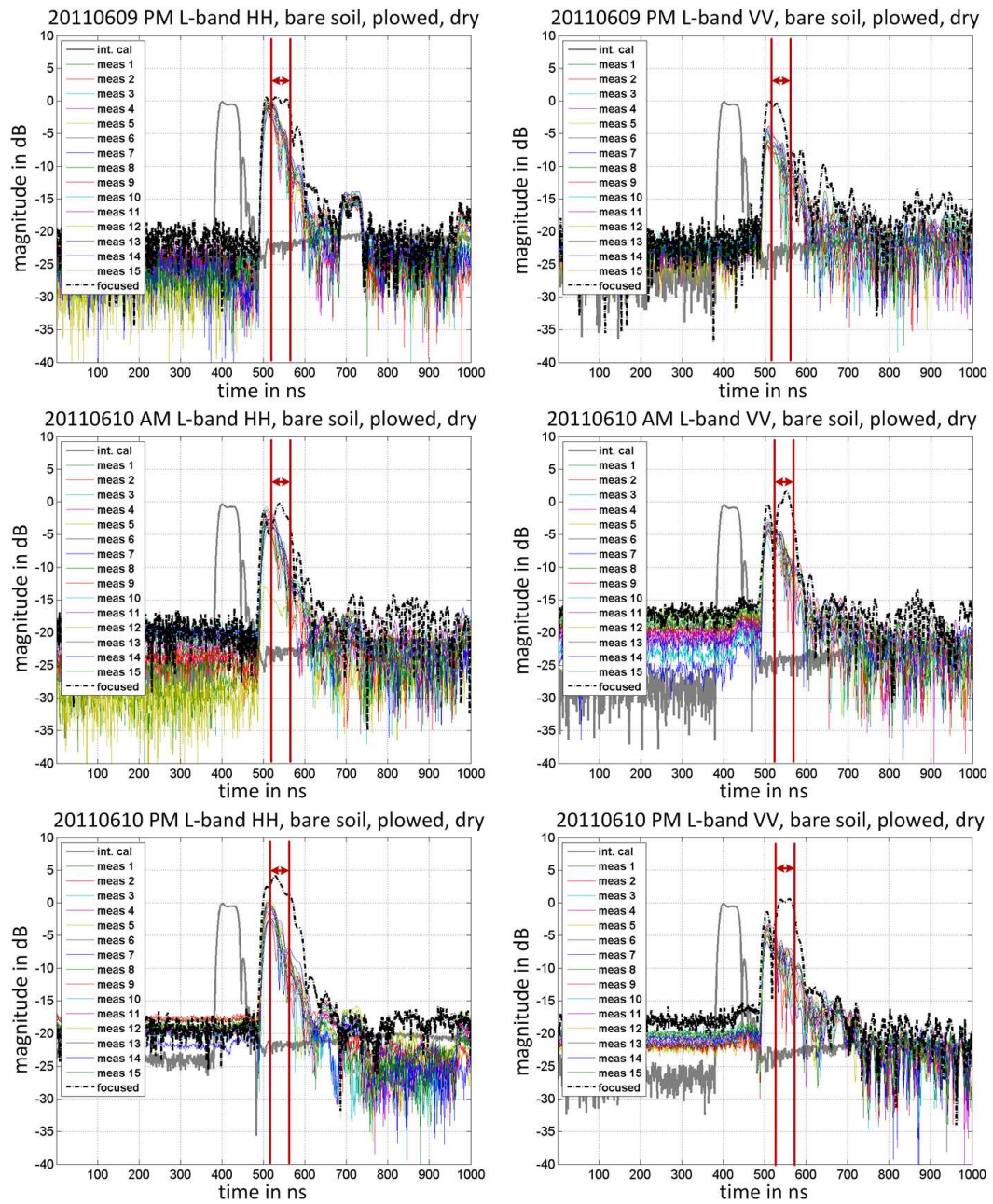
Figure 5.17: L-band Measurements of the plowed dry field

Comparison with model prediction

Model prediction of the RCS of the bare field requires the knowledge of the ground parameters including surface profile and soil moisture content at the surface and subsurface.
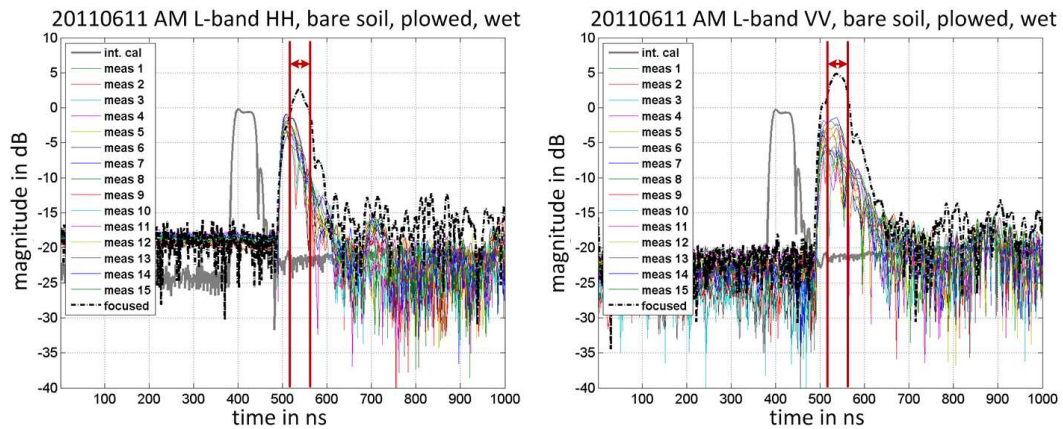
Figure 5.18: L-band Measurements of the plowed wet field

Since the corn field has a pattern that is generally smooth in the direction perpendicular to the radar pointing direction, the field is viewed as a surface with 1D roughness (varying along the radar look direction). The roughness was measured using a meshboard as shown in Figure 5.19 and Figure 5.20 for unplowed and plowed fields. Estimated surface roughnesses from these meshboard measurements are listed in Table 5.1.

The soil consists of 89.4% sand, 7.1% clay, and 3.5% silt. Volumetric water con-

Figure 5.19: Unplowed dry surface

tent of the soil was measured at different depths by ground sensors. Sensor locations are illustrated in Figure 5.22, denoted by 'NE', 'SW', and 'SE'. Measurements of sensor 'NE' at North Station are used for simulation here. The soil moisture results during these four-day (DOY159 to DOY162) measurements are plotted in Figure 5.21 at sensors of different

126

Figure 5.20: Plowed dry surface

Table 5.1: SOIL ROUGHNESS

field condition	h	l_c
unplowed (06/09)	7.83 mm ($h = 0.026\lambda_0$, $kh = 0.16$)	73.97 mm ($l_c = 0.25\lambda_0$, $kl_c = 1.55$)
plowed (06/09)	12.96 mm ($h = 0.043\lambda_0$, $kh = 0.27$)	69.13 mm ($l_c = 0.23\lambda_0$, $kl_c = 1.45$)
plowed (06/11)	16.04 mm ($h = 0.054\lambda_0$, $kh = 0.34$)	76.23 mm ($l_c = 0.25\lambda_0$, $kl_c = 1.60$)
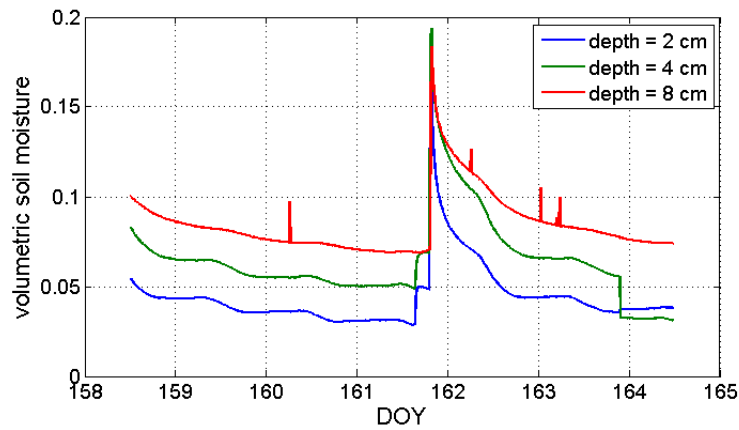
Figure 5.21: Ground measurement of soil moisture

depths (2 cm, 4 cm, and 8 cm). Values of all three sensors are used to form a dielectric profile for model simulation shown in Figure 5.23.

With the estimated surface roughnesses and the soil moisture profiles, we simulated the scattering from a single surface with 1D roughness and a dielectric profile underneath

127
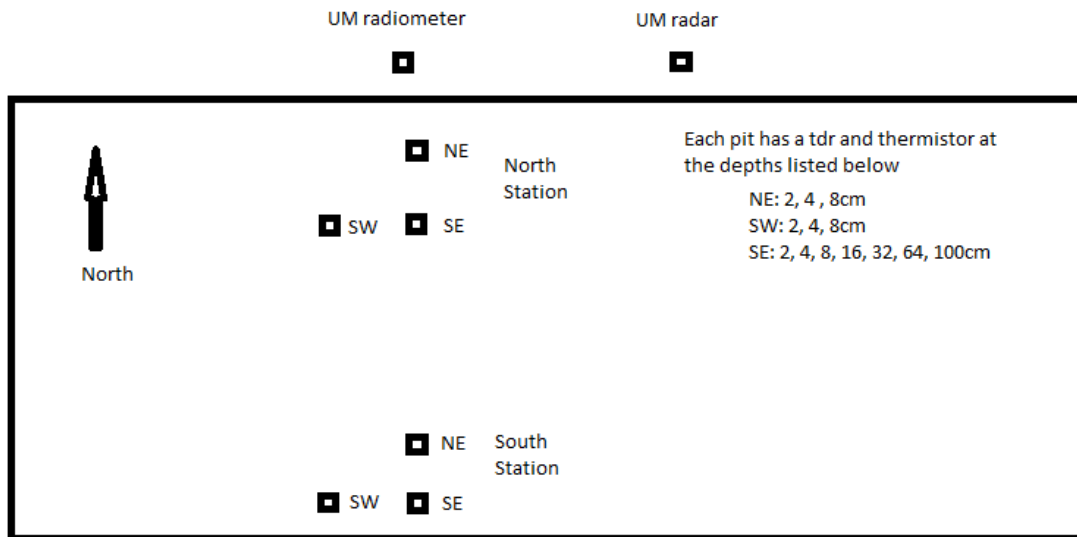
Figure 5.22: Ground measurement layout
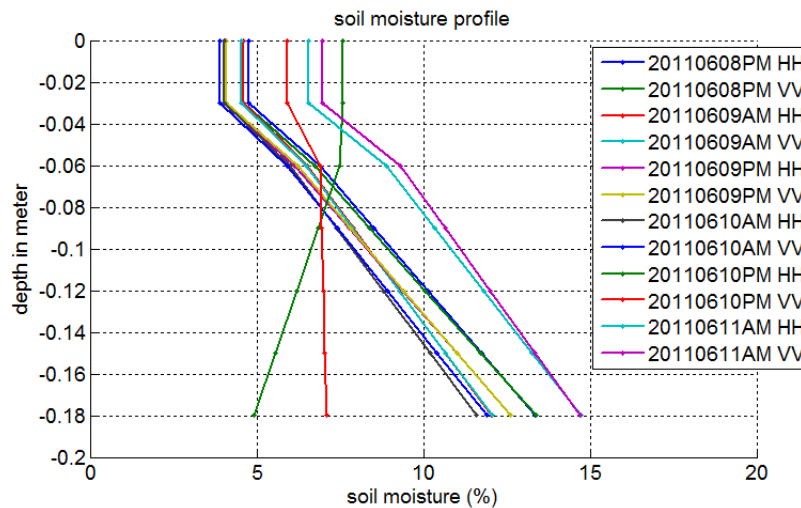
Figure 5.23: Soil moisture profiles used in model simulations

as illustrated in Figure 5.24. The model predictions of backscattering cross sections are listed in Table 5.2, while the backscattering cross sections estimated from measurements are shown in Table 5.3. Figure 5.25 plots both results for comparison.

The comparison of the predicted and measured backscattering cross sections shows an overestimation bias of ~6.20 dB in the measured values, with deviation of ~5.5 dB. The measured RCSs as a function of measurement time are plotted in Figure 5.26. As
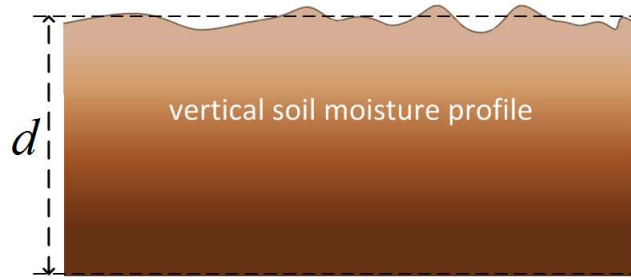
Figure 5.24: Simulated geometry for comparison with measurement ($d = 20$ cm)

Table 5.2: SIMULATION PREDICATED BACKSCATTERING CROSS SECTION (AM: MORNING SET; PM: AFTER-NOON SET)

Date (DOY)	HH (AM)	VV (AM)	HH (PM)	VV (PM)
2011-06-08 (159)	NA	NA	-28.64 dB	-24.18 dB
2011-06-09 (160)	-28.70 dB	-24.25 dB	-24.34 dB	-20.11 dB
2011-06-10 (161)	-24.41 dB	-20.19 dB	-23.30 dB	-18.87 dB
2011-06-11 (162)	-21.65 dB	-17.40 dB	NA	NA

Table 5.3: MEASURED BACKSCATTERING CROSS SECTION

Date (DOY)	HH (AM)	VV (AM)	HH (PM)	VV (PM)
2011-06-08 (159)	NA	NA	-20.54 dB	-17.44 dB
2011-06-09 (160)	-18.67 dB	-21.12 dB	-13.76 dB	-16.43 dB
2011-06-10 (161)	-18.02 dB	-14.88 dB	-13.98 dB	-13.11 dB
2011-06-11 (162)	-17.83 dB	-10.66 dB	NA	NA

can be seen, the measured values are larger than the model predictions in general. Several datasets show larger HH measurement values than the VV results, which is different from what we expected based on the theoretical solution. The measured VV values show a generally increasing trend as the field condition changes, which can also be observed from the simulation results.

To further understand the causes of the error, we did a sensitivity analysis of the backscattering cross section to the variations in the simulation parameters.
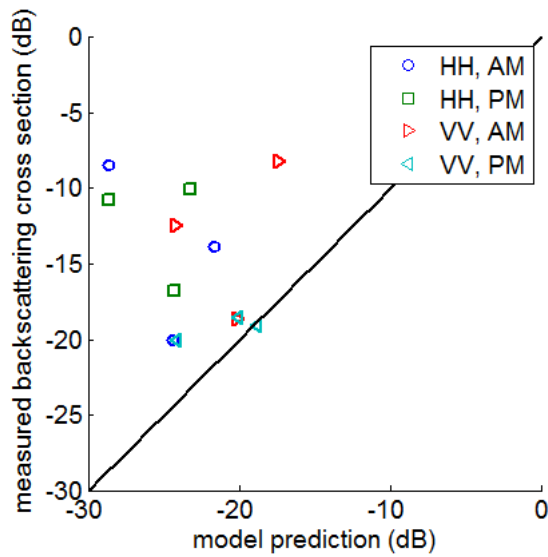
Figure 5.25: Comparison of the L-band measured data (Table 5.3) and model predications (Table 5.2).
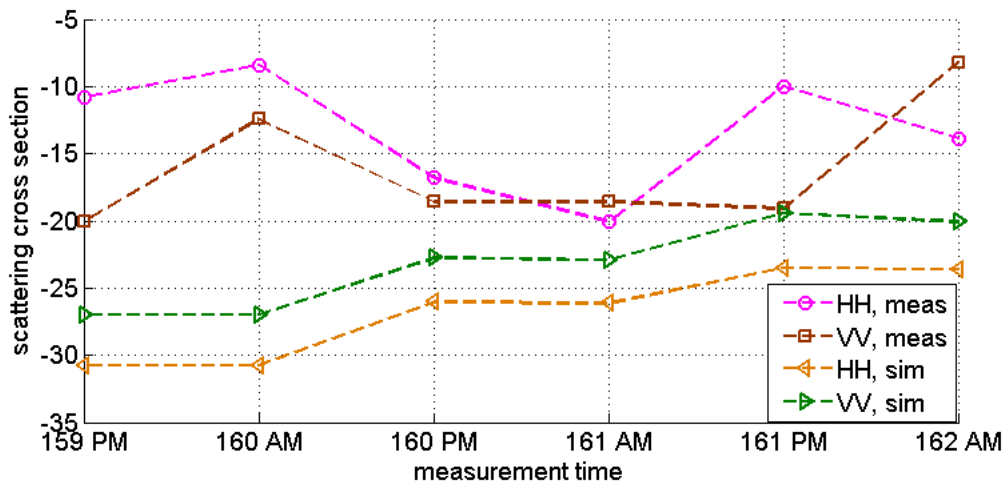
Figure 5.26: Measured RCSs as a function of measurement time

Analysis of error sources

i. Error in surface roughness measurement

To study the impact of the error in the roughness measurement, we increases the rms height of the simulated surface to 150%, 200%, and 250% of the original rms height, while maintaining the ratio between the rms height and the correlation length.

130

Table 5.4 and Figure 5.27 show the improvement in the comparisons between the

Table 5.4: SENSITIVITY OF THE COMPARISON BETWEEN MEASUREMENTS AND MODEL PREDICTIONS TO THE SURFACE ROUGHNESS

rms height increment	0	150%	200%	250%
Bias	6.2 dB	3.84 dB	2.15 dB	0.68 dB
Std. Dev.	5.5 dB	4.8 dB	4.32 dB	3.91 dB
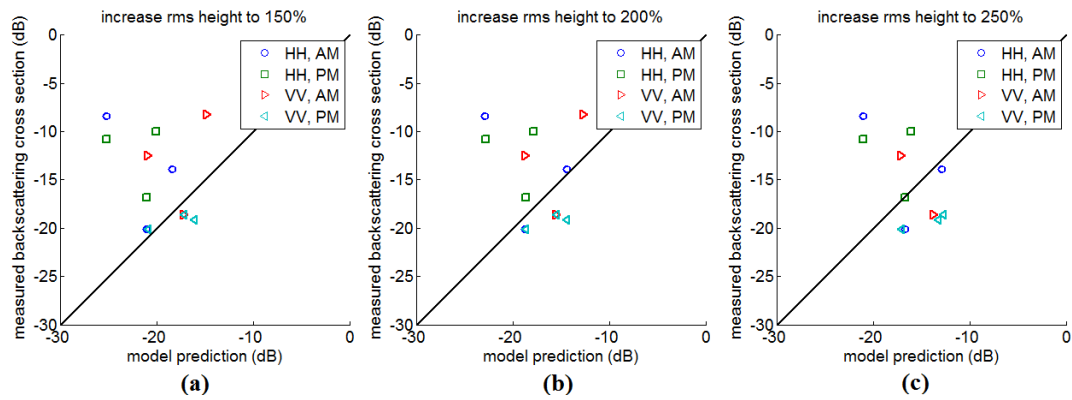
Figure 5.27: Comparison of the L-band measured data with the model predications of increased rms heights (Table 5.4)

measurement and model predictions using increased surface roughnesses. Note that even increasing the roughness to 200% of the measured values still means a rms height range of ~1 to ~3 cm. Therefore, the roughness measurement error can have large impact on the comparison between the predicted and measured backscattering cross sections. Enhancement in the accuracy of such measurements is important for the experimental validation of the rough surface scattering model.

ii. Error in soil moisture profile determination

To study the impact of the error in the soil moisture profile determination on the comparison between the measurements and the model predictions, we increase the overall soil moisture profile by 6%, 10%, and 15%. Comparisons between the measurements and the simulations using the enhanced soil moisture profiles show improvement in the agreement

131

of the results (Table 5.5). This improvement is smaller compared to that in the above study of increasing surface roughness.

Table 5.5: SENSITIVITY OF THE COMPARISON BETWEEN MEASUREMENTS AND MODEL PREDICTIONS TO THE SOIL MOISTURE

soil moisture increment	0	6%	10%	15%
Bias	6.2 dB	4.97 dB	4.86 dB	4.5 dB
Std. Dev.	5.5 dB	5.37 dB	5.35 dB	5.3 dB

Additionally, besides the moisture profile in depth, the soil water content also varies horizontally depending on the ground topography. In our simulations, we use one sensor location to represent the moisture of the whole footprint, which can cause errors in the predicted results as well.

iii. Error in surface profile

In our model simulations performed for above comparisons, the surface is assumed to have only 1D roughness along the look direction of the radar, i.e., a 2D scattering solution is used to predict the theoretical scattering values. However, due to the large beamwidth of the radar antenna, the validity of the 2D scattering model is limited and becomes less accurate, which causes error in our comparisons as well. To estimate the impact of this error, we create a 2D rough surface with the 1D roughness parameters and simulate its scattering cross section. The comparison between the measurements and the predictions from the 3D scattering model show both smaller bias of 3.05 dB and smaller standard deviation of 4.12 dB. Accurate comparison between the measured and predicted backscattering cross sections requires the knowledge of the 2D surface profile, which is not available to us.

iv. CR measurement and RCS computation

Misalignment of the calibration target can cause error in the measurement results. Using the GO model for the CR RCS computation, the impact of the CR misalignments in both elevation and azimuth directions is studied. As can be seen from Figure 5.28, the error

caused by the CR misalignment is smaller than 1 dB.

Besides the misalignment of the CR, performing low frequency measurement in the
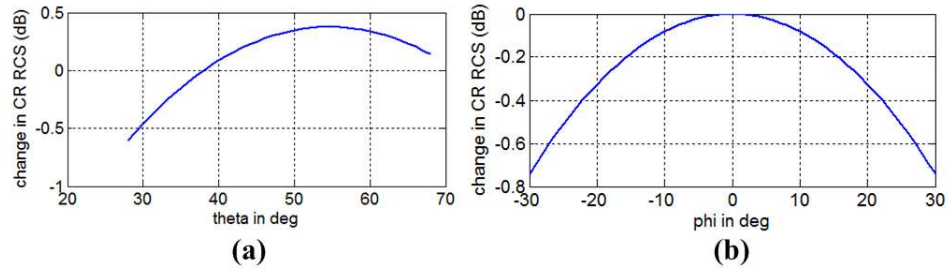
Figure 5.28: RCS changes due to misalignment in (a) elevation direction (theta: elevation angle) and (b) azimuth direction (phi: azimuth angle)

near field range of the CR can cause overestimated CR RCS. In this case, the validity of the high frequency approximation becomes limited, and the scattering from the CR edges, as well as the interactions between the CR and the ground need to be taken into account [57]. More precise numerical solutions based on the near-field calculations are required for more accurate calibration.

iv. Other error sources

Besides the error sources discussed above, there are other factors that could cause error in the comparison between the model simulations and the radar measurements.

- **Speckle:** The inherent presence of speckles in the measurements causes large deviations in the results, whose remedy is taking more samples at different looks.

- **Focused footprint area determination:** The error in the focused footprint area determination can result in larger backscattering cross sections if the area is underestimated.

- **Antenna pattern and absolute gain determination:** The antenna pattern and absolute gain need to be precisely measured for accurate determination of the footprint area and the calibration with the targets.

• **Radio frequency interference** The interference from the tower body, or the neighboring systems operating concurrently in the field can cause larger measured RCS as well.

5.7.4 Measurement Signature Change Over the Growing Season

The radar measurements were taken every month during the growing season of the corn field (Figure 5.29). Though we don't have a combined vegetation scattering model to predict the signal return, we would like to show the signature of the return signal as the corn grew.

The first row in Figure 5.30 shows the measurements of the field of germinating corn

Figure 5.29: Growing season of corn field: germinating (left), growing ∼1 meter tall (center), and before harvest (right)

corresponding to Figure 5.29 left. The signature of the return signal does not change much from the bare soil measurements, as expected. The second row in Figure 5.30 presents the measurements of the field when the corn grew approximately 1 meter tall before earing (Figure 5.29 center). More features appear in the return signals even after 600 ns. Both the HH and VV measurements show larger ground return signals. The cross polarization components are also measured, showing similar signature as the copol components. This becomes more clear in the third row of Figure 5.30, showing the measurements of the corn field right before harvest (Figure 5.29 right).
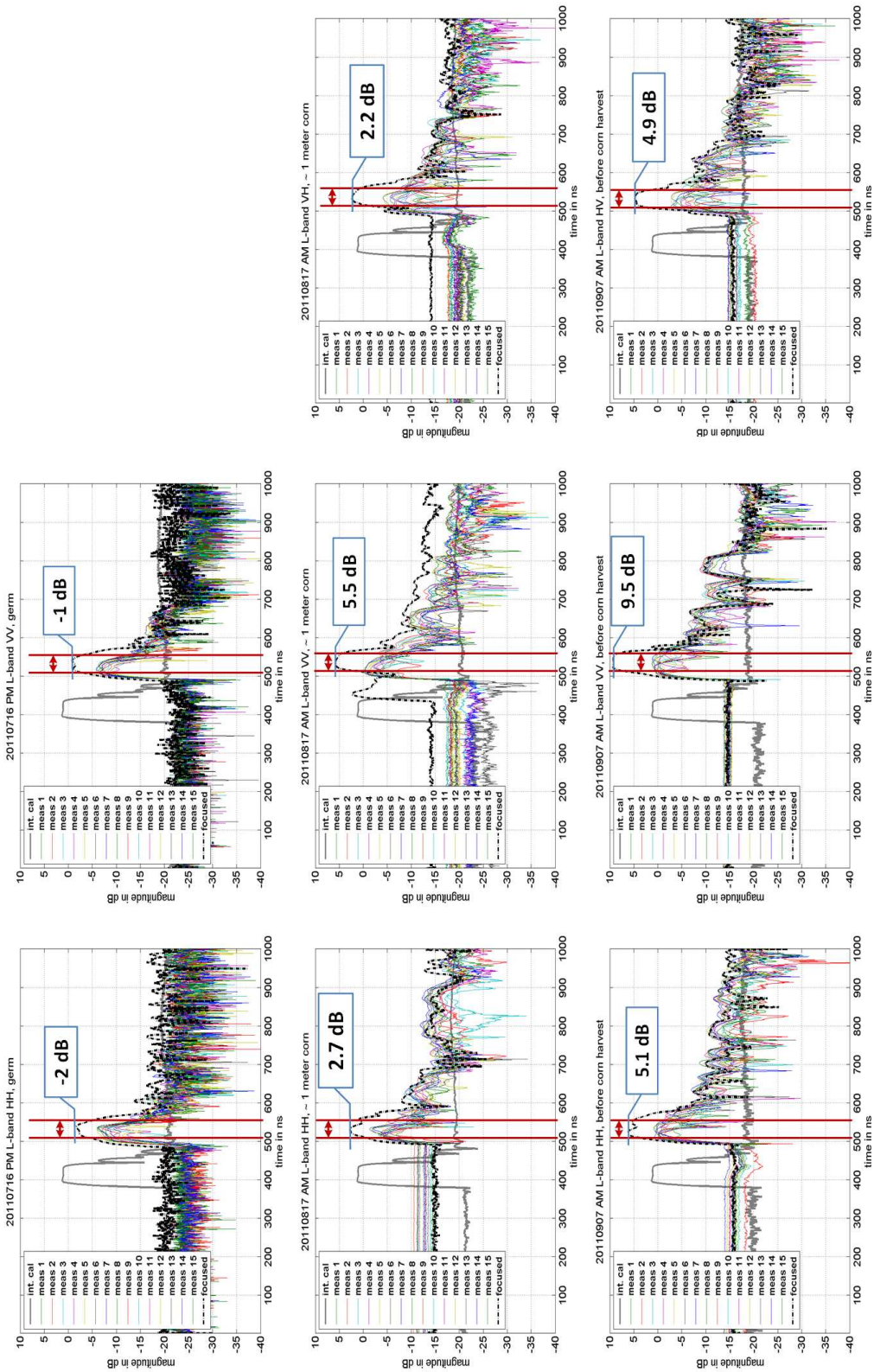
Figure 5.30: Growing season of corn field: germinating (row 1), growing ~1 meter tall (row 2), and before harvest (row 3)

5.7.5 P-band Measurements
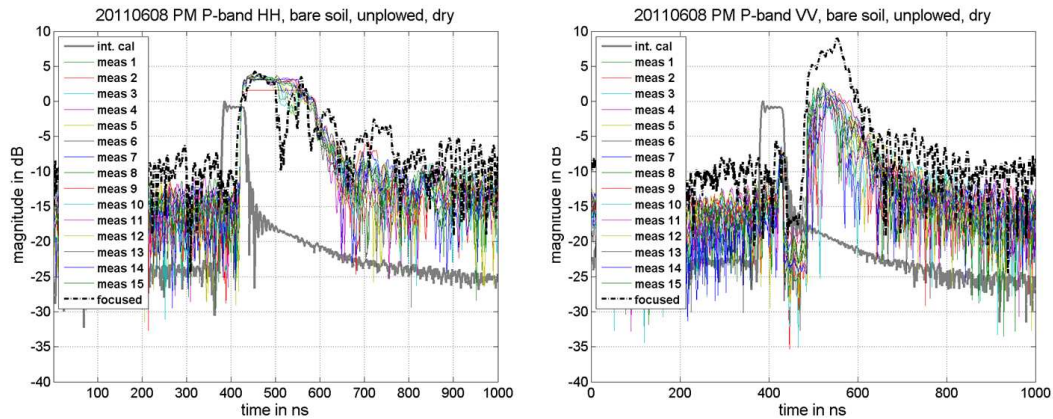
Figure 5.31: P-band Measurements of the unplowed dry field

Besides the L-band measurements, P-band (435 MHz) measurements are performed as well. Results of the bare soil are shown in Figure 5.31 (for unplowed, dry field), Figure 5.32 (for plowed, dry field), and Figure 5.33 (for plowed, wet field). Compared to the L-band measurement results, the P-band results show more features/noises. They can be due to the larger interference caused by the antenna cross coupling, since the protect switch in the receive chain is deactivated to avoid the ringing effect. The interference from the tower body could also add more noise to the measurements. Quantitative evaluation of the P-band results requires the P-band calibration of known targets. However, our CR is too small to be a good target for P-band; and a large enough P-band target would need near-field RCS prediction model as well. These are the problems needed to be addressed in the future work.

5.8 Summary and Conclusion

A newly designed and built tower-based multiple-low-frequency radar system is introduced in this chapter. This radar is a compact, remote-controlled, stand-alone system with larger output power. It has been used in several field campaigns for surface, subsurface, and

136
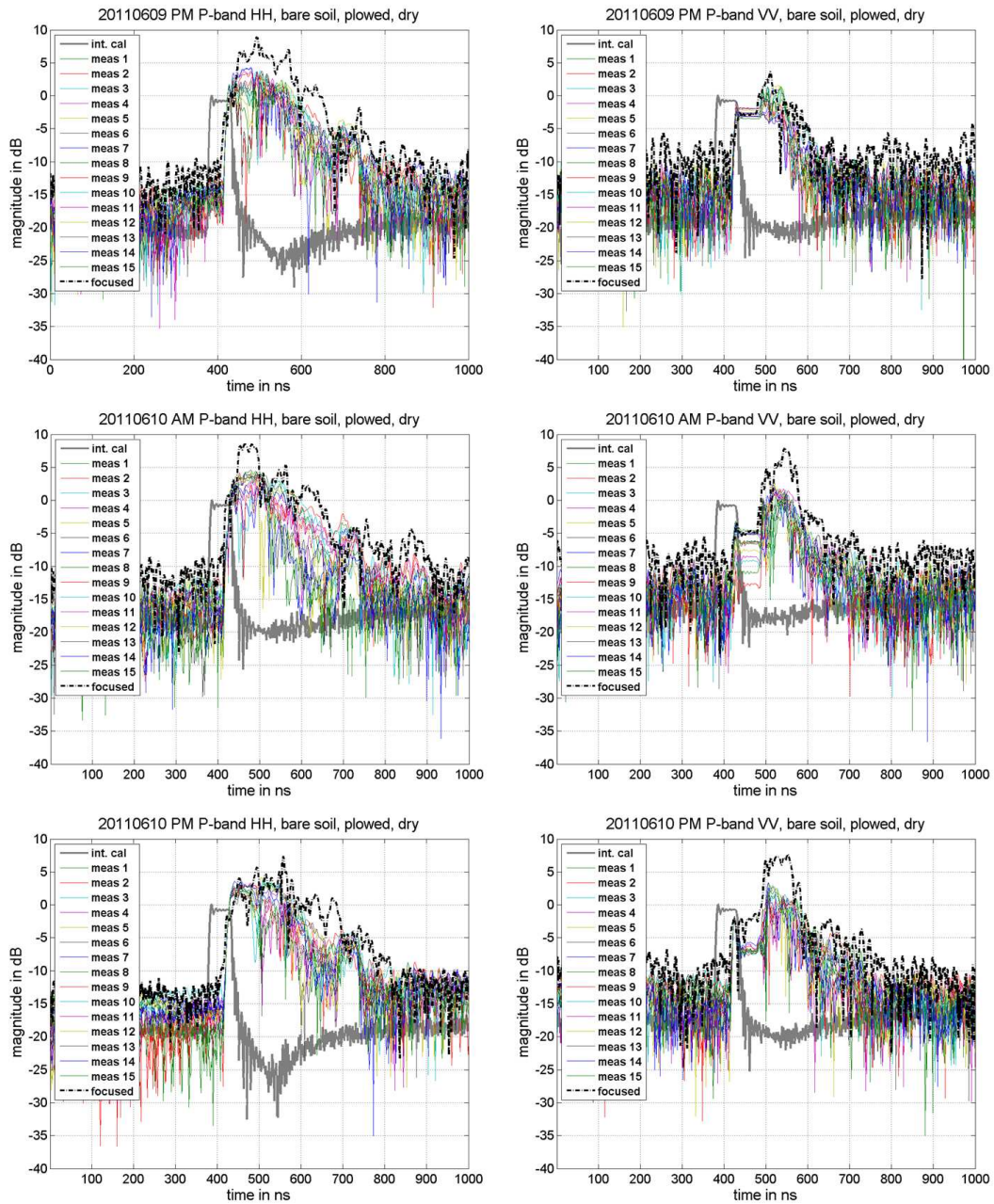
Figure 5.32: P-band Measurements of the plowed dry field

subcanopy soil moisture detection. In this chapter, primary results from the field measurements of the corn field over the growing season are shown and analyzed. The results show the radar sensitivity to soil roughness and moisture. Signal signature changes can also be seen over the growing season of the corn.
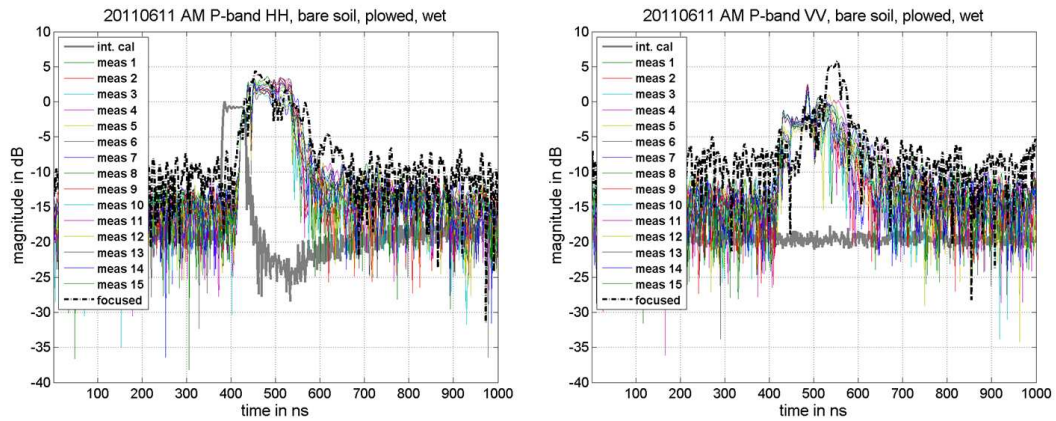
Figure 5.33: P-band Measurements of the plowed wet field

Meanwhile, measurements from this radar system also indicate problems need to be addressed in near-field radar measurement, data processing, and model validation. First of all, accurate data processing and error analysis require further numerical modeling of the near-field backscattering of the calibration targets (e.g., corner-reflectors). Precise determination of the footprint area is also critical and should be done based on the system sensitivity. For model validation, a methodology of backscattering aggregation within the footprint based on the model predicted scattering from sub-areas need to be used, considering different field illumination angles in the footprint.

CHAPTER 6

Conclusion and Future Work

6.1 Conclusion

To summarize, Chapters 2 to 4 of this dissertation presented a set of increasing complex forward models predicting the three-dimensional electromagnetic scattering from the layered rough surfaces with buried inhomogeneities. These were followed by Chapter 5, which introduced a tower-based low-frequency radar system newly designed and built for surface, subsurface, and subcanopy soil moisture detection.

Starting with single rough surface scattering, Chapter 2 described a solution using stabilized extended boundary condition method (SEBCM). We solved the long standing instability issue of the classical EBCM. The SEBCM gives a full-wave surface scattering solution that is valid over a large range of surface roughness. It computes the same size problem more efficiently than spatial domain fully numerical approaches. This SEBCM solution we developed was validated by comparing with solutions provided by several other analytical and numerical models, as well as with actual measurements.

The problem involving multi-layer rough surfaces was solved in Chapter 3 based on the scattering matrix approach and single rough surface solution using SEBCM. This solution is able to simulate dielectric profiles between subsurfaces, representing a more realistic scenario of ground scattering. For multilayer surfaces of large roughness, this is the only

known method that is practically applicable to realistic soil profile scenarios.

Random or root-like media were added to the multi-layered rough surface structure to represent the sublayer inhomogeneities and vegetation roots. Chapter 4 presented the solutions to include the random media in the multilayer rough surface scattering model. The problem was solved using the recursive transition matrix (T-matrix) method for spherical or short-cylindrical scatterers, and the generalized iterative extended boundary condition method was developed for long or root-like cylindrical clusters. Both methods compute efficiently the scattering of these random media, taking into account of the interactions among scatterers. The transition matrix (T-matrix) to scattering matrix (S-matrix) transformation we developed further enables the integration of media scattering with layered rough surface scattering. This completes our model of three-dimensional electromagnetic scattering from layered media with rough interfaces, which is the first ground scattering model having comprehensive subsurface structural definition.

In the last part of this dissertation, we also showed results from experiments aimed at surface, subsurface, and subcanopy soil moisture detection using a tower-based low-frequency radar system.This system is a compact remote-controlled and easily deployed stand-alone high power radar. Field experiment results proved its sensitivity to soil moisture, and paved the way for future experiments and analyses under more varied field conditions.

6.2 Future Work

6.2.1 Scattering Modeling - combination with vegetation scattering model

The solution we developed to the scattering from layered rough surfaces with buried root-like inhomogeneities considers only the structure below the ground surface; the vegetation, because of which the roots exist, is not taken into account. Although this was a

deliberate choice - in that the purpose was to focus only on soil and factors impacting the scattering properties from subsurface features - a complete solution from vegetated ground needs to combine scattering from both above- and below-ground regions. One approach is to combine with one of the commonly used vegetation scattering model such as that in [61]. Such models use Stokes matrices to define the scattering contributions of the vegetation layers, then add them and their interactions with the ground layer. We can convert our scattering matrix to Stokes matrix as well. The Stokes matrices of the above- and below-ground regions can be combined to have the complete scattering solution. The more accurate way of having the complete solution is to solve the scattering from vegetation in a similar way as we did to the scattering from the vegetation roots, which gives the scattering matrix of the vegetation layer. The scattering matrices of the vegetation layer and below-ground layer can be cascaded to describe the total scattering. This approach would yield a much more accurate solution, at the cost of added computational complexity.

6.2.2 Scattering Modeling - computational efficiency enhancement

Though our solution to the ground scattering problem has higher computational efficiency than the pure numerical methods for the problem of the same size, there is still much room for improvement of the computational speed. The results we presented in this dissertation are all simulated using matlab on a desktop PC with a Intel Duo Core processor and 4GB memory. This limits the number of Floquet modes included in the solution, i.e., limits the length of the surface period. The solution should be implemented in FORTRAN to allow larger memory usage and added speed, and parallelized using OpenMP for multi-processing on a computation cluster. The parallelization of the multi-surface algorithm can be performed with respect to surface layers, surface realizations, matrix filling process, and matrix multiplication. The random media scattering solution can be parallelized in sub-cylinder T-matrix computations, cluster T-matrix computation, as well as the matrix multiplications. Enhanced computational efficiency will make these forward models more applicable for the construction of solution spaces as a function of the ground properties,

which can be further used for soil moisture retrieval.

6.2.3 Radar System and Measurements

The tower-based low-frequency radar system is a prototype compact systems for on-demand low-cost soil moisture detection. The hardware system can be significantly improved through several layers of integration: the structure of PC motherboard, FPGA, and solid-state switches can be combined to be a dedicated radar control unit based on MPGA (Microcomputer-FPGA) with switch banks; the RF synthesizer, digitizer, and quad-demodulator are all integrable to be single/multiple compact units. This will result in a lighter, smaller, and less expensive system, which can be put onto other mobile low-altitude platforms. Moreover, a better antenna solution is needed for more directivity and higher gain, especially for lower frequencies (VHF and UHF). This not only reduces the power requirement of the radar system, it also enhances the radar sensitivity to allow the radar operation without the need for synthetic aperture processing, which expands the radar application environments and enables automated radar observation. In the data processing aspect, more precise modeling of the radar cross section of the calibration targets (e.g., CR) is necessary, especially in the near field range. Solving the absolute calibration problem for low-altitude low-frequency radars will have a major positive impact on achieving accurate soil moisture retrievals with such systems.

6.2.4 On-Board Processing

The tower-mounted or future version of the low-altitude compact radar system will be most beneficial in the future if they can integrate processing, calibration, and retrieval algorithms into the radar system. Essentially this will be an additional piece of the digital electronics subsystem, but one that could substantially add to the utility of low-frequency radar systems for scientific and operational use.

APPENDIX

APPENDIX A

Numerical Generation of 2D Random Rough Surface

Considering a 2D randomly rough surface, $z = f(\bar{r}_\perp)$, where $\bar{r}_\perp = (x, y)$, its Fourier transform is

$$F(\bar{k}_\perp) = \frac{1}{4\pi^2} \int_{-\infty}^{\infty} f(\bar{r}_\perp) e^{-i\bar{k}_\perp \cdot \bar{r}_\perp} d\bar{r}_\perp \tag{A.1}$$

where $\bar{k}_\perp = (k_x, k_y)$. For every two points on the surface, (x_1, y_1) and (x_2, y_2), we have

$$\langle f(\bar{r}_\perp) \rangle = 0 \tag{A.2}$$

$$\langle f(\bar{r}_{1\perp}) f(\bar{r}_{2\perp}) \rangle = h^2 C(\bar{r}_{1\perp} - \bar{r}_{2\perp}) \tag{A.3}$$

where $C(\bar{r}_\perp)$ is the correlation function, which is related to the spectral density $W(\bar{k}_\perp)$ by

$$h^2 C(\bar{r}_\perp) = \int_{-\infty}^{\infty} W(\bar{k}_\perp) e^{i\bar{k}_\perp \cdot \bar{r}_\perp} d\bar{k}_\perp \tag{A.4}$$

Two correlation functions are commonly used, the Gaussian correlation function with the corresponding spectral density,

$$C(\bar{r}_\perp) = \exp\left(-\frac{|\bar{r}_\perp|^2}{l^2}\right) \tag{A.5}$$

$$W(\bar{k}_\perp) = \frac{h^2 l^2}{2} \exp\left(-\frac{|\bar{k}_\perp|^2 l^2}{4}\right) \tag{A.6}$$

and the exponential correlation function with its spectral density,

$$C(\bar{r}_\perp) = \exp\left(-\frac{|\bar{r}_\perp|}{l}\right) \tag{A.7}$$

$$W(\bar{k}_\perp) = \frac{h^2 l^2}{2\pi\left(1 + \bar{k}_\perp^2 l^2\right)^{\frac{3}{2}}} \tag{A.8}$$

To generate the rough surface numerically, the 2D rough surface can be represented by its Fourier series

$$f(x,y) = \frac{1}{L_x L_y} \sum_{m=-\infty}^{+\infty} \sum_{n=-\infty}^{+\infty} F_{mn} e^{i(mK_x x + nK_y y)} \tag{A.9}$$

where $K_x = 2\pi/L_x$ and $K_y = 2\pi/L_y$. By comparing the following two representations of the correlation function,

$$\langle f(x_1, y_1) f(x_2, y_2) \rangle =$$
$$\frac{1}{L_x^2 L_y^2} \sum_{\substack{m,n,p,q \\ =-\infty}}^{+\infty} \langle F_{mn} F_{pq}^* \rangle e^{i(mK_x x + nK_y y)} e^{i(pK_x x + qK_y y)} \tag{A.10}$$

and

$$\langle f(x_1, y_1) f(x_2, y_2) \rangle = h^2 C(x_1 - x_2, y_1 - y_2)$$
$$= \iint_{-\infty}^{+\infty} dk_x dk_y W(k_x, k_y) e^{ik_x(x_1 - x_2)} e^{ik_y(y_1 - y_2)} \tag{A.11}$$

it can be seen that $\langle F_{mn} F_{pq}^* \rangle = \delta_{mp} \delta_{nq} X_{mn}$, where $X_{mn} = 4\pi^2 L_x L_y \cdot W(K_m, K_n) = \langle |F_{mn}|^2 \rangle$.

Here we have used $dk_x = \Delta k_x = K_x$ and $dk_y = \Delta k_y = K_y$ to get

$$\frac{2\pi}{L_x} \frac{2\pi}{L_y} \sum_{\substack{m,n \\ =-\infty}}^{+\infty} e^{iK_m(x_1 - x_2)} e^{iK_n(y_1 - y_2)} W(K_m, K_n)$$
$$= \frac{1}{L_x^2 L_y^2} \sum_{\substack{m,n \\ =-\infty}}^{+\infty} X_{mn} e^{iK_m(x_1 - x_2)} e^{iK_n(y_1 - y_2)} \tag{A.12}$$

where $K_m = mK_x$ and $K_n = nK_y$.

145

Utilizing above relations, the 2D random rough surface with dimensions $M \times N$ samples can be obtained by constructing a matrix F_{mn} in the spectral domain. Denoting the matrices of the rough surface and its Fourier series by $[f_{pq}]$ and $[F_{mn}]$, we can write:

$$f_{pq} = \frac{1}{L_x L_y} \sum_{\substack{m= \\ -M/2+1}}^{M/2} \sum_{\substack{n= \\ -N/2+1}}^{N/2} F_{mn} e^{i\frac{2\pi m}{M}p} e^{i\frac{2\pi n}{N}q} \tag{A.13}$$

$$F_{mn} = \frac{L_x L_y}{MN} \sum_{\substack{p= \\ -M/2+1}}^{M/2} \sum_{\substack{q= \\ -N/2+1}}^{N/2} f_{pq} e^{-i\frac{2\pi m}{M}p} e^{-i\frac{2\pi n}{N}q} \tag{A.14}$$

Since $f(x,y)$ is real, the matrix $[F_{mn}]$ has the structure of $F_{mn} = F_{-m,-n}^*$, $F_{M/2,n} = F_{M/2,-n}^*$ and $F_{m,N/2} = F_{-m,N/2}^*$. Hence, entries $F_{0,0}$, $F_{M/2,0}$, $F_{0,N/2}$ and $F_{M/2,N/2}$ are real. Therefore, by generating an $M \times N$ array of random numbers $[c_{mn}]$ with standard normal distribution and rearranging them according to the above structure, $[F_{mn}]$ can be obtained by weighing the rearranged array as $F_{mn} = 2\pi \sqrt{L_x L_y W(K_m, K_n)} \cdot c_{mn}$. The rough surface $f(x,y)$ is then the 2D inverse Fourier transform of the F_{mn} matrix. Depending on the specific IFFT algorithm, rearrangement or re-indexing of arrays may be necessary.

APPENDIX B

Derivation of Floquet Mode Coefficients

As shown in Eq.(2.12) to Eq.(2.17), the expressions for the Floquet mode coefficients of the scattered fields can be further written as Eq.(B.1) to Eq.(B.6).

$$b_{mnx}^{(j)} = \frac{k_{jzmn}}{L_x L_y} \sum_{p,q} \int_p dxdy k_{ym} f_x e^{-i[(k_{xn}-k_{xq})x'+(k_{ym}-k_{yp})y'+k_{jzmn}f(x',y')]} \alpha_{pqx}$$

$$+\frac{k_{jzmn}}{L_x L_y} \sum_{p,q} \int_p dxdy (k_{ym} f_y - k_{jzmn}) e^{-i[(k_{xn}-k_{xq})x'+(k_{ym}-k_{yp})y'+k_{jzmn}f(x',y')]} \alpha_{pqy}$$

$$+\frac{ik_{jzmn}}{L_x L_y} \sum_{p,q} \int_p dxdy e^{-i[(k_{xn}-k_{xq})x'+(k_{ym}-k_{yp})y'+k_{jzmn}f(x',y')]} \beta_{pqx} \qquad \text{(B.1)}$$

$$b_{mny}^{(j)} = \frac{k_{jzmn}}{L_x L_y} \sum_{p,q} \int_p dxdy (k_{jzmn} - k_{xn} f_x) e^{-i[(k_{xn}-k_{xq})x'+(k_{ym}-k_{yp})y'+k_{jzmn}f(x',y')]} \alpha_{pqx}$$

$$+\frac{-k_{jzmn}}{L_x L_y} \sum_{p,q} \int_p dxdy k_{xn} f_y e^{-i[(k_{xn}-k_{xq})x'+(k_{ym}-k_{yp})y'+k_{jzmn}f(x',y')]} \alpha_{pqy}$$

$$+\frac{ik_{jzmn}}{L_x L_y} \sum_{p,q} \int_p dxdy e^{-i[(k_{xn}-k_{xq})x'+(k_{ym}-k_{yp})y'+k_{jzmn}f(x',y')]} \beta_{pqy} \qquad \text{(B.2)}$$

$$b_{mnz}^{(j)} = \frac{-k_{jzmn}}{L_xL_y}\sum_{p,q}\int_p dxdy k_{ym}e^{-i[(k_{xn}-k_{xq})x'+(k_{ym}-k_{yp})y'+k_{jzmn}f(x',y')]}\alpha_{pqx}$$

$$+\frac{k_{jzmn}}{L_xL_y}\sum_{p,q}\int_p dxdy k_{xn}e^{-i[(k_{xn}-k_{xq})x'+(k_{ym}-k_{yp})y'+k_{jzmn}f(x',y')]}\alpha_{pqy}$$

$$+\frac{ik_{jzmn}}{L_xL_y}\sum_{p,q}\int_p dxdy f_x e^{-i[(k_{xn}-k_{xq})x'+(k_{ym}-k_{yp})y'+k_{jzmn}f(x',y')]}\beta_{pqx}$$

$$+\frac{ik_{jzmn}}{L_xL_y}\sum_{p,q}\int_p dxdy f_y e^{-i[(k_{xn}-k_{xq})x'+(k_{ym}-k_{yp})y'+k_{jzmn}f(x',y')]}\beta_{pqy} \qquad \text{(B.3)}$$

$$a_{mnx}^{(j)} = \frac{-k_{jzmn}}{L_xL_y}\sum_{p,q}\int_p dxdy k_{ym}f_x e^{-i[(k_{xn}-k_{xq})x'+(k_{ym}-k_{yp})y'-k_{jzmn}f(x',y')]}\alpha_{pqx}$$

$$+\frac{-k_{jzmn}}{L_xL_y}\sum_{p,q}\int_p dxdy (k_{ym}f_y+k_{jzmn})e^{-i[(k_{xn}-k_{xq})x'+(k_{ym}-k_{yp})y'-k_{jzmn}f(x',y')]}\alpha_{pqy}$$

$$+\frac{-ik_{jzmn}}{L_xL_y}\sum_{p,q}\int_p dxdy e^{-i[(k_{xn}-k_{xq})x'+(k_{ym}-k_{yp})y'-k_{jzmn}f(x',y')]}\beta_{pqx} \qquad \text{(B.4)}$$

$$a_{mny}^{(j)} = \frac{k_{jzmn}}{L_xL_y}\sum_{p,q}\int_p dxdy (k_{jzmn}+k_{xn}f_x)e^{-i[(k_{xn}-k_{xq})x'+(k_{ym}-k_{yp})y'-k_{jzmn}f(x',y')]}\alpha_{pqx}$$

$$+\frac{k_{jzmn}}{L_xL_y}\sum_{p,q}\int_p dxdy k_{xn}f_y e^{-i[(k_{xn}-k_{xq})x'+(k_{ym}-k_{yp})y'-k_{jzmn}f(x',y')]}\alpha_{pqy}$$

$$+\frac{-ik_{jzmn}}{L_xL_y}\sum_{p,q}\int_p dxdy e^{-i[(k_{xn}-k_{xq})x'+(k_{ym}-k_{yp})y'-k_{jzmn}f(x',y')]}\beta_{pqy} \qquad \text{(B.5)}$$

$$a_{mnz}^{(j)} = \frac{k_{jzmn}}{L_xL_y}\sum_{p,q}\int_p dxdy k_{ym}e^{-i[(k_{xn}-k_{xq})x'+(k_{ym}-k_{yp})y'-k_{jzmn}f(x',y')]}\alpha_{pqx}$$

$$+\frac{-k_{jzmn}}{L_xL_y}\sum_{p,q}\int_p dxdy k_{xn}e^{-i[(k_{xn}-k_{xq})x'+(k_{ym}-k_{yp})y'-k_{jzmn}f(x',y')]}\alpha_{pqy}$$

$$+\frac{-ik_{jzmn}}{L_xL_y}\sum_{p,q}\int_p dxdy f_x e^{-i[(k_{xn}-k_{xq})x'+(k_{ym}-k_{yp})y'-k_{jzmn}f(x',y')]}\beta_{pqx}$$

$$+\frac{-ik_{jzmn}}{L_xL_y}\sum_{p,q}\int_p dxdy f_y e^{-i[(k_{xn}-k_{xq})x'+(k_{ym}-k_{yp})y'-k_{jzmn}f(x',y')]}\beta_{pqy} \qquad \text{(B.6)}$$

Since $e^{-i[(k_{xn}-k_{xq})x'+(k_{ym}-k_{yp})y'\pm k_{jzmn}f(x',y')]}$ is periodic, there are

$$\int_P dxdy f_x e^{-i[(k_{xn}-k_{xq})x'+(k_{ym}-k_{yp})y'\pm k_{jzmn}f(x',y')]}$$
$$= \mp \frac{k_{xn}-k_{xq}}{k_{zmn}} I_j^{\pm} \tag{B.7}$$

$$\int_P dxdy f_y e^{-i[(k_{xn}-k_{xq})x'+(k_{ym}-k_{yp})y'\pm k_{jzmn}f(x',y')]}$$
$$= \mp \frac{k_{ym}-k_{yp}}{k_{jzmn}} I_j^{\pm} \tag{B.8}$$

where $I_j^{\pm} = \int_P dxdy e^{-i[(k_{xn}-k_{xq})x'+(k_{ym}-k_{yp})y'\pm k_{jzmn}f(x',y')]}$. Then the coefficients in the expressions of $[\mathbf{b}_{mn}]$ and $[\mathbf{a}_{mn}]$ in terms of the surface fields can be derived as shown in Eq.(2.28) and Eq.(2.29).

BIBLIOGRAPHY

[1] Y. H. Kerr, "Soil moisture from space: Where are we?" *Hydrogeology Journal*, vol. 15, no. 1, pp. 117–120, Feb. 2007.

[2] US Global Change Research Program, "Conceptualization of the water cycle," http://www.usgcrp.gov, 2003.

[3] Yann H. Kerr, Philippe Waldteufel, Jean-Pierre Wigneron, Jean-Michel Martinuzzi, Jordi Font, and Michael Berger, "Soil Moisture Retrieval from Space: The Soil Moisture and Ocean Salinity (SMOS) Mission," *IEEE Transactions on Geoscience and Remote Sensing*, vol. 39, no. 8, pp. 1729–1735, Aug. 2001.

[4] Hubert M. J. P. Barr, Berthyl Duesmann, and Yann H. Kerr, "SMOS: The Mission and the System," *IEEE Transactions on Geoscience and Remote Sensing*, vol. 46, no. 3, pp. 587–593, Mar. 2008.

[5] A. Merzouki, H. McNairn and, A. Pacheco, "Mapping soil moisture using radarsat-2 data and local autocorrelation statistics," *IEEE Journal of Selected Topics in Applied Earth Observations and Remote Sensing*, vol. 4, no. 1, pp. 128–137, Mar. 2011.

[6] M. Moghaddam, S. Saatchi, and R. H. Cuenca, "Estimating Subcanopy Soil Moisture with Radar," *Journal of Geophysical Research*, vol. 105, no. D11, pp. 14 899–14 911, 2000.

[7] S. Hensley, T. Michel, J. Van Zyl, R. Muellerschoen, B. Chapman, S. Oveisgharan, Z. Haddad, T. Jackson, I. Mladenova, "Effect of Soil Moisture on Polarimetric-Interferometric Repeat Pass Observations by UAVSAR during 2010 Canadian Soil Moisture Campaign," *Proceedings of IGARSS 2011*, pp. 1063–1066, 2011.

[8] M. Moghaddam, Y. Rahmat-Samii, E. Rodriguez, D. Entekhabi, J. Hoffman, D. Moller, L. E. Pierce, S. Saatchi, and M. Thomson, "Microwave Observatory of Subcanopy and Subsurface (MOSS): A Mission Concept for Global Deep Soil Moisture Observations," *IEEE Transactions on Geoscience and Remote Sensing*, vol. 45, no. 8, pp. 2630–2643, Aug. 2007.

[9] D. Entekhabi, E. G. Njoku, P E. O'Neill, K. H. Kellogg, W. T. Crow, W. N. Edelstein, J. K. Entin, S. D. Goodman, T. J. Jackson, J. Johnson, J. Kimball, J. R. Piepmeier, R. D. Koster, N. Martin, K. C. McDonald, M. Moghaddam, S. Moran, R. Reichle, J. C. Shi, M. W. Spencer, S. W. Thurman, L. Tsang, and J. Van Zyl, "The Soil Moisture Active Passive (SMAP) Mission," *Proceedings of the IEEE*, vol. 98, no. 5, May 2010.

[10] Agriculture and Agri-Food Canada, "Soil landscapes, vegetation, and associated soil profiles," http://sis.agr.gc.ca, 2008.

[11] Y. Oh, K. Sarabandi, and F. T. Ulaby, "An Empirical Model and an Inversion Technique for Radar Scattering from Bare Soil Surfaces," *IEEE Transaction on Geoscience and Remote Sensing*, vol. 30, no. 2, pp. 370–381, Mar. 1992.

[12] P. C. Dubois, J. J. Van Zyl, and E. T. Engman, "Measuring Soil Moisture With Imaging Radar," *IEEE Transactions on Geoscience and Remote Sensing*, vol. 33, no. 4, pp. 915–926, July 1995.

[13] W. S. Ament, "Forward- and Back-Scattering from Certain Rough Surfaces," *IEEE Transactions on Antennas and Propagation*, vol. 4, no. 3, pp. 369–373, July 1956.

[14] V. Twersky, "On Scattering and Reflection of Electromagnetic Waves by Rough Surfaces," *IEEE Transactions on Antennas and Propagation*, vol. 5, no. 1, pp. 81–90, Jan 1957.

[15] P. Beckmann, "A New Approach to the Problem of Reflection from a Rough Surface," *Acta Technica CSAV*, vol. 2, no. 4, pp. 311–355, Jan 1957.

[16] J. A. Kong, *Electromagnetic Wave Theory*.   John Wiley & Sons, Inc., 1990.

[17] Alireza Tabatabaeenejad and Mahta Moghaddam, "Bistatic Scattering from Three-Dimensional Layered Rough Surfaces," *IEEE Transactions on Geoscience and Remote Sensing*, vol. 44, no. 8, Aug. 2006.

[18] A. Voronovich, "Small-Slope Approximation for Electromagnetic Wave Scattering at a Rough Interface of Two Dielectric Half-Spaces," *Waves in Random Media*, vol. 4, pp. 337–367, 1994.

[19] G. Berginc, "Small-Slope Approximation Method: A Further Study of Vector Wave Scattering from Two-dimensional Surfaces and Comparison with Experimental Data," *PIERS*, vol. 37, pp. 251–287, 2002.

[20] K. F. Warnick and W. C. Chew, "Numerical Simulation Methods for Rough Surface Scattering," *Waves in Random Media*, vol. 11, no. 1, pp. R1–R30, Jan 2001.

[21] F. D. Hastings, J. B. Schneider, and S. L. Broschat, "A Monte-Carlo FDTD Technique for Rough Surface Scattering," *IEEE Transactions on Antennas and Propagation*, vol. 43, no. 11, pp. 1183–1191, Nov. 1995.

[22] H. T. Chou and J. T. Johnson, "A Novel Acceleration Algorithm for the Computation of Scattering from Rough Surfaces with the Forward-Backward Method," *Radio Science*, vol. 33, no. 5, pp. 1277–1287, Nov 1998.

[23] D. A. Kapp and G. S. Brown, "A New Numerical Method for Rough-Surface Scattering Calculations," *IEEE Transactions on Antennas and Propagation*, vol. 44, no. 5, pp. 711–721, May 1996.

[24] V. Jandhyala, E. Michielssen, S. Balasubramaniam, and W. C. Chew, "A Combined Steepest Descent-Fast Multipole Algorithm for the Fast Analysis of Three-dimensional Scattering by Rough Surfaces," *IEEE Trans. Geosci. Remote Sens.*, vol. 36, no. 3, pp. 738–748, May 1998.

[25] P. C. Waterman, "New Formulation of Acoustic Scattering," *J. Acoust. Soc. Am.*, vol. 45, no. 6, pp. 1417–1429, 1969.

[26] W. C. Chew, *Waves and Fields in Inhomogeneous Media*. New York: IEEE Press, 1995.

[27] Metin A. Demir, Joel T. Johnson, and Tom J. Zajdel, "A study of the fourth-order small perturbation method for scattering from two-layer rough surfaces," *IEEE Transactions on Geoscience and Remote Sensing*, in review, 2011.

[28] A. Schuster, "Radiation through a foggy atmosphere," *Asro-phys. J*, vol. 21, pp. 1–22, 1905.

[29] F. T. Ulaby, R. K. Moore, and A. D. Fung, *Microwave Remote Sensing*. Artech House, Inc, 1982.

[30] L. L. Foldy, "The multiple scattering of waves," *Phys. Rev.*, vol. 67, pp. 107–109, 1945.

[31] Leung Tsang, Jin Au Kong, Kung-Hau Ding, and Chi On Ao, *Scattering of Electromagnetic Waves: Advanced Topics*. New York: Wiley, 2001.

[32] J. Korringa and R. L. Mills, "Coherent-potential approximation for the random system with short range correlations," *Phys. Rev. B*, vol. 5, pp. 1654–1655, 1972.

[33] L. Tsang and J. A. Kong, "Scattering of electromagnetic waves from random media with strong permittivity fluctuations," *Radio Sci.*, vol. 16, pp. 303–320, 1981.

[34] L. Tsang, J. A. Kong, and R. T. Shin, *Theory of Microwave Remote Sensing*. New York: Wiley-Interscience, 1985.

[35] Weng Cho Chew, James A. Friedrich, and Robert Geiger, "A multiple scattering solution for the effective permittivity of a sphere mixture," *IEEE Transactions on Geoscience and Remote Sensing*, vol. 28, no. 2, pp. 207–214, Mar. 1990.

[36] Chih-hao Kuo and Mahta Moghaddam, "Two-dimensional full-wave scattering from discrete random media in layered rough surfaces," *Proceedings of IEEE APS 2007*, pp. 4801–4804, June 2007.

[37] A. K. Fung, *Microwave Scattering and Emission Models and Their Applications*. Norwood, MA: Artech House, 1994.

[38] K. S. Chen, Tzong-Dar Wu, Leung Tsang, Qin Li, Jiancheng Shi, and A. K. Fung, "Emission of Rough Surfaces Calculated by the Integral Equation Method with Comparison to Three-Dimensional Moment Method Simulations," *IEEE Transactions on Geoscience and Remote Sensing*, vol. 41, no. 1, Jan 2003.

[39] P. Dubois and J. van Zyl, "An Empirical Soil Moisture Estimation Algorithm Using Imaging Radar," *1994 International Geoscience and Remote Sensing Symposium*, vol. 3, pp. 1573–1575, May 1994.

[40] J. T. Johnson, R. T. Shin and J. A. Kong, "Scattering and Thermal Emission from a Two Dimensional Periodic Surface," *Progress In Electromagnetics Research*, vol. 15, pp. 303–333, 1997.

[41] Leung Tsang, Jin Au Kong, Kung-Hau Ding, and Chi On Ao, *Scattering of Electromagnetic Waves: Numerical Simulations*.   New York: Wiley, 2001.

[42] M. Zribi, N.Baghdadi, etc., "Evaluation of a Rough Soil Surface Description with ASAR-ENVISAT Radar Data," *Remote Sensing of Environment*, vol. 95, no. 1, pp. 67–76, Mar 2005.

[43] Shaowu Huang, Leung Tsang, Eni G Njoku, and Kuan-Shan Chen, "Backscattering Coefficients, Coherent Reflectivities, and Emissivities of Randomly Rough Soil Surfaces at L-band for SMAP Applications Based on Numerical Solutions of Maxwell Equations in Three-Dimensional Simulations," *IEEE Transaction on Geoscience and Remote Sensing*, vol. 48, no. 6, June 2010.

[44] X. Duan and M. Moghaddam, "3-D Vector Electromagnetic Scattering from Arbitrary Random Rough Surfaces using Stabilized Extended Boundary Condition Method for Remote Sensing of Soil Moisture," *IEEE Transaction on Geoscience and Remote Sensing*, vol. PP, no. 99, August 2011.

[45] Chih-Hao Kuo and Mahta Moghaddam, "Scattering from Multilayer Rough Surfaces Based on the Extended Boundary Condition Method and Truncated Singular Value Decomposition," *IEEE Trans. Antennas Propag.*, vol. 54, no. 10, Oct. 2006.

[46] A. Tabatabaeenejad and M. Moghaddam, "Study of validity region of small perturbation method for two-layer rough surfaces," *IEEE Transactions on Geoscience and Remote Sensing*, vol. 7, no. 2, pp. 319–323, Apr. 2010.

[47] Metin A. Demir, "Perturbation Theory of Electromagnetic Scattering from Layered Media with Rough Interfaces," *Dissertation*, the Ohio State University 2007.

[48] Magda El-Shenawee, "Polarimetric Scattering from Two-Layered Two-Dimensional Random Rough Surfaces with and without Buried Objects," *IEEE Transactions on Geoscience and Remote Sensing*, vol. 42, no. 1, Jan. 2004.

[49] N. R. Peplinski, F. T. Ulaby, and M. C. Dobson, "Dielectric properties of soils in the 0.3 - 1.3 ghz range," *IEEE Transaction on Geoscience and Remote Sensing*, vol. 33, no. 3, pp. 803–807, May 1995.

[50] ——, "Corrections to 'dielectric properties of soils in the 0.3 - 1.3 ghz range," *IEEE Transaction on Geoscience and Remote Sensing*, vol. 33, no. 6, p. 1340, Nov. 1995.

[51] M.A. Mojida and H. Cho, "Evaluation of the time-domain reflectometry (tdr)-measured composite dielectric constant of root-mixed soils for estimating soil-water content and root density," *Journal of Hydrology*, vol. 295, pp. 263–275, 2004.

[52] Jozef Michalov, "Dielectric properties of the root system tissues of a 130-day-old maize plant," *Journal of Electroanalytical Chemistry*, vol. 155, pp. 405–411, 1983.

[53] Dennis S. Schrock, "How to prevent construction damage," *University of Missouri Extension*, 2000.

[54] W. Z. Yan, Y. Du, H. Wu, and D. W. Liu, "EM Scattering from a Long Dielectric Circular Cylinder," *Progress in Electromagnetics Research*, vol. 85, pp. 39–67, 2008.

[55] Robert H. MacPhie and Ke-Li Wu, "A Plane Wave Expansion of Spherical Wave Functions for Modal Analysis of Guided Wave Structures and Scatterers," *IEEE Transactions on Antennas and Propagation*, vol. 51, no. 10, pp. 2801–2805, Oct 2003.

[56] M. Haynes and M. Moghaddam, "Multipole and S-Parameter Antenna and Propagation Model," *IEEE Transactions on Antennas and Propagation*, vol. 59, no. 1, pp. 225–235, Jan 2011.

[57] K. Sarabandi and T. -C. Chiu, "Optimum Corner Reflectors for Calibration of Imaging Radars," *IEEE Transaction on Antennas and Propagation*, vol. 44, no. 10, pp. 1348–1361, Oct. 1996.

[58] K. Sarabandi and F. T. Ulaby, "A convenient technique for polarimetric calibration of single-antenna radar systems," *IEEE Transaction on Geoscience and Remote Sensing*, vol. 28, no. 6, pp. 1022–1033, Nov. 1990.

[59] Anastasis C. POLYCARPOU, Constantine A. BALANIS, Craig R. BIRTCHER, "Radar cross section of trihedral corner reflectors using PO and MEC," *Annals of Telecommunications*, vol. 50, no. 5-6, pp. 510–516, Nov. 1995.

[60] T. Bongiovanni, H. Enos, A. Monsivais-Huertero, B. Colvin, K. Nagarajan, J. Judge, P. Liu, J. Fernandez-Diaz, R. De Roo, Y. Goykhman, X. Duan, D. Preston, R. Shrestha, C. Slatton, M. Moghaddam, and A. England, "Field Observations During the Eighth Microwave Water and Energy Balance Experiment (MicroWEX-8): from June 16 through August 24, 2009," *Document Series of the Agricultural and Biological Engineering Department, Florida Cooperative Extension Service, Institute of Food and Agricultural Sciences, University of Florida*, 2011.

[61] S. L. Durden, J. J. Van Zyl, and H. A. Zebker, "Modeling and Observation of the Radar Polarization Signature of Forested Areas," *IEEE Transactions on Geoscience and Remote Sensing*, vol. 27, no. 3, pp. 290–301, May 1989.